Band 67

Schriftenreihe des Lehrstuhls für
Wasserchemie und Wassertechnologie
und der DVGW-Forschungsstelle am Engler-Bunte-Institut
des Karlsruher Instituts für Technologie (KIT)

Nanoparticles in biofilm systems – assessment of their interactions by magnetic susceptibility balance and magnetic resonance imaging

Maria Pia Herrling

Herausgeber
Harald Horn

Karlsruhe 2016

Maria Pia Herrling
Nanoparticles in biofilm systems – assessment of their interactions by magnetic susceptibility balance and magnetic resonance imaging

Herausgeber: Harald Horn
Band 67
Schriftenreihe des Lehrstuhls für Wasserchemie und Wassertechnologie und der DVGW-Forschungsstelle am Engler-Bunte-Institut des Karlsruher Instituts für Technologie (KIT)
Karlsruhe 2016

ISSN: 2195-2973
Lehrstuhl für Wasserchemie und Wassertechnologie und DVGW-Forschungsstelle
am Engler-Bunte-Institut des Karlsruher Instituts für Technologie (KIT)
Engler-Bunte-Ring 9
D-76131 Karlsruhe
Tel.: +49-(0)721-608-42581
Fax: +49-(0)721-608-46497
E-mail: ebi-sekretariat-wasserchemie@kit.edu
http://wasserchemie.ebi.kit.edu/

Titelbild: Biosorption von Eisen-Nanopartikeln an Biofilmen. Quelle: dieses Werk.

Nanoparticles in biofilm systems – assessment of their interactions by magnetic susceptibility balance and magnetic resonance imaging

zur Erlangung des akademischen Grades eines
DOKTORS DER INGENIEURWISSENSCHAFTEN (Dr.-Ing.)

der Fakultät für Chemieingenieurwesen und Verfahrenstechnik des
Karlsruher Instituts für Technologie (KIT)

genehmigte
DISSERTATION

von
Diplom Geoökologin Maria Pia Herrling
aus Pforzheim

Referent: Prof. Dr. Harald Horn
Korreferent: Prof. Dr. Susanne Lackner
Korreferent: Prof. Dr. Hermann Nirschl
Tag der mündlichen Prüfung: 17. Dezember 2015

Acknowledgement

"*Alone we can do so little; together we can do so much*." - I would like to express my sincere gratitude to a **great number of people** who contributed to this work. It would not have been possible to do without the support and guidance that I received.

Firstly, I would like to thank my advisor **Prof. Dr. Harald Horn** for his continuous support of my Ph.D study and research, for his motivation, immense knowledge and teaching me how interpret and present results in a scientific and exciting way. I appreciate that he provided an excellent work environment and gave me the freedom to pursue different research topics. Besides the provided funding, he encouraged and supported me to successfully apply for several scholarships.

I am thankful to my advisor **Prof. Dr. Susanne Lackner** who is now a professor at the University of Weimar. I appreciate all her expert contributions of time, ideas, and discussions about designing experiments and meeting research needs to make my Ph.D. experience very productive. The enthusiasm she has for her research and her professional guidance was motivational for me, even during tough times in the Ph.D. pursuit. I am also thankful for the excellent example she has provided me as a successful woman engineer and professor.

I wish to thank my NMR advisor **Priv.-Doz. Dr. Gisela Guthausen** from the NMR facility center Pro^{2}NMR at KIT. She has taught me how good experimental work (not only using NMR) is done. Although I was not officially her PhD student, she always set aside time for me. She significantly contributed and improved the quality of this work by writing matlab scripts for data processing, supervising joined student projects and finally by social activities.

A special thanks to **Prof. Dr. Matthias Franzreb** from the Institute of Functional Interfaces at KIT. He was willing to lend me his magnetic susceptibility balance for more than 3 years.

Thank you, **Prof. Dr. Hermann Nirschl** from of the Institute for Mechanical Process Engineering and Mechanics at KIT for accepting to be the third reviewer of my dissertation.

A special thanks to **all Colleagues, all Technicians** and **all former Colleagues** of the Chair of Water Chemistry and Water Technology at Engler-Bunte-Institut. The group has been a source of friendships as well as good advice and collaboration. Thank you, **Rafael Peschke**, **Reinhard Sembritzki, Axel Heidt,**

Uli Reichert, Elly Karle and **Matthias Weber** for the great help in the laboratory and during the "*Praktikum*"-period. **Dunja Haak, Sylvia Heck** and **Ursula Schäfer** thanks for your support over the years.

I would like to express my thanks to **Gudrun Abbt-Braun, Birgit Gordalla**, **Stephanie West** and **all Post-Docs**: **Michael Wagner, Marius Majewsky, Florencia Saravia** and **Andrea Hille-Reichel** who have been a constant example of successful scientists for me. I am especially appreciative of the support I received from **Markus Delay**. He was the one who inspired me to work with nanomaterials and shared all his knowledge with me.

It was a real pleasure to work with the international group of **PhD students**. **Di Peng, Jueying Quian** and **Elham Fatoorehchi**, thank your for your motivation and positive spirit over the years. I am especially grateful for conversations with **Eva Gilbert, Shelesh Agrawal, Fabian Brunner** and **Samuel Welker** who constructively improved the quality of manuscripts and my own interdisciplinary understanding of NMR. Furthermore, I want to especially acknowledge the **group of PhD students** who joined the unforgettable trip to India in 2014, this experience will always be related to you. I will miss you.

My time at Engler-Bunte-Institut was made enjoyable in large part due to the many friends that became a part of my life. I am especially grateful for time spent with my favorite officemate and close friend **Chunyan Li**. Thank you for your endless support, constructive suggestions and inspiring discussions over the years. You are fabulous.

A special thanks to all excellent **bachelor and master students** who have played important roles during my Ph.D. and have contributed to the achieved results: **Sarah Lüken, Oleg Tatti, Katharina Fetsch, Alexander Hirn, Philipp Tepper, Christian Gurrath, Laure Cuny, Florian Ranzinger, Manuel Haas, Jessica Weisbrodt** and all the **students and (former) colleagues** of the NMR laboratory.

Additionally, I want to acknowledge the colleagues from the Institute for Mechanical Process Engineering and Mechanics at KIT: **Felicitas Arndt, Eva Förster, Fabian Bülow** and **Franz Dalitz**.

I am very thankful for the great hospitality I experienced at the NMR laboratory of **Prof. Dr. Sarah Codd** and **Prof. Dr. Joseph Seymour** at Montana State University. Thank you for this great personal and professional experience. It was a real pleasure to participate at the NMR field project of **Catherine Kirkland**. **Catherine Kirkland, Andrew Bender** and **Jaci Peick,** thank you for taking care of me during my stay - you are very special to me.

A special thanks to **Prof. Dr. Frank Gu** and **Perry Everett** for hosting me at the Waterloo Institute of Nanotechnology for 2 weeks at University of Waterloo. It has been a great experience.

I would like to thank the **Karlsruhe House of Young Scientists (KHYS)** and the **German Carl-Zeiss Foundation** for their financial support and good cooperation during the funding period. Additionally, the **DFG** founded NMR facility center Pro^{2}NMR enabled the NMR measurements within this Ph.D. work.

Lastly, I would like to thank my family. For my **Mother** and **Father** who raised me with love and supported me in all my pursuits. For the patient and motivating presence of my sister **Ana Lena** here at KIT for three of my years here. For my best friend and partner **Christian** whose faithful support during this Ph.D. is so appreciated.

Maria Pia Herrling

Abstract

In the last decades, the increased application of engineered nanoparticles (ENP) in industrial processes and consumer products has raised concerns about their health and environmental safety. In their life cycle, ENP will potentially accumulate in wastewater treatment plants (WWTP) representing sinks for ENP. During biological WWT attachment of ENP to the biomass, e.g. biofilm systems, are responsible for the desired removal of ENP from the water phase before they enter into the environment. Ikuma *et al*. 2015 stated that "*…as biofilms are efficient "sponges" for ENP, efforts to elucidate the fundamental mechanisms guiding interactions between ENP and biofilms have just begun*." This recent citation indicates that there is still a significant knowledge gap surrounding the behavior of ENP in technical as well as natural biofilm systems. The *"sponge-like"* behavior for ENP of various biofilms needs to be evaluated to estimate potential mass flows of ENP in the environment. The lack of information is partly due to difficulties in the detection of ENP and analytical limitations, such as too low concentrations, polydispersity of ENP and the high complexity of the environmental samples. Although there are many analytical methods commercially available to quantify ENP, most of them are not able to perform *in-situ* and *in-vivo* measurements in complex water matrixes.

To contribute to a better understanding of the **interaction between ENP and real biofilms**, a **new and promising analytical approach** is demonstrated within this dissertation. This approach **utilizes inorganic magnetic iron oxide ENP (Fe_3O_4-NP)** as targeted model ENP. Inorganic Fe_3O_4-NP were employed due to their wide application spectrum and their magnetic properties. Based on their magnetic properties, Fe_3O_4-NP were detected using **magnetic susceptibility balance (MSB)** and **magnetic resonance imaging (MRI)**. The combination of those methods enables the precise quantification and visualization of Fe_3O_4-NP in the bulk water and their sorption to the biofilm in a completely *in-situ* and *non-invasive* manner. A set of experiments under different experimental conditions and time scales was conducted. The focus was to examine the role of the

- **chemistry of the water matrix,**
- **particle properties and**
- **exposure time**

on the interactions between Fe_3O_4-NP and two different kinds of biofilm systems (compact and fluffy structure). Furthermore, the influence of the biofilm structure on the local flow field (no Fe_3O_4-NP addition) was investigated to gain initial information about particle transport in biofilm systems.

First, with the aim of evaluating the influence of the chemistry of the water matrix on the removal of Fe_3O_4-NP coated with polyvinyl alcohol, batch experiments with compact granular biofilms were conducted (**chapter 4**). The results obtained by MSB show that the removal of Fe_3O_4-NP from the bulk water was rather low (5 - 35% of input Fe_3O_4-NP) compared to the findings of recent literature (up to 100 % removal). This was due to the stabilization of Fe_3O_4-NP by dissolved and particulate organic matter (OM) in the bulk water, which was released by the biofilm matrix itself. Surprisingly, also the biosorption (here defined as sum of chemical and physical sorption processes of ENP to biofilms) of Fe_3O_4-NP onto the biofilms was low as well (only 2.4 % of input Fe_3O_4-NP). The interactions of Fe_3O_4-NP with the biofilms were hampered by the smooth and compact structure of the granular biofilms and their stabilization by OM in the bulk water. Furthermore, desorption has occurred. The maximum biosolid concentration in compact granular biofilms was 1.9 µg Fe/mg TSS (total suspended solid). This indicates that instead of biosorption other processes such as co-sedimentation might be responsible for the removal of Fe_3O_4-NP. In conclusion, OM might represent a key parameter for the fate of ENP in biofilm systems.

Additional experimental work was performed under static conditions to explore the influence of the particle size and particle surface functionalization of Fe_3O_4-NP on the biosorption to biofilms exhibiting fluffy structures (**chapter 5**). The visualization using MRI revealed that the penetration depth of Fe_3O_4-NP into the biofilm matrix depends on the particle size, but not on the surface functionalization (here: starch, dextran, dextran-hydroxyl and silica coating). Fe_3O_4-NP with a diameter of 20 nm penetrated deeper into the biofilm matrix than larger ones (80 nm). However, all investigated Fe_3O_4-NP mainly sorbed to the biofilm surface and outer layers and no full penetration occurred. These results imply that especially the particle size could particularly be a key factor to consider for mass flows of Fe_3O_4-NP in biofilm systems. After an exposure of 14 days all investigated Fe_3O_4-NP were irreversibly immobilized within the biofilm matrix. This is contrary to the finding in the batch experiments with compact granular biofilms, where desorption of Fe_3O_4-NP has been observed highlighting the relevance to investigate different types of biofilms.

Further, experiments in continuous flow systems (flow cell, moving bed biofilm reactor) were performed with the aim to study the influence of exposure time on the biosorption of Fe_3O_4-NP coated with silica to fluffy biofilms (**chapter 6**). The concentration of Fe_3O_4-NP was measured in the bulk water and in the biofilm using MSB. The results show that the transport of Fe_3O_4-NP through the systems was more dominant than the biosorption to the fluffy biofilm. The maximum biosolid concentration was 3.6 µg Fe/mg TSS, which is slightly higher than in compact biofilms due to favored entrapment in the EPS. However, the retention capacity of the used biofilm systems was low. In flow cells and in a moving bed biofilm reactor, 57 - 65 % of the input Fe_3O_4-NP were released by the effluent. Furthermore, detachment

of biofilm parts loaded with Fe_3O_4-NP has occurred, which further increased the washout of Fe_3O_4-NP. The time scale of observation is important to consider for the long-term effects of the interactions of Fe_3O_4-NP with biofilms. However, for the initial interactions the exposure time is of subordinated relevance because the biosorption happened quickly (within minutes) and the transport of Fe_3O_4-NP with the flowing fluid was dominant.

In a last step, the flow field in the carrier based biofilm systems was investigated (in the absence of Fe_3O_4-NP) in the context that the local flow field influences the transport of Fe_3O_4-NP towards biofilm surface (**chapter 7**). The results obtained by MRI show that the biofilm structure had a significant impact on the surrounding flow velocities. For example, narrow pathways can be created by the biofilm, in which the flow velocities are significantly decreased due to flow evasion. The biofilm thickness and coverage of the biofilm are important factors to consider. Depending on the orientation of the biofilm carrier to the flow direction, areas of stagnation can be formed, where the transport of solutes and particles (ENP) would be dominated by diffusion. Nevertheless, there was no clear correlation between biofilm coverage and flow ratio in the biofilm carrier system.

With the help of the MSB and MRI, unique information about the fate of Fe_3O_4-NP was generated giving general indications for potential mass flows of ENP in technical as well as natural environments.

Zusammenfassung

Der verstärkte Einsatz von synthetischen Nanopartikeln (engl. engineered nanoparticles (ENP)) in industriellen Prozessen und Konsumgütern führt durch ihren Eintrag den Wasserkreislauf zu großen Problemen für Mensch und Umwelt. Dabei stellen kommunale Kläranalgen eine wichtige Senke für ENP dar um ihren weiteren Transport in die Umwelt zu verhindern. Ein besonderes Augenmerk liegt auf der biologischen Reinigungsstufe, die durch die Bindung von ENP an die Biomasse (e.g. in Form von Biofilmen) zu der gewünschten Reinigung des Wassers von ENP führt. Ikuma *et al*. 2015 hat kürzlich folgendes Zitat publiziert, das auf die Wissenslücken bezüglich der Interaktionen zwischen Biofilmen und ENP hinweist: "*…as biofilms are efficient "sponges" for ENP, efforts to elucidate the fundamental mechanisms guiding interactions between ENP and biofilms have just begun*." Informationen über die Interaktion von ENP mit Biofilmen geben Hinweise für ihr Verhalten und potentielle Stoffströme in technischen aber auch natürlichen Biofilmsystem. Die genannte Wissenslücke ist unter anderem durch Limitationen in der Partikelanalytik bedingt. Probleme für die Bestimmung von ENP in Umweltproben sind vor allem niedrige Konzentrationen, Polydispersität der ENP und die komplexe Probenmatrix. Obwohl zahlreiche Geräte zur Partikelanalyse erhältlich sind, fehlt es an Methoden, die im Stande sind *in-situ* und *in-vivo* Messungen durchzuführen.

Für die **Untersuchung der Interaktion von ENP mit echten Biofilmen** wurde in dieser Promotionsarbeit ein **neuer analytischer Ansatz** verwendet. **Anorganische magnetische ENP (Fe_3O_4-NP)** wurden als Modellnanopartikel eingesetzt, da sie ein breites Anwendungsspektrum haben und magnetische Eigenschaften besitzen. Der Verbleib der Fe_3O_4-NP wurde basierend auf ihren magnetischen Eigenschaften mittels der **Magnetischen Suszeptibilitätswaage (MSB)** und **Magnetischer Resonanz-Tomographie** (engl. Magnetic Resonance Imaging **(MRI)**) festgestellt. Die Kombination dieser Methoden ermöglicht den Verbleib von Fe_3O_4-NP in Biofilmsystemen präzise, *in-situ* und *non-invasive* zu verfolgen (Quantifizierung und Visualisierung). Im Detail wird das Verhalten von Fe_3O_4-NP unter verschiedenen experimentellen Bedienungen und auf verschiedenen Zeitskalen untersucht. Die Experimente haben einen besonderen Fokus auf:

- **Veränderungen in der Wassermatrix,**
- **Partikeleigenschaften und**
- **Expositionszeit**

hinsichtlich der Interaktion von Fe_3O_4-NP mit zwei verschiedenen Biofilmen (fluffige und kompakte Struktur). Weiterhin wurde der Einfluss der Biofilmstruktur auf das umgebende Strömungsfeld untersucht

(in Abwesenheit von Fe_3O_4-NP) um erste Informationen über den Transport von Fe_3O_4-NP an die Biofilmoberfläche zu generieren.

In Batchexperimenten wurde der Einfluss der Wassermatrix auf die Entfernung und Biosorption (Sammelbegriff für chemische und physikalische Sorptionsvorgänge von ENP an Biofilme) von Fe_3O_4-NP an kompakte und granulierte Biofilme untersucht (**chapter 4**). Die Konzentration der Fe_3O_4-NP wurde mittels MSB bestimmt. Im Gegensatz zu den Erkenntnissen der aktuellen Literatur, wurden die Fe_3O_4-NP in den Batchexperimenten nur zu 5 - 35 % (bezogen auf Input Fe_3O_4-NP) von der Wassermatrix entfernt. Dieses Verhalten kann vor allem durch die Stabilisierung von Fe_3O_4-NP durch gelöste und partikuläre organische Materie (OM) in der Wasserphase erklärt werden, die von der Biofilmmatrix selbst abgegeben wurde. Überraschender Weise ist auch die Biosorption der Fe_3O_4-NP sehr gering (nur 2,4 % der Input Fe_3O_4-NP). Dies liegt an der glatten und kompakten Struktur der granulierten Biofilme, die die Interaktion mit den Biofilmen vermindert. Weiterhin war die Biosorption reversibel. Die maximale Konzentration von Fe_3O_4-NP in den granulierten Biofilmen war 1.9 µg Fe/mg TS (Trockensubstanz). Die Ergebnisse weisen darauf hin, dass die Biosorption durch den stabilisierenden Einfluss von OM und die kompakte Struktur der granulieren Biofilm schwach ausgeprägt ist. Somit können andere Interaktionen, wie Co-sedimentation dominanter sein als die Biosorption.

Zusätzliche Experimente wurden unter statischen Bedingungen durchgeführt um die diffusionsgetriebene Interaktion und Biosorption verschieden großer und funktionalisierter Fe_3O_4-NP in fluffigen Biofilmsystem mittels MRI zu untersuchen (**chapter 5**). Die Untersuchungen mittels MRI haben gezeigt, dass die Partikelgröße einen deutlichen Einfluss auf die Penetrationstiefe von Fe_3O_4-NP in die Biofilmmatrix hatte. Kleinere Fe_3O_4-NP (20 nm) penetrierten stärker als größere (80 nm), was für die generellen Stoffströme von ENP von Bedeutung ist. Interessanter Weise hatte die Oberflächenfunktionalisierung der Fe_3O_4-NP (wie beispielsweise: Stärke, Dextran, Silica oder Dextran mit Hydroxylresten) keinen signifikanten Einfluss auf die Penetration in die Biofilmmatrix. Die Fe_3O_4-NP haben sich hauptsächlich - unabhängig von Größe und Funktionalisierung - an der Oberfläche und den äußeren Biofilmschichten angelagert und penetrierten den Biofilm nicht vollständig. Nachdem die Biofilme 14 Tage den Fe_3O_4-NP ausgesetzten waren, fand eine irreversible Immobilisierung von allen getesteten Fe_3O_4-NP statt. Dies ist gegensätzlich zu den Ergebnissen mit granulierten Biofilmen und gibt Hinweise, dass die Untersuchung von verschiedenen Biofilmstrukturen von höchster Wichtigkeit ist.

Des Weiteren wurde das Verhalten und die Biosoption von Fe_3O_4-NP in Systemen mit kontinuierlichem Durchfluss (Flow Cells und Moving Bed Biofilm Reaktor (MBBR)) hinsichtlich der Expositionszeit untersucht (**chapter 6**). Die Ergebnisse (erhoben mittel MSB) zeigen, dass der Transport von Fe_3O_4-NP mit dem Fluid dominanter war als die Biosorptionsprozesse. Einen Anteil von 57 - 65 % der ursprünglich

hinzugegebenen Fe_3O_4-NP haben die Systeme ohne Biosorption passiert. Somit ist die Rückhaltekapazität der Biofilmsysteme in der Flow Cell und im MBBR gering. Die maximale Konzentration an Fe_3O_4-NP im fluffigen Biofilm war 3.6 µg Fe/mg TS - höher als für die kompakten granulierten Biofilme. Das kann an der offenen Biofilmstruktur liegen, die die Fe_3O_4-NP leichter einfangen können. Die Interaktion der Fe_3O_4-NP mit den Biofilmen geschieht jedoch schnell (innerhalb von Minuten) und der Transport von Fe_3O_4-NP ist dominant. Somit hat die Expositionszeit einen geringen Einfluss auf die initiale Biosorption. Um jedoch die Langzeitfolgen von der Interaktion von Fe_3O_4-NP mit den Biofilmen beobachten zu können, spielt die Zeitskala eine wichtige Rolle. Beispielsweise können Änderungen in der Biofilmstruktur stattfinden: nach 3 h Expositionszeit haben sich Teile des Biofilms, die Fe_3O_4-NP enthalten, abgelöst und so zu weiterem Austrag von Fe_3O_4-NP aus dem Biofilmsystem geführt.

Um den Transport von ENP zur Biofilmoberfläche besser zu charakterisieren, wurde in einem letzten Schritt, der Einfluss der Struktur eines auf einem Träger gewachsenen Biofilms auf das umgebende lokale Strömungsfeld untersucht (ohne Zugabe von Fe_3O_4-NP) (**chapter 7)**. Die Ergebnisse, die mittels MRI erhoben worden sind, zeigen, dass die Struktur der Biofilme die lokalen Strömungsgeschwindigkeiten entscheidend beeinflussen. Die geschieht zum Beispiel durch enge Passagen, in welchen die Strömungsgeschwindigkeiten verlangsamt waren. Dabei spielen die Biofilmdicke und die Verteilung der Biofilms in dem Träger eine wichtige Rolle. Abhängig von der Orientierung des Trägers zur Strömungsrichtung, kann es zu Stagnation kommen und der Transport von gelösten und partikulären Stoffen (ENP) wäre dann durch Diffusionsvorgänge dominiert.

Mit Hilfe der Magnetischen Suszeptibilitätswaage und Magnetischer Resonanz-Tomographie konnten im Rahmen dieser Arbeit spezifische Daten generiert werden, die Hinweise für die Interaktionen und den Verbleib von ENP in natürlichen, sowie in technischen Biofilmsystemen geben.

Publications

The chapters 4, 5, 6 and 7 of this dissertation have been published in the following peer-reviewed articles.

Herrling, M. P., Guthausen G., Wagner M., Lackner, S., Horn, H. (**2015**). *Determining the flow regime in a biofilm carrier by means of magnetic resonance imaging*. Biotechnology and Bioengineering. 112(5): 1023–1032.

Herrling, M. P., Fetsch, K., Delay, M., Blauert, F., Wagner M., Franzreb, M., Horn, H., Lackner, S. (**2015**). *Low biosorption of PVA coated engineered magnetic nanoparticles in granular sludge assessed by magnetic susceptibility*. Science of the total Environment. 537: 43–50.

Herrling, M. P., Lackner, S., Tatti, O., Delay, M., Guthausen, G., Franzreb, M., Horn, H. (**2016**). *Short and Long Term Biosorption of Iron Oxide Nanoparticles in heterotrophic Biofilms*. Science of the total Environment, 544: 722–729.

Ranzinger, F., **Herrling, M. P.**, Lackner, S. Grande, V., Baniodeh, A., Powell, A., Horn, H., Guthausen, G. (**2016**). *Direct surface visualization of biofilms with high spin coordination clusters using magnetic resonance imaging*. Acta Biomaterialia, 31: 167–177.

Cuny, L., **Herrling, M. P.**, Guthausen, G., Horn, H., Delay, M. (**2015**). *Magnetic resonance imaging reveals detailed spatial and temporal distribution of iron-based nanoparticles transported through water-saturated porous media*. Journal of contaminant Hydrology. 182: 51–61.

Kirkland, C., **Herrling, M. P.**, Hiebert, R., Bender, A., Grunewald, E., Walsh, D., Codd, S. (**2015**). *In-situ detection of subsurface biofilm using low-field NMR - a field study.* Environmental Science and Technology. 49: 11045–11052.

Guthausen, G., Machado, J. R., Luy B., Baniodeh, B., Powell, A. K., Krämer, S., Ranzinger, F., **Herrling, M. P.**, Lackner, S., Horn, H. (**2015**). *Characterisation and application of ultra-high spin clusters as magnetic resonance relaxation agents*. Dalton Transactions. 44: 5032–5040.

Contents

1 INTRODUCTION

1.1 Motivation

In the early 90's, nanoscience and nanoparticle research emerged globally. The production of nanomaterials is expected to rise to 58,000 tons per year between 2011 and 2020 (Maynard 2006). The increasing number of applications using engineered nanoparticles (ENP) in consumer products and in industry (Heiligtag and Niederberger 2013, Nowack *et al.* 2012) has led to their undesired release into the environment, e.g. through wastewater streams. Especially in the global water cycle, the distribution of ENP as pollutants needs to be controlled to avoid harmful effects on humans and the environment.

ENP can be divided in organic (e.g. carbon nanotubes, fullerenes) and inorganic (e.g. Fe-, Ti,- Ag-, or Zn-based ENP) nanomaterials (Delay and Frimmel 2012). Inorganic metal-based ENP represent the main research focus due to their wide application spectrum and toxicity. For example, concentrations of metallic ENP, such as TiO_2-based ENP were reported to be up to 1.6 µg/L in surface waters (Gottschalk *et al.* 2013b), which could have negative impacts on natural ecosystems. Numerous mathematical models and experimental studies have been conducted in an effort to better understand and predict the potential pathways of ENP in the environment (Gottschalk *et al.* 2013b, Schaumann *et al.* 2015, Sun *et al.* 2014). Particularly in the water cycle, wastewater treatment plants (WWTP) represent potential sinks for ENP by their accumulation in the biological treatment step (Mueller and Nowack 2008, Nowack 2009, Nowack and Bucheli 2007, Nowack *et al.* 2012, Schaumann *et al.* 2015, Som *et al.* 2010). During the biological WWT, ENP are mostly removed from the water phase by attachment to biomass (Gottschalk *et al.* 2013a, Westerhoff *et al.* 2013). The removal of various ENP from the water in WWT systems differs between 10 % and 90 % (Westerhoff *et al.* 2013) with varying effluent concentrations (Gottschalk *et al.* 2013b). This has been examined in batch experiments and continuous flow WWT systems (bioreactors, pilot plants) with varying particle concentrations and exposure times. However, the desired removal of ENP cannot be predicted or regulated yet (Westerhoff *et al.* 2013) and more research is required to understand the fate of ENP. Besides the removal of ENP from the water phase, the identification of concentrations of ENP in biomass from WWTP is a current research need (Westerhoff *et al.* 2013). The biomass from WWT is still disposed in landfills or applied to agricultural soils (Blaser *et al.* 2008, Brar *et al.* 2010) potentially leading to migration of ENP into soils and groundwater.

The lack of information concerning the distribution of ENP is partly due to difficulties in their detection and analytical limitations, such as too low concentrations, polydispersity of ENP and the high complexity of the environmental samples (Delay and Frimmel 2012). Although there are many analytical methods

commercially available to quantify ENP, most of them are not able to perform *in-situ* and *in-vivo* measurements in complex water matrixes (Lowry *et al.* 2012).

But not only the analytical limitations represent a challenge for the estimation of the mass flows of ENP, also the interactions of ENP with the biomass are highly complex and not yet fully understood (Ikuma *et al.* 2015). The biomass in WWT is commonly organized as suspended active sludge and numerous studies demonstrated the sludge mediated removal of ENP from the water phase (Kaegi *et al.* 2013, Kiser *et al.* 2009). However, in newer biological water treatment technologies the biomass is organized in form of biofilms and only few data on the removal and biosolid concentrations of ENP in biofilms is currently available (Westerhoff *et al.* 2013). Biofilms consist of microorganisms embedded in a matrix of extracellular polymeric substances (EPS) anchoring themselves to surfaces (Lewandowski and Beyenal 2013). They are ubiquitous in technical as well as natural environments, (Costerton 1999) and therefore, the accumulation of ENP in the biofilm matrix will affect the mass flows of ENP and their possible harmful impacts. When ENP reach the biofilm surface (by diffusive or advective transport) complex interactions in time and space are expected to happen. In WWT, attachment of ENP to the biofilms is the most important interaction. The attachment is so far summarized in the term “biosorption”, which covers all sorption processes (chemisorption, physical sorption), entrapment in the biofilm structure and biouptake of ENP into the biofilm matrix and cells (Brar *et al.* 2010, Kiser *et al.* 2010). The interactions mainly depend on the type of biofilm (chemical and physical structure) and on the particle properties (e.g. particle surface functionalization and particle size). In turn, the particle properties are strongly related to the chemistry of the surrounding water matrix (Elimelech *et al.* 1995). For example, ENP can be stabilized in the water phase by the coating of their particle surface with natural organic matter (NOM) (Delay *et al.* 2011) and as a consequence, their biosorption to biofilms might be hampered (Fabrega *et al.* 2009b). As mentioned earlier, the structure of the biofilm also impacts the interaction with ENP. Biofilms exhibit diverse physical structures, such as smooth, flat, rough, fluffy or filamentous structures (Flemming and Wingender 2010). For example, fluffy biofilm structures (high specific surface area) enhance the biosorption of ENP by entrapment in their EPS compared to more compact structures (Gu *et al.* 2014, Ma *et al.* 2013). Other types of interactions, such as electrostatic, steric and, chemical interactions between ENP and the biofilm surface, biofilm matrix and embedded cells has been demonstrated in numerous studies (Fabrega *et al.* 2009b, Keller *et al.* 2010, Nevius *et al.* 2012, Zhang *et al.* 2009). However, the research about the fundamental mechanisms being responsible for the interactions are still at the beginning (Ikuma *et al.* 2015).

1.2 Objectives of this work

As mentioned in the motivation, the detailed interactions between ENP and real biofilm systems are still not fully understood and it requires more research to better estimate the fate of ENP. However, the distribution of ENP in complex environmental systems is difficult to evaluate partly due to analytical limitations. This is why this dissertation aims to demonstrate a **new and promising analytical approach** to examine the **interactions between ENP and real biofilm systems**. For this approach, easily traceable inorganic **magnetic iron oxide ENP (Fe_3O_4-NP)** were selected as targeted model ENP. Inorganic Fe_3O_4-NP were employed due to their wide application spectrum and their magnetic properties. Based on their magnetic properties, Fe_3O_4-NP were detected completely *in-situ* and *non-invasively* using **magnetic susceptibility balance (MSB)** and **magnetic resonance imaging (MRI).** MSB allows the simple quantification of Fe_3O_4-NP in the water phase and the biosolid concentration in the biofilm matrix (down to tens of µg/L). Complementary to the quantification, the interaction between Fe_3O_4-NP (serving as contrast agents) and biofilms was visualized using MRI. MRI provides spatio-temporally resolved information about the distribution of Fe_3O_4-NP in the undisturbed structure of the biofilm. The combination of both methods generates unique information to elucidate the fate of Fe_3O_4-NP within the real biofilm system.

This new analytical combination of MSB and MRI was applied to examine the interactions of Fe_3O_4-NP with biofilm systems originating from WWT under different experimental conditions and time scales. Exposure experiments of Fe_3O_4-NP with a sufficient degree of complexity were conducted in different experimental setups (batches, flow cells and moving bed biofilm reactor) involving two different types of biofilms (fluffy and compact biofilm structure). The objective was to characterize the interaction and biosorption of Fe_3O_4-NP to biofilms with respect to the **chemistry of the water matrix**, **the particle properties and the exposure time**. Complementary to that, addressing the transport of ENP to the biofilm surface (perquisite to the interaction), the **influence of the biofilm structure on the local flow field** was investigated in absence of Fe_3O_4-NP. An overview of the conducted experiments is given in Table 1-1. Besides the superordinate goal to demonstrate the applicability of the new analytical approach, the objectives related to the chapters in this dissertation are pointed out in the following:

- Characterize the removal and the biosorption of Fe_3O_4-NP in compact granular biofilm systems in laboratory batch experiments with respect to the water matrix **(Chapter 4)**.

- Visualize the diffusion dominated biosorption and immobilization of Fe_3O_4-NP within fluffy biofilm systems in laboratory batch experiments with respect to their particle size and functionalization **(Chapter 5)**.

- Compare the behavior and biosorption of Fe_3O_4-NP in fluffy biofilm systems in short term and long term exposure experiments in continuous flow systems, such as flow cells and moving bed biofilm reactor **(Chapter 6)**.

- Determine the local flow field around heterogeneous biofilm structures in continuous flow cells to estimate the transport of particles to the biofilm surface **(Chapter 7)**.

The results improve the understanding of ENP-biofilm-interactions by the relocation of ENP within the biofilm matrix and differentiation of possible interaction processes. This represents one step towards the better prediction of the fate of ENP in the biofilm systems and their potential mass flows, also regarding their passage through WWTP. Furthermore, reliable data on the biosolid concentration of ENP is provided by the application of MSB and MRI, which can serve as input data for a better risk assessment of ENP in technical as well as natural environment.

1.2.1 Overview of conducted experiments

Two different types of biofilm systems (exhibiting a compact and fluffy structure) were exposed to differently sized and functionalized Fe_3O_4-NP in various experimental set-ups (batch, flow cell, moving bed biofilm reactor (MBBR)), see chapter 4 - 6. To determine the flow field in the used biofilm system, a continuous flow experiment was conducted in the absence of Fe_3O_4-NP, see chapter 7. In order to assist the reader, an overview of all conducted experiments is provided in the following table.

Table 1-1: Overview of all conducted experiments within this dissertation. Abbreviations: magnetic susceptibility balance (MSB), magnetic resonance imaging (MRI), moving bed biofilm reactor (MBBR).

chapter	system	type of biofilm and Fe_3O_4-NP	exposure time	method	aim
4	shaken batch experiments	granular biofilm; Fe_3O_4-NP with polyvinyl alcohol coating	18 h	MSB	• removal and biosorption by granular biofilm • consideration of changes in the water matrix and type of biofilm
5	static batch experiments	fluffy biofilm; Fe_3O_4-NP with dextran, starch, dextran-hydroxyl coating	14 d	MRI	• spatially resolved biosorption and immobilization in biofilms • consideration of different particle properties
6	continuous flow experiments in flow cell and MBBR	fluffy biofilm; Fe_3O_4-NP with silica coating	5 min, 30 d	MSB; MRI	• spatially-temporally resolved biosorption in biofilms • consideration of the contact time and transport
7	continuous flow experiments in flow cell	fluffy biofilm; no Fe_3O_4-NP	-	MRI	• determination of the local flow regime in biofilm systems • indications for particle transport in biofilm systems

2 BACKGROUND

2.1 Nanoparticles

Belonging to the group of nanomaterials, the use of the term "nanoparticle" (NP) is widespread and there are diverse accepted definitions available (Auffan *et al.* 2009). The unit prefix "*nano*" means 10^{-9} (one billionth) and is derived from the Greek word νάνος (nános) meaning dwarf. According to the International Organization for Standardization (ISO), NP are defined as particulate materials with all dimensions between 1 nm and 100 nm (ISO 2008). NP can be of natural or of anthropogenic origin (engineered nanoparticles (ENP)). Natural NP result from physical, chemical and biological processes (e.g. weathering of rocks, forest fire, volcano eruption) and they are therefore ubiquitous in soils, water and air (Christian *et al.* 2008, Mihai *et al.* 2015). In contrast, NP synthesized for targeted applications are of anthropogenic origin (then called ENP). ENP are of high interest: In 2005 the total global investment in nanotechnologies was 10 billion US$ with rising tendency (Navarro *et al.* 2008a) indicating the immense application of nanomaterials, including ENP. ENP can be divided in organic (e.g. carbon nanotubes, fullerenes) and inorganic (e.g. Fe-, Au-, Ag-, Al-, Ti-, Ce-, Si-, Zn-based ENP) nanomaterials. ENP usually consist of a particle core and one or several surface shells and coatings. The particle surface chemistry can be modified by the functionalization with organic or inorganic functional groups or molecules with specific properties (e.g. hydrophobicity, surface charge, geometry). Therefore, ENP are widely used in consumer products (e.g. textiles, cosmetics), technical and industrial applications and biomedical applications (Brar *et al.* 2010, Mihai *et al.* 2015, Schmid 2010). In the field of environmental engineering, ENP enable advanced wastewater treatment (Theron *et al.* 2008) and soil remediation (Mueller and Nowack 2010, Zhang 2003). This work addresses the group of inorganic ENP, especially iron based magnetic iron oxide nanoparticles (Fe_3O_4-NP).

Magnetic iron oxide nanoparticles (Fe_3O_4-NP)

In this dissertation Fe_3O_4-NP are used as model ENP to trace their fate in biofilm systems. Their magnetic particle property enables following their distribution *via* magnetic susceptibility measurements (quantification) and magnetic resonance imaging (visualization). Therefore, a short introduction about Fe_3O_4-NP is given in the following.

Beyond other technical relevant inorganic metal(oxide) ENP such as e.g. Ag-, Au-, Ce-, TiO_2-NP, the application of magnetic Fe_3O_4-NP in particle science and fundamental research has been perused intensively (Laurent *et al.* 2008). Fe_3O_4-NP are applied in medical diagnostics (Ito *et al.* 2005) and drug delivery (Gupta and Gupta 2005, Mahmoudi *et al.* 2011a), catalysis (Kang *et al.* 2011), soil remediation

(Masciangioli and Zhang 2003) or heavy metal absorption in waste water treatment (Hu *et al.* 2006). In biomedicine, super paramagnetic iron oxide nanoparticles (SPION) are often used as contrast agents in magnetic resonance imaging (Mahmoudi *et al.* 2011b). The magnetism of Fe_3O_4-NP can be either ferrimagnetic or superparamagnetic depending on the particle size and the physic-chemical properties. To prevent their oxidation and destabilization, Fe_3O_4-NP are often coated with organic substances such as hydrophilic polymers (e.g. polyethylene glycol) or polysaccharides (e.g. dextran, starch) or with inorganic shells (e.g. silica, carbon). These coatings provide electrostatic and steric stabilization of the Fe_3O_4-NP and can be helpful for further functionalization with ligands (Lu *et al.* 2007).

2.1.1 Behavior in aquatic systems

The increasing application of ENP in costumer products and industry results inevitably in their release into the environment such as surface waters (Benn and Westerhoff 2008, Delay and Frimmel 2012, Gottschalk and Nowack 2011, Klaine *et al.* 2008, Navarro *et al.* 2008a, Wiesner *et al.* 2009). Consumer products can release ENP either:

- as free single particles,
- as aggregates,
- as particles with a specific surface functionalization or
- as particles embedded in a matrix (Nowack and Bucheli 2007).

As inorganic ENP are often composed of eco-toxic materials - it is essential to evaluate potential negative impacts on ecosystems and human health in short and long-term (Buzea *et al.* 2007, Navarro *et al.* 2008a, Wiesner *et al.* 2006). In this context, especially Ag-NP have been studied due to their antibacterial effects (Ahamed *et al.* 2010, Kim *et al.* 2014). Numerous toxicity studies involve living organisms, such as bacteria (Li *et al.* 2013, Mahmoudi *et al.* 2009, Navarro *et al.* 2008b), plants (Navarro *et al.* 2008a), zebra fish (Yeo and Kang 2008) and mammals (Buzea *et al.* 2007). In conjunction with the risk assessment of ENP, particle analysis is a prerequisite. The standard characterization of ENP in liquid samples implies the analysis of the particle size distribution using e.g. dynamic light scattering or electron microscopy techniques (Delay and Frimmel 2012). The chemical composition and concentrations of ENP is conventionally analyzed by inductively coupled plasma mass spectrometry (ICP-MS) after acid digestion (Barth 1984, Farré and Barceló 2012). A summary of the commonly used analytical methods is given elsewhere (Quik *et al.* 2011). However, difficulties such as low concentrations, high matrix effects, particle reactivity, polydispersity and missing standard materials for calibration limit the detection of ENP in environmental water samples (Delay and Frimmel 2012). This is why there is only a limited database regarding the real concentrations of ENP in the environment compared to other chemical compounds e.g.

inorganic or organic trace pollutants (Mueller and Nowack 2008). Many authors stress the lack of adequate and standardized analytical methods and detailed descriptions of the conducted research, e.g. operational conditions and risk management measures (Clark *et al.* 2012, Delay and Frimmel 2012). Through that, the research is ongoing. The Organisation for Economic Co-operation and Development (OECD) recently conducted a survey on the available methods and models for assessing the exposure to ENP. They pointed out that the next steps lie in the evaluation of the methods and the techniques for a direct exposure sampling and measurement (OECD 03. July 2015).

Despite the analytical challenges, numerous experimental and modeling studies significantly contributed to elucidate the fate of ENP in the environment in the last decade (Gottschalk *et al.* 2013a, Sun *et al.* 2014). It has been shown that, once in the environment, ENP underlie complex interactions and transformations with and by inorganic and organic components in the water matrix. ENP undergo chemical reactions (e.g. surface modifications), physical reactions (e.g. deposition) as well as biological reactions (biological oxidation). Moreover, neoformation of ENP might also occur (Christian *et al.* 2008, Delay and Frimmel 2012, Klaine *et al.* 2008, Lowry *et al.* 2012). Addressing the mobility, reactivity and potential interactions with biological systems, the particle size and stability of ENP in suspension are key factors to consider. The following gives a short introduction about the parameters influencing the particle stability in suspension. For fundamentals of particle deposition and aggregation please consult e.g. the textbook of Elimelech *et al*. (1995).

Particle Surface Charge

ENP have a high surface energy, which favors the collision of ENP leading to agglomeration and most likely sedimentation processes. To prevent agglomeration, ENP can be stabilized in solution by for example electrostatic stabilization due to particle surface charges. Particle surface charges can originate from:

- reactions on the particle surface (-functionalization) causing variable charges depending on the pH value (protonation, deprotonation),
- isomorphic substitution or crystal defects in the solid core material of ENP leading to permanent particle surface charges or
- adoption of hydrophobic substances on the particle surface.

The model of the electric double layer by STERN, GOUY und CHAPMAN describes the distribution of the particle surface charge in water suspension with electrolytes, see Figure 2-1. The particle surface charge (NERNST potential) has to be balanced by (hydrated and dehydrated) counter-ions from the water matrix.

Consequently, ion layers are established near by the particle surface, exemplary depicted for a negatively charged particle, see Figure 2-1: the first layer is the STERN layer (immobile ion layer) followed by the GOUY-CHAPMAN layer (diffusive ion layer, uneven distribution of ions) (Elimelech *et al.* 1995, Stumm 1992, Stumm and Morgan 1996).

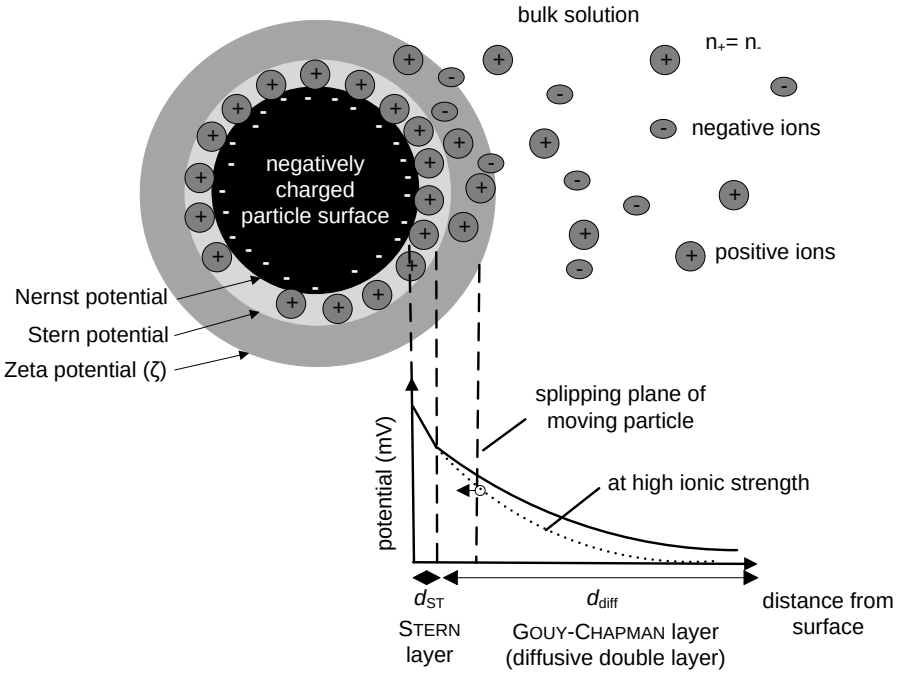

Figure 2-1: Schematic of the electrical double layer on a negative charged particle surface in a system with electrolytes after Stumm (1992). The thickness of the STERN layer d_{ST} and the diffusive layer d_{diff} are determined by the water matrix and particle properties. The abbreviation *n* refers to the number of ions in the solution. The proportions of this figure are out of scale.

Influence of ionic strength and pH

In environmental samples the stability of ENP is mainly affected by the ionic strength and pH value (Delay *et al.* 2011). For the analysis of the particle surface charge, an electric field is applied across the dispersion. Depending on their surface charge, particles will move towards the electrode with the opposite charge reaching a constant velocity. The electric field will cause a displacement of the charges within diffusive double layer on the ions (GOUY-CHAPMAN layer). The charge will be sheared off due to the particle movement (at the slipping plane). Then the particles lose their balanced state by counter ions. The resulting potential at the slipping plane is defined as the zeta potential (ζ), see Figure 2-1. Among others, the zeta potential depends on the pH value. The protonation (low pH values) or deprotonation (high pH values) of the particle surface is balanced at the point of zero charge (PZC), where the particle surface charge is neutral. At PZC particles in suspension tend to homo-agglomerate due to low electrostatic

repulsive forces. In particle science, the zeta potential serves as indicator for particle stability: when the zeta potential is around ± 30 mV a particle suspension is considered to be stable (electrostatic stabilization). In case of solutions with high ionic strength (high ion concentrations), the agglomeration of particles is favored. When the bulk solution has an increased ion concentration, e.g. in wastewaters, the diffusive double layer will be compressed, see dotted line in plot of Figure 2-1. This is due to faster surface charge balancing which lowers the potential (subplot in Figure 2-1). In summary, a low a zeta potential close to PZC of particles and a high ionic strength promote particle agglomeration in suspensions (Jiang *et al.* 2009, Ottofuelling 2011, Stumm 1992). The stability of dispersions of ENP and their tendency for agglomeration is described using the theory of DERJAGUIN-LANDAU-VERWEY-OVERBEEK (DLVO) considering electrostatic forces, steric forces, and VAN DER WAALS forces between single ENP (Derjaguin and Landau 1941), see appendix A.2.

Influence of natural organic matter (NOM)

In complex water matrices, interactions of ENP with natural organic matter (NOM) are of high relevance for the particle stabilization and mobility (Baalousha *et al.* 2008, Cuny *et al.* 2015, Delay *et al.* 2011, Pelley and Tufenkji 2008, Tiller and Omelia 1993). NOM consists of organic macromolecules such as humic acids, fulvic acids and humins, and non-humic substances such as proteins, polysaccharides, nucleic acids, and amino acids (Jones and Bryan 1998). NOM is able to sorb on the surface of ENP and contribute to a steric (long organic chains) as well as electrostatic (shift to more negative surface potential) stabilization of the ENP (Keller *et al.* 2010, Napper 1977, Ottofuelling 2011). However, NOM in combination with bivalent ions, such as Ca^{2+} can lead to bridging and flocculation processes resulting in particle destabilization (Delay *et al.* 2011, Zhang *et al.* 2009). The (temporal or long-term) coating of the surface of ENP with organic molecules has been described as “corona” of ENP. This organic “corona” significantly influences the fate of ENP due to favored interactions with other biomolecules (Monopoli *et al.* 2012), such as the surfaces of biofilm systems.

2.1.2 Nanoparticles meet biofilms

Biofilms

Biofilms are composed of microorganisms populations or other organisms (protozoa, algae, fungi) which attach to surfaces (usually solid-liquid) and are embedded in a matrix of extracellular polymeric substances (EPS) (Horn 2004, Lewandowski and Beyenal 2013). More than 90 % of the total global microorganisms form multispecies biofilms as present in ecosystems such as lakes, surface waters, ground waters, as well as terrestrial ecosystems (Kallmeyer *et al.* 2012). The biofilm's EPS matrix is highly heterogeneous and complex. EPS consist of a large number of organic molecules such as

- polysaccharides (40 - 95 %),
- proteins (< 1 - 60 %),
- nucleic acids (< 1 - 10 %) and
- lipids (< 1 - 40 %)

as well as inorganic compounds and humic substances (Flemming and Wingender 2001). Polysaccharides and proteins for example favor the aggregation of the cells in the biofilm while serving as nutrition source. Depending on the microbial composition of the biofilm, it can consist of 10 - 25 % of cells and 75 - 90 % EPS matrix (Costerton 1999). The biofilm structure and composition strongly depends on the chemical and hydrodynamic environment during the biofilm growth, and thus varies in time and space (Flemming and Wingender 2010, Flemming and Wingender 2002, Horn 2004, Van Loosdrecht *et al.* 1995). Extensive shear stress at high flow velocities will lead to thinner and more compact biofilm structures, and lower flow velocities to more fluffy open biofilm morphologies depending on the substrate load (De Beer *et al.* 1996, De Beer *et al.* 1994b, Stewart 2012). In this context, biofilms can form, e.g. smooth, flat, rough, fluffy, or filamentous (Flemming and Wingender 2010) structures. Biofilms are able to settle in ecological niches exposed to extreme living conditions with regard to pH, hydrodynamic and osmotic stress as well as exposure to biocides and antibiotics (Costerton *et al.* 1994, Stewart and Costerton 2001). Biofilms are also able to persist unwanted at locations, such as clinical instruments, therein causing tremendous problems as they can host pathogens triggering infections and diseases (Costerton *et al.* 2005, Hall-Stoodley and Stoodley 2009). In technical systems, the presence of biofilms can be critical as well by e.g. biofouling of membranes for water purification (von der Schulenburg *et al.* 2008b). Nevertheless, biofilms also have great advantages: in nature, life would not be possible without biofilms forming a large number of micro scale ecosystems (e.g. subaerial biofilms (Gorbushina 2007), marine biofilms (Mai-Prochnow *et al.* 2004)). Furthermore, biofilms enable technical applications in, e.g. biological wastewater treatment

(McQuarrie and Boltz 2011, Odegaard *et al.* 1994) and bioremediation of soils and ground waters (Lewandowski and Beyenal 2013).

Therefore, biofilm systems became an important interdisciplinary research topic, merging biology, chemistry, and engineering science (Morgenroth and Milferstedt 2009). Imaging techniques for the investigation of the biofilm structure and functionality are summarized in section 3.2.2 and will not be discussed at this point.

Behavior of ENP in biofilm systems

With respect to the distribution of ENP in the environment, their interactions with biofilms have a major impact on mass flows and bioavailability (Fabrega *et al.* 2011, Westerhoff *et al.* 2013). As in most environments, microorganisms (MO) preferentially exist in form of biofilms, and a fundamental understanding of the interactions of ENP with biofilms is critical to monitor the fate of ENP. Compared to microorganisms organized in suspended form (sludge, single cells), there is less research on the interactions and accumulation of ENP within natural biofilm systems (Ikuma *et al.* 2015) as well as biofilms used in WWT (Westerhoff *et al.* 2013).

In Figure 2-2 parameters, processes and possible interactions of ENP with biofilms in water phase are summarized according to Brar *et al*. (2010) and Ikuma *et al*. (2015). In the following, the main focus will be on the small-scale interaction processes with the biofilm and less on transport of ENP. As mentioned in section 2.1.1, the environmental behavior of ENP strongly depends on the particle properties (**1**) and their potential transport to the biofilm surface (**2**), see bold numbers in Figure 2-2. The particle size, shape and surface are mainly driven by the physical, chemical, and biological environment, e.g. chemistry of the water matrix, fluid flow, temperature (Delay and Frimmel 2012, Petosa *et al.* 2010). Homo- and hetero-agglomeration (**3**) and subsequent sedimentation (**4**) is expected to occur in environmental water matrixes (**5**). For example, an increased the ionic strength might lead to particle agglomeration (**3**). Besides their surface functionalization by specific coatings or organic ligands for targeted applications, the surface of ENP can further be modified under environmental conditions such as the sorption of NOM or other organic matter (OM) forming an organic "corona" (see 2.1.1). The "corona" stabilizes ENP in the bulk water and can lead to a steric repulsion with the biofilm matrix on the one hand (Fabrega *et al.* 2009a, Lowry *et al.* 2012). On the other hand, it has been reported that OM coated ENP can also facilitate the surface interactions with biofilms by organic binding sites (Fabrega *et al.* 2009b, Morrow *et al.* 2010). Generally, it has been demonstrated that the surface properties (e.g. functionalization and modifications) of ENP are more dominant for the interaction with biofilms than the core material (Fabrega *et al.* 2009a, Fabrega *et al.* 2009b, Fabrega *et al.* 2011, Nevius *et al.* 2012, Thill *et al.* 2006). In any case, "bare" ENP

are non-existent in the environment due to transformations and interactions with other components (Ikuma *et al.* 2015). The direct interactions of ENP also depends on the structure of the biofilm (**6**), see Figure 2-2), specifically on its physical (e.g. pores, compactness) and chemical (e.g. EPS content) properties as shown by only few studies involving model biofilms (Sahle-Demessie and Tadesse 2011) and real biofilms originating from WWT (Gu *et al.* 2014, Ma *et al.* 2013). Several studies proved that the EPS matrix plays a key role, especially for the interactions of ENP with biofilms, as it provides preferential binding sites for sorption and accumulation (Battin *et al.* 2009, Kroll *et al.* 2014, Sheng and Liu 2011). Nevertheless, changes in the chemical and physical structure after exposure to inorganic ENP have been observed, e.g. by an exposure of >100 mg ZnO-NP /g TSS to granular biofilms, the concentrations of proteins, DNA, lipids, and humic acids in the EPS were significantly decreased (Mu *et al.* 2012).

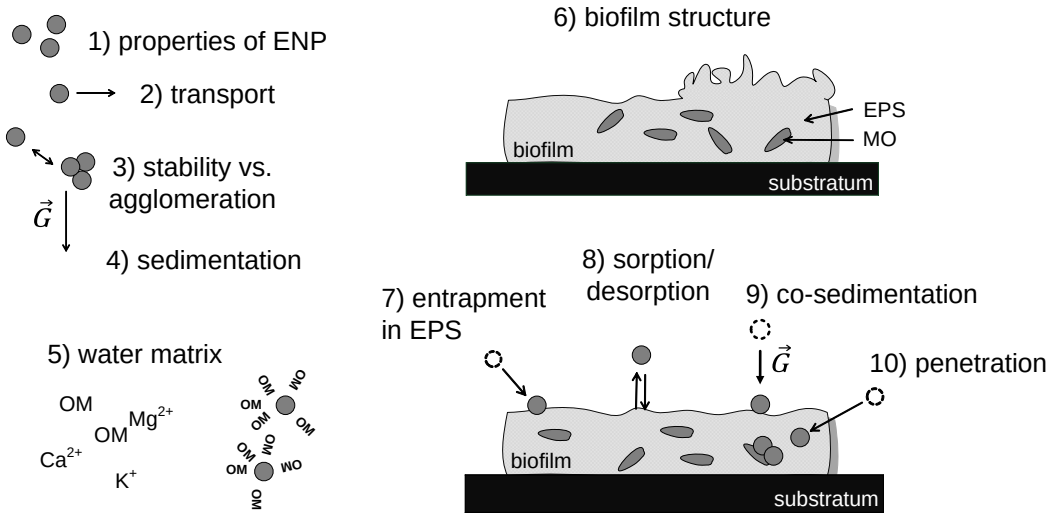

Figure 2-2: Environmental parameters and processes involved in the interactions of ENP and biofilms (indicated by numbers), adopted schematic after Brar *et al.* (2010) and Ikuma *et al.* (2015). Abbreviations: OM: organic matter, MO: microorganisms, EPS: extracellular polymeric substances, $\vec{G}$: force of gravity. The proportions in this figure are out of scale.

Once ENP reach the biofilms surface, various interactions can take place (Figure 2-2) such as:

- entrapment in EPS matrix (**7**),
- sorption and desorption (**8**),
- physical co-sedimentation (**9**) and
- penetration in to the biofilm matrix and cells (**10**)

(Battin *et al.* 2009, Brar *et al.* 2010, Ikuma *et al.* 2015, Westerhoff *et al.* 2013).

Mainly driven by the morphology and structure of the biofilm (**6**), entrapment of ENP (**7**) in fluffy biofilm structures such as sludge flocks is likely to happen (Brar *et al.* 2010). However, the dominant process for the attachment of ENP to biofilms are sorption processes (**8**) which can be either physical sorption (e.g. electrostatic or VAN DER WAALS forces) or chemisorption (e.g. chemical interaction). The attachment is so far summarized in the term "biosorption", which covers all sorption processes (chemisorption, physical sorption), entrapment in the biofilm structure and biouptake of ENP into the biofilm matrix and cells (Kiser *et al.* 2010). This term is frequently used for the general description of attachment processes of ENP to biomass, which remove ENP from WWT (Gomez-Rivera *et al.* 2012, Herrling *et al.* 2015a, Otero-Gonzalez *et al.* 2015). Research about surface interactions, especially concerning the electrostatic forces by the resulting zeta potential of ENP is ongoing (Ikuma *et al.* 2014). Besides the attachment processes, physical co-sedimentation (**9**) of ENP can happen in systems with suspended biofilms such as special (granular) biofilms. Co-sedimentation is an indirect interaction, which can enhance the removal of ENP from the bulk water especially by biofilms exhibiting compact structures hampering sorption processes (Herrling *et al.* 2015a). Finally, when ENP are deposited to the biofilm surface they are able to penetrate the EPS matrix and might interact with cells (**10**). ENP, e.g. Ag-NP, are able to diffuse into biofilms (e.g. *Pseudomonas fluorescence* biofilms), but the transport and penetration into the biofilm matrix under realistic conditions leading to biological uptake is mainly restricted by the particle size of ENP (Battin *et al.* 2009, Peulen and Wilkinson 2011). By an increased diameter of ENP, for example of Ag-NP the diffusion coefficients into the biofilm matrix were reduced (Peulen and Wilkinson 2011). Furthermore, there are indications given that ENP preferentially accumulate extracellular (Fabrega *et al.* 2009b, Limbach *et al.* 2008), but also intracellular uptake was observed (Yu *et al.* 2015). Generally, the penetration of ENP into the biofilm matrix can inhibit the biological activity of the biofilm and disturb the cell integrity (Ma *et al.* 2013, Sheng and Liu 2011). For example, the degree of toxicity of FeO-NP to microorganisms (*Saccharomyces cerevisiae* and *Escherichia coli*) correlated with their sorption to the cell membranes mainly attributed to electrostatic forces (Schwegmann *et al.* 2010). In contrast, it has been shown that ENP can be structurally embedded in the biofilm and sludge matrix without necessarily disrupting the cell membranes (Hou *et al.* 2014, Sibag *et al.* 2015). Supporting to this finding, studies employing biofilms (e.g. *Pseudomonas fluorescence*) and ecotoxic ENP (e.g. Ag-NP) found that the presence of NOM in the bulk solution hampers the toxic effect by coating the surface of ENP (Fabrega *et al.* 2009a). Besides the toxic effects of e.g. Ag-NP, it has been recently demonstrated that concentrations of Ag-NP in the range of tens µg/L can also stimulate biofilm development of *Pseudomonas aeruginosa* (Yang and Alvarez 2015). As the interactions of ENP with single cells and cell membranes are not the focus of this work, please consult extensive reviews for more information (Nel *et al.* 2009, Stark 2011).

2.1.3 Removal of nanoparticles in wastewater treatment

The aim of municipal WWTP is to efficiently remove most of the nutrients (nitrogen, phosphorus and carbon compounds), pathogens, and other contaminants from the wastewater in mechanical, biological, and chemical treatment steps (Wiesmann *et al.* 2007). In biological treatment, organic compounds are partly degraded by heterotrophic bacteria. Moreover, incorporation of suspended solids (organic and inorganic matter) into the biomass is part of the treatment process. The biomass hosts a high biodiversity of microorganisms such as bacteria and protozoa. Depending on the type of bioreactor and on the operation conditions the biomass is organized e.g. in

- flocculent and filamentous sludge flocks (activated sludge),
- compact granular biofilms (spherical biofilm system) or
- biofilms attached to carrier material (Henze 2002, Wiesmann *et al.* 2007).

Besides the common wastewater compounds mentioned above, there are other undesired pollutants such as pharmaceuticals and ENP present in the wastewater. WWTP play a key role in potential entry points of ENP to the water cycle (Kim *et al.* 2010). According to mass flow models of ENP WWTP are expected to be exposed to significant amounts of ENP (Nowack 2009, Nowack and Bucheli 2007, Som *et al.* 2010). A typical concentration range of ENP, e.g. of TiO_2-NP in surface waters is 3 ng/L to 1.6 µg/L, whereas in effluents of WWTP higher concentrations about 5 µg/L were reported (Gottschalk *et al.* 2013b). The biofilms in the biological WWT are mainly responsible for the elimination of ENP from the water phase by attachment to the biofilm (see Figure 2-2). However, the degree of the removal of ENP from the bulk water can differ significantly. In Table 2-1 the recent literature on the removal of ENP from wastewater is summarized, which confirms the variety of removal. Although the general removal can be high, the particular degree of removal does not correlate with the experimental set-up being a closed system (batch experiment) or a continuous flow WWT system (bioreactor, pilot plant, full scale WWTP). Also the type of ENP is of minor relevance with respect to the degree of removal of ENP (Kaegi *et al.* 2013). Comparative studies revealed that granular biofilms are biologically more resistant to toxic ENP, like Ag-NP or Ce-NP, than flocculent sludge due to its protective dense EPS. Moreover, granular biofilms remove ENP less efficiently compared to flocculent biofilm, which emphasizes the importance to investigate different kinds of biomass in this context (Gu *et al.* 2014, Ma *et al.* 2013). However, not a single parameter enables the estimation of the behavior of ENP, highlighting the complexity of these systems (Westerhoff *et al.* 2013). Another challenge is the assessment of the distribution of ENP in WWT systems: once ENP are removed from the water phase they do not necessarily end up sorbed to the biomass. ENP can also be removed by physical processes and transformations, e.g. sedimentation (Ganesh *et al.* 2010), see Figure 2-2. The Organisation for Economic Cooperation and Development (OECD) recently published

new information of an experimental program (based on 780 studies) where commercially availed inorganic ENP (e.g. Ce-NP, SiO_2-NP, Ag-NP, Au-NP, TiO_2-NP, ZnO-NP) have been used to generate nano-specific data on their fate and distribution in the environment. This report also contains information about fate of ENP in WWT systems pointing out that there is still a significant fraction of ENP escape from the clearing system (OECD 2015).

Table 2-1: Selected studies on the removal of different inorganic ENP from WWT classified by their experimental set-up. Abbreviations: activated sludge flocks (ASF), anaerobic granular biofilms (AG), anaerobic sludge flocks (AnSF), biofilm (BF), synthetic waste water (SWW), raw waste water (RWW), buffer solution (BS), deionized water (DW), functionalized ENP (func.), laboratory (lab.), sequencing batch reactor (SBR), hydraulic retention time of the WWT system (HRT). Results obtained within this dissertation are highlighted in bold.

reference	ENP core	biofilm	medium	removal of ENP	set-up	additional information
chapter 4 (in this dissertation)	**Fe_3O_4**	**AG**	**DW**	**<35 %**	**batch**	**18 h exposure time**
(Kiser *et al.* 2010)	TiO_2 Ag plain Ag func.	ASF	BS	23 % 97 % 39 %	batch	3 h exposure time; closed system
(Park *et al.* 2013)	Ag plain TiO_2 SiO_2	ASF	DW	90 % 95 % 95 %	batch	24 h exposure time; closed system
(Gomez-Rivera *et al.* 2012)	CeO_2	ASF	DW	94-97 %	batch	20 h exposure time; closed system
(Gu *et al.* 2014)	Ag plain	AG ASF	DW	2.5-9.4 % 30-58 %	batch	3 h exposure time; closed system
(Kaegi *et al.* 2013)	Ag func. Au func.	ASF	RWW	99 % 99 %	batch	2 h exposure time; closed system
(Ganesh *et al.* 2010)	Cu	ASF	DW	95 %	batch	20 h exposure time; closed

						system
Chapter 6 (in this dissertation)	**Fe_3O_4**	**BF**	**SWW**	**98%**	**MBBR**	**HRT: 5 h; overall removal**
(Tan *et al.* 2015)	ZnO	ASF	SWW	98 %	membrane bioreactor	HRT: 12 h; overall removal
(Otero-Gonzalez *et al.* 2014)	CuO	AG	SWW	68-80 %	anaerobic sludge reactor	HRT: 6 - 12 h; overall removal
(Hou *et al.* 2013)	ZnO	ASF	RWW	100 %	SBR	HRT: 12 h; removal per cycle
(Wang *et al.* 2012)	Ag func. TiO_2	ASF	SWW	88 % 97 %	SBR	HRT: 8 h; 18 d experiment
(Gartiser *et al.* 2014)	TiO_2	ASF	SWW	>95 %	sewage treatment plant (lab.)	HRT: 6 h; 22 d experiment; overall removal
(Kaegi *et al.* 2011)	Ag plain	ASF	SWW	95 %	pilot WWTP	HRT: 1 d; 43 d experiment
(Kiser *et al.* 2009)	TiO_2	ASF	RWW	79 %	full scale WWTP	average removal; 1 month sampling

3 METHODS

3.1 Magnetic susceptibility balance

In this dissertation a new approach is presented: the magnetic susceptibility balance (MSB) was used to assess the interaction between magnetic Fe_3O_4-NP and biofilm systems originating from WWT *in-situ* and *non-invasively*. MSB is employed in chapter 4 and 6. The promising application of MSB offers the unique possibility to quantify:

- the concentration Fe_3O_4-NP in the bulk water as well as in complex water matrices and
- the concentration of Fe_3O_4-NP in the biofilm matrix.

3.1.1 Principles of magnetic susceptibility

Introduced by GOUY in 1889, this method has been employed, e.g. in geology (Borradaile and Henry 1997) for heavy metal mapping in soils (Hanesch and Scholger 2002) or in medicine for liver tissue examination (Weiss and Witte 1973). The volume magnetic susceptibility χ_v (dimensionless) of a sample is the ratio between the magnetization M (A/m) multiplied by an inductive constant $\overline{\mu_0}$ (H/m) to the strength of the magnetic field B (T) defined by

$$\chi_V = \frac{M \cdot \overline{\mu_0}}{B}. \qquad \text{Equation 3-1}$$

χ_v is indicated in SI unit system (Earnshaw 1968, Orchard 2007) and is dimensionless. By including the density of the substance ρ (kg/m^3), the mass magnetic susceptibility χ_M (m^3/kg) can be calculated by (Earnshaw 1968)

$$\chi_M = \frac{\chi_V}{\rho}. \qquad \text{Equation 3-2}$$

χ_v and χ_M can either have a negative or positive value indicating a repulsion (diamagnetic) or an attraction (paramagnetic, superparamagnetic, ferri- or ferromagnetic) of the sample in the presence of an external magnetic field. Equations 3-1 and 3-2 are valid for one phase systems only. As environmental samples often represent multiphase systems, WIEDEMANN's Law is applied to calculate the susceptibility of the desired component (Weiss and Witte 1973). In heterogeneous samples, the total magnetic susceptibility is the sum of the magnetic susceptibilities of all components weighted by their mass fraction where m_i (kg) is the mass of substance (i) and m the total mass of the sample given by

$$\chi_{\mathrm{M\,total}} = \sum_{i=1}^{n} {}^{m_i}/_{m} \cdot \chi_{\mathrm{M},i} \,. \qquad \text{Equation 3-3}$$

The basic principle of a magnetic susceptibility measurement relies on the GOUY method (1889) (Weiss and Witte 1973). A conventional laboratory balance and a large permanent magnet were combined to measure the gain or loss in sample weight due to the applied magnetic field. The sample was placed in between two poles of a permanent magnet causing a magnetic force according to the magnetism of the inserted sample. In this work, the measurements were conducted using a laboratory magnetic susceptibility balance (MSB) which applies the GOUY method *vice versa*. The sample tube was fixed while the permanent magnets were able to move. The displacement of the magnets inside the MSB introduced by the magnetization of the sample was detected optically. The mass magnetic susceptibility measured by the MSB was then calculated by

$$\chi_M = \frac{C \cdot I_{MSB} \cdot (R - R_0)}{10^9 \cdot m} \,. \qquad \text{Equation 3-4}$$

Here, C (dimensionless) is the MSB constant and R (m^3/kg) is the reading signal of the filled sample tube. R_0 (m^3/kg) equals the signal of the empty sample tube, I_{MSB} (m) is the height of the sample in the sample tube and m (kg) is the mass of the sample.

3.1.2 Quantification of nanoparticles within biofilm matrix

Compared commonly used method for the quantification of ENP in environmental samples is atomic or mass spectroscopy (inductively coupled atomic emission and mass spectroscopy (ICP-OES, ICP-MS)) (Quik *et al.* 2011). Those are costly analytical methods which have certain limitations for the quantification of ENP in complex sample matrixes, such as invasiveness, and a time-consuming sample preparation (acid digestion) is required. In contrast, MSB offers a simple, fast and precise analytical approach to quantify ENP without sample preparation. ENP can be detected in *in-situ* in their original state and only a small sample volume of 50 µL to 200 µL is required. Samples can either be liquid, solid, or mixed phase systems offering a high applicability. The sole perquisite for the application of MSB for the quantification of ENP is their magnetic property (paramagnetic or superparamagnetic).

In this dissertation paramagnetic Fe_3O_4-NP were quantified *via* MSB. Their magnetic property causes a positive signal change in the magnetic susceptibility according to the concentration of Fe_3O_4-NP in an external magnetic field. A concentration of Fe_3O_4-NP of e.g. c(Fe) = 251 mg/L corresponds to a magnetic susceptibility of +68.839± 0.515, see Table 3-1. This correlation is only possible by the calibration of the

magnetic susceptibility of Fe_3O_4-NP determined by MSB with the iron concentration *c*(Fe), determined by ICP-OES. ICP-OES used is a conventional analytical method with a high precision and a detection limit of <1 µg/L Fe (Agilent-Technologies 2010). Linear fitting of a calibration curve resulted in a correlation coefficient close to 1, which reflects the good quality of the linear correlation, see calibration curves in Figure 4-2 and Figure 6-2. The MSB is a high precision analytical method (detection limit of $\chi_{V\,min} = 0.13 \cdot 10^{-6}$ (SI units) (Sherwood-Scientific 2006)). The validation is given by the repeatability of the standard measurement (for water, $n = 10$) which proves the high precision of the MSB (error < 2 %). Table 3-1 presents measured values for the standards deionized water (diamagnetic) and $CuSO_4$ (paramagnetic) and the expected values for their magnetic susceptibility (Landolt and Börnstein 1986). The error between measured value of deionized water and expected value is 0.2 %, see Table 3-1. The biofilms used in this dissertation are diamagnetic and close to the value of water. For the quantification of Fe_3O_4-NP sorbed to the biofilm the influence of water and biofilm on the magnetic susceptibility signal for Fe_3O_4-NP was negligible. Fe_3O_4-NP are strongly paramagnetic while water and biofilm have far lower (diamagnetic) values indicating that the water matrix and the biofilm are insignificant in this case. Water was the background matrix of all samples as the biofilms' water content is up to 95 % (Neu *et al.* 2010).

Table 3-1: Magnetic volume susceptibilities (dimensionless, SI system) of deionized water, $CuSO_4$ (standards for MSB validation) and biofilm. Asterisks (*) indicate expected values as summarized in Landolt-Börnstein (1986). Inorganic Fe_3O_4-NP were measured in suspension with deionized water. Biofilm systems used in chapter 4 and 6 are listed. The granular biofilms were sieved in three size fractions (100 - 250 µm, 250 - 500 µm, 500 - 800 µm).

sample name	sample	measured $\chi_V \cdot 10^{-6}$ (-)	expected $\chi_V \cdot 10^{-6}$ (-)	chapter
deionized water	control	-9.023 ± 0.138	-9.0478*	-
$CuSO_4$ (solid)	control	+75.474 ± 0.276	+75.398*	-
Fe_3O_4-NP PVA coating (c(Fe) = 251 mg/L)	calibration	+68.839± 0.515	-	**4**
Fe_3O_4-NP silica coating (c(Fe) = 467 mg/L)	calibration	+20.410± 0.170	-	**6**
fluffy biofilm	biofilm	-8.972 ± 0.151	-	**6**
granular biofilm (100 - 250 µm)	biofilm	-2.815± 0.578	-	**4**
granular biofilm (250 - 500 µm)	biofilm	-4.210 ± 0.151	-	**4**
granular biofilm (500 - 800 µm)	biofilm	-4.046 ± 0.188	-	**4**

For the quantification of Fe_3O_4-NP using MSB particle agglomeration has no influence on the measured magnetic susceptibility signal. Firstly, no agglomeration of Fe_3O_4-NP is introduced by internal magnetic forces in the absence of an external magnetic field. This is due to the elemental magnetic dipoles of the magnetic particles not having a permanent alignment (no magnetic behavior, no magnetic attraction). Secondly, by the application of an external magnetic field, Fe_3O_4-NP experience a strong aligned magnetization and particles can agglomerate. However, in particle agglomerates the net magnetization of the single Fe_3O_4-NP is maintained by the surface functionalization which creates an interspace between each particle. This allows the determination of Fe_3O_4-NP concentration *via* the magnetic susceptibility even though Fe_3O_4-NP are agglomerated.

3.2 Magnetic resonance imaging

In this dissertation *in-situ* and *non-invasive* magnetic resonance imaging (MRI) was used to assess the interaction between magnetic Fe_3O_4-NP and biofilm systems originating from WWT. MRI is employed in chapter 5, 6 and 7. The promising application of MRI to investigate the interactions of Fe_3O_4-NP and biofilms offers the unique possibility to visualize:

- biofilms undisturbed structure and simultaneously
- biosorption and immobilization of Fe_3O_4-NP in the biofilm matrix.

3.2.1 Principles of magnetic resonance imaging

MRI allows the *non-invasive* 2D and 3D visualization of living biological samples *in-situ* while providing specific structural parameters as well as fluid dynamics. MRI techniques contribute to a deeper insight and description of complex multi-phase systems in life science, material science and environmental science. MRI relies on the nuclear magnetic resonance (NMR), which is based on the magnetization of nuclei. The phenomenon of NMR was discovered amongst others by Felix Bloch and Edward Purcell in 1946 (noble prize in 1952) and is now widely used in analytics for e.g. chemical structure analysis (NMR spectroscopy). A further development towards MRI was realized in 1973 by introducing magnetic field gradients which enable spatial resolution of for example the proton density (Lauterbur 1973).

In this dissertation, MRI was applied for biofilm research to elucidate biofilm structure and to give indications for mass transport and interactions with ENP. The next paragraphs summarize the basic principles of MRI without claim on completeness. For a detailed description please refer to the textbooks of Kimmich (1997) and Callaghan (1991).

Nuclear magnetic resonance - the NMR signal

NMR active nuclei carry an odd number of protons and/or neutrons as e.g. ^{1}H, ^{31}P, ^{19}F, ^{23}Na, ^{13}C, ^{14}N (nuclear spin quantum number: $I > 0$, for ^{1}H: $I = \frac{1}{2}$) inducing an intrinsic nuclear spin. Hydrogen (^{1}H) has one of the highest NMR sensitivities due to its gyromagnetic ratio and the natural abundance of 99.98 % and is therefore the most targeted nucleus in MRI. The spin of the ^{1}H nuclei induces a magnetic moment (μ in A/m^2) which is proportional to the nucleus specific gyromagnetic ratio (γ in 1/(T·s)) and reduced Planck constant ($\hbar$ in J·s) by $\mu = \gamma \cdot \hbar \cdot I$. The presence of an external magnetic field applied in *z*-direction (B_0 in T) causes a precesion of the nuclear magnetization around B_0. The precesion frequency called Larmor frequency (ω_0, resonance frequency in rad/s) is proportional to the magnetic field amplitude by

$$|\omega_0| = \gamma \cdot |B_0|. \qquad \text{Equation 3-5}$$

Spins experience a parallel or antiparallel alignment with B_0 pursuant to the Boltzmann distribution. The spins alignment is associated with discrete energy states (for ^{1}H two energy states) being a lower energy state (parallel) or higher energy state (antiparallel). The energy difference (ΔE in J) of the spin states is described by

$$\Delta E = \hbar \cdot \gamma \cdot |B_0| = \hbar \cdot \omega_0 \qquad \text{Equation 3-6}$$

In the classical NMR theory, spins sum up to a net magnetization M_0 (in A/m), whose equation of motion is described by the Bloch equations. M_0 precesses around B_0 (with ω_0) and is proportional to the external magnetic field amplitude, the gyromagnetic ratio, the number of nuclei (N) in the sample and the temperature T.

To manipulate the nuclear magnetization *M*, a short radio frequency (rf) field is applied in a coil which induces a second much smaller radio frequency magnetic field B_1 orthogonal to B_0. To motivate the underlying processes of NMR, a simplified vector model in a rotating coordinate system (rotating around the *z*-axis with the Larmor frequency) is used. In this rotating coordinate system the axes are defined as *x*, *y*, *z*, see Figure 3-1. The net magnetization lies along the *y*-axis after excitation with a 90° pulse with phase *x*. More general, in the presence of B_1, the net magnetization *M* is flipped to *xy*-direction. The amplitude and duration of the rf-pulse determines the angle (φ), by which the magnetization vector is turned towards the transverse *xy*-plane. By a 90° pulse (π/2 pulse) the NMR signal received by in the sample surrounding coil in *xy*-plane is maximal. Correspondingly, a 180° pulse (π pulse) will turn the magnetization to -*z*, where the NMR signal in *xy*-plane is minimal. The NMR signal decays due to the thermodynamic processes towards the thermal equilibrium orientated to B_0 (longitudinal relaxation). The magnetization of nuclei and the presession frequency is measured very precisely in order to explore the chemical environment of the nuclei, which is the basis of NMR spectroscopy. With the help of the mathematical approach of the Fourier transform (FT) the decreasing measured signal over time (free induction decay (FID)) is transformed to intensity over frequency signal (NMR spectrum) (Abragam 1989).

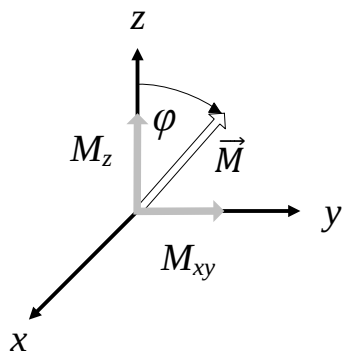

Figure 3-1: Resulting magnetization vector $\vec{M}$ (white indicated macroscopic magnetization) in a rotating coordination system. $\vec{M}$ has a component in *z* and in *xy* direction (gray indication). The magnetization is modified (by the flip angle φ) by the application of a radio frequency (rf) pulse.

Relaxometry

After excitation, the transverse magnetization $M_{x,y}$ decays over time (often exponentially). This process is defined as transverse relaxation characterized by the time constant T_2 (spin-spin-relaxation in s). The relaxation by which the net magnetization reestablishes in *z* direction is the longitudinal relaxation characterized by T_1 (spin-lattice-relaxation in s).

Longitudinal relaxation is based on losing energy to the environment (lattice) and re-establishment of the magnetization in *z*-direction by

$$\frac{dM_z}{dt} = -\frac{M_z - M_0}{T_1}. \qquad \text{Equation 3-7}$$

Equation 3-7 is the *z*-component of the Bloch equations in the rotating frame. The solution is given by

$$M_z(t) = M_0 \cdot \left(1 - e^{-\frac{t}{T_1}}\right). \qquad \text{Equation 3-8}$$

Transverse relaxation occurs due to the magnetization decay of the spins by losing their phase coherence. Energy will be transferred within spins by molecular interactions. The net magnetization $M_{x,y}(0)$ in *xy*-plane in the rotating coordinate system returns to zero, and the signal attenuates with time by

$$\frac{\mathrm{d}M_{\mathrm{x,y}}}{\mathrm{d}t} = -\frac{M_{\mathrm{x,y}}}{T_2}. \qquad \text{Equation 3-9}$$

The solution is given by

$$M_{x,y}(t) = M_{x,y}(0) \cdot e^{-\frac{t}{T_2}}. \qquad \text{Equation 3-10}$$

Inhomogeneity of the external magnetic field causes additional spin dephasing (with different dephasing rates) contributing to transverse magnetization decay T_2. The effective T^*_2 is then described by $\frac{1}{T_2^*} = \frac{1}{T_2} + \gamma \Delta B_0$. T_2 is the sample related, irreversible part of the decay, which has to be distinguished from the inhomogeneity contributions, which can be refocused by appropriate NMR sequences.

Both relaxation times, T_1 and T_2, are material specific parameters which are influenced by the molecular surrounding of the spins. Series of defined rf-pulses (amplitude, frequency and duration) are applied in specific pulse sequences to achieve the desired NMR signal where T_1 or T_2 can be determined (Callaghan 1991, Kimmich 1997). In MRI, often a weighting is sufficient for a specific image contrast. This can be realized by e.g. varying the acquisition parameters T_R (time in s between repeated experiments) and τ_E (echo time in s between the excitation, refocusing and acquisition of the magnetization echo). The measured NMR signal will depend on the degree of relaxation within these specific time intervals. This applies also to imaging as explained in Figure 3-2.

Magnetic resonance imaging

The spatial encoding in MRI is based on field gradients which overlay with B_0. The magnetic field has then a magnetic field gradient (G in T/m) in x, y, and z. Since the Larmor frequency (ω_0) is proportional to the magnetic field (B_0), the magnetic field gradients enable a linear encoding of position (r in m):

$$\vec{\omega}_0 \left(\vec{B}_0, \vec{G}, \vec{r}\right) = \gamma \cdot \vec{B}_0 + \gamma \cdot \vec{G} \cdot \vec{r}. \qquad \text{Equation 3-11}$$

In Equation 3-11, r refers to all directions in space, but in the following only one spatial direction will be considered. For MRI, a series of different field gradients need to be applied in a specific order (Figure 3-2): a slice selection gradient (G_s) selects a specific slice within the sample. A phase encoding gradient (G_{ph}) and frequency encoding gradient (G_r) realize the two-dimensional spatial resolution in the imaging of the slice by phase and frequency encoding. By 2D-Fourier-transform reconstruction, the image can be obtained (Kimmich 1997).

Frequency selective rf-pulses with frequency bandwidth ($\Delta\omega$) are combined with a slice selection gradient (G_s). $\Delta\omega$ corresponds to the Larmor frequencies in a particular slice in the sample determined by the slice selection gradient. The slice selection gradients can be applied in either spatial direction. For a slice selection in xy-plane (axial slice), G_s would be applied along z. A phase encoding gradient (G_{ph}) is

switched on between the excitation and refocusing or detection of the signal. G_{ph} encodes the phase of the spin's precession spatially by altering the Larmor frequency in the gradient direction, in our example the *y*-direction. This causes a spatial dependence of the frequency which is manifested as a spatially dependent phase after switching off G_{ph}. Phase encoding can be realized by combining a spin echo (SE) experiment (90° followed by a 180° rf-pulse) with the corresponding gradients, see Figure 3-2. The number of phase encoding steps determines the digital resolution of the images along the phase encoded direction. During reading the SE, a frequency encoding gradient (G_r) is applied e.g. in *x*-direction. G_r encodes the precession frequencies along *x* and allows the allocation by detection of the frequencies. The time between the single experiments (total number of *n*) is the repetition time T_R in s. The time interval between the excitation, refocusing and acquisition is the echo time τ_E in s.

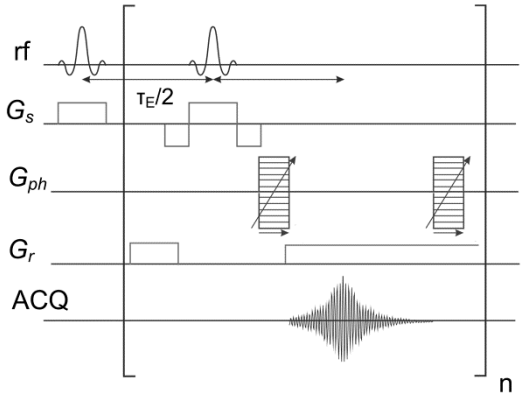

Figure 3-2: Standard MRI imaging experiment (multi slice multi echo) and simplified radio frequency- and field gradient pulse scheme where a spin echo (SE) is acquired after the textbooks of Kimmich (1997) and Callaghan (1991) (acquisition: ACQ). A slice selection gradient (G_s) enables the multiple slice selection within the sample. Two-dimensional images can be reconstructed when applying phase (G_{ph}) and frequency (G_r) encoding along two different spatial coordinates.

Using e.g. a multi-slice-multi-echo (MSME) experiment, several slices in different orientations (axial, sagittal, and coronal) can be acquired within one experiment repeating the sequence in Figure 3-2. Compared to other techniques, the fluid flow can be measured directly and *non-invasively* by MRI without the application of contrast agents or dyes. MSME enables a time-of-flight-experiment (TOF) where flow velocities can be visualized via the deformation of saturation stripes (Kimmich 1997). Furthermore a measurement via flow phase contrast (FLOW-PC) imaging was performed based on phase changes which can be associated with fluid mass flow during the experiment (Gatehouse *et al.* 2005). For further details please see chapter 7.2.

3.2.2 Biofilm imaging

As most biofilms are multispecies and highly heterogeneous systems - there are no standardized qualitative and quantitative methods for the measurement of biofilms. To better understand the structure and functionally of biofilms, imaging techniques have given a major contribution. Microscopic techniques such as light microscopy, confocal laser scanning microscopy (CLSM), Raman microscopy and electron microscopy enable to study the physical structure and morphology, as well as chemical composition of biofilms on different scales (Neu *et al.* 2010, Wagner *et al.* 2010b). Biofilm structure parameters, such as the biofilm thickness and biofilm coverage can be obtained. For example CLSM allows the selective visualization of the EPS matrix (by staining protocols) in on the µm-scale (Staudt *et al.* 2004, Wagner *et al.* 2009). New analytical approaches, as for example optical coherence tomography (OCT) demonstrate the development of biofilms (Li *et al.* 2016) and their mechanical properties, as deformation *non-invasively* with a spatial resolution down to few µm (Blauert *et al.* 2015). Additionally to imaging, 1D and multidimensional modeling improved the general understanding about biofilm processes involving microbiological processes, hydrodynamics and chemistry to describe for example biofilm growth under changing environmental conditions (Horn and Lackner 2014, Wanner 2006). There are also few newer approaches where imaging and modeling are combined (Li *et al.* 2015).

An ideal analytical tool allowing the combination of biofilm imaging and the investigation of the biofilm-bulk phase is MRI. Compared to traditional microscopy techniques having certain limitations concerning *in-situ* observation and invasiveness, such as electron microscopy (Neu *et al.* 2010), MRI offers a multifaceted application for a *non-invasive* and *non-destructive* investigation of biofilm systems. Therefore, MRI has strong potential in biofilm research being especially suitable for the analysis of thick biofilms at the µm-scale and mm-scale (Morgenroth and Milferstedt 2009, Ramanan *et al.* 2013). Biofilms are composed of bacterial cells embedded in a gel-like EPS matrix which contain various organic substances (e.g. biopolymers, lipids, proteins), see section 2.1.2. However, the entire biofilm consists to up to 95% of water (Neu *et al.* 2010) located in intercellular space, cell membranes and intracellular space. The T_1 and T_2 relaxation times for water in the biofilm are shortened compared to the free bulk water - this effect is the most used base for biofilm imaging *via* MRI. Generally, T_2 relaxation measurements are preferred because their acquisition is faster. The enhanced relaxation is probably due to the hampered motion of ^{1}H nuclei within the biofilm and molecular exchange of the protons in bulk water and biopolymers (EPS). The molecular exchange and interactions happen on a time scale of less than µs. The T_2 relaxation time of pure water is long (in the rage of 1-2 s) whereas the T_2 of biopolymers is comparably short in the range of 10 - 100 ms. The measured T_2 of the biofilm is then the average relaxation time (100 - 200 ms) (Brownstein and Tarr 1979, Codd *et al.* 2011, Hoskins *et al.* 1999, Lens *et al.* 1997, Seymour *et*

al. 2004a, Vogt *et al.* 2013). To some extent this also applies to T_1 relaxation, however a different image contrast is exhibited, see Figure 3-3. For the investigation of biofilms, the spin density (number of spins per volume ρ_{PD} in moles/m^3) might also be of interest. The spin density can be correlated with the image intensity. Furthermore, T_1 and T_2 relaxation times and spin density can give indications for the composition of single components within a biofilm matrix being either liquid (signal) or solid (no signal intensity in standard MRI) or gas (no signal intensity in standard MRI). In the late 90's for the first time, biofilms were imaged via T_2 relaxation maps (Hoskins *et al.* 1999). More recently, the shift to lower T_2 relaxation times found for blank compared to biofouled systems (tubes, porous media) was used to monitor biofilm growth (Codd *et al.* 2011, Manz *et al.* 2003, Sanderlin *et al.* 2013). MRI has been applied to measure local flow velocities, local shear stress and the impact of biofilm distribution, growth and detachment on water flow fields surrounding biofilms grown in tubes, flow cells, biofilm carriers and capillary bioreactors (Herrling *et al.* 2015b, Manz *et al.* 2003, 2005, Nott *et al.* 2005a, Seymour *et al.* 2004a, Wagner *et al.* 2010a). So far, the investigated biofilm systems were limited to laboratory scale, which were adapted to meet the requirements of the MRI tomograph and probes. In 2015, the first experiments for *in-situ* biofilm detection in soils using an outdoor NMR probe were conducted, first, in a laboratory well-bore environment, then in a field study (Kirkland *et al.* 2015a, Kirkland *et al.* 2015b).

Examples for a microscopic optical image proton density (PD), T_1- and T_2-weighted and images of biofilm systems used in this dissertation are depicted in Figure 3-3 (acquisition parameter in Table 5-2). The carrier supported biofilm systems are employed in experiments in chapter 5, 6 and 7. The image contrast between biofilm and bulk water strongly depends on the MRI acquisition parameters (Metzger *et al.* 2006).

- The PD image was acquired at long T_R (10 s) and short τ_E (3.2 ms) for minimizing the relaxation weighing of the NMR signals. It is obvious that the biofilm and the bulk water cannot be distinguished due to comparable proton densities.
- In the T_2-weighted image τ_E was set to 50 ms (long compared to T_2 relaxation) and T_R was kept long in order the T_1 relaxation of the protons is completed (10 s). The biofilm appears as dark fluffy structures attached to the carrier material and the bulk water appears again bright. This is due to the biofilm's shorter T_2.
- In the T_1-weighted image T_R was set to 800 ms (short compared to T_1 relaxation) and τ_E to 4.5 ms: the biofilm appears as a bright fluffy layer attached to the carrier material, and the bulk water appears darker due to the shorter T_1 relaxation of the biofilm.

There are different artifacts which can occur in MRI images, that show a locally distorted intensity e.g. at gas-liquid interphase or by ferromagnetic objects.

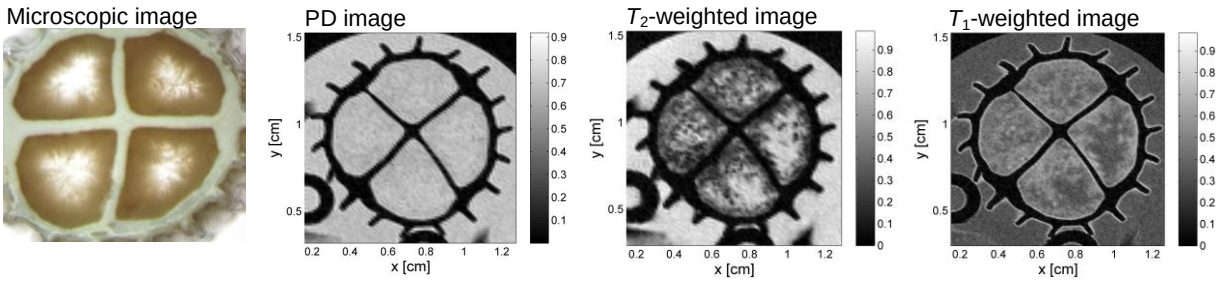

Figure 3-3: Microscopic optical image, PD, T_1-weighted and T_2-weighted images of a biofilm cultivated on a cylindrical carrier (diameter: 9.2 mm). The solid carrier material consists of polyethylene and shows no signal in the presented MRI images. The in-plane resolution was 76 µm for the T_1-weighted image and 152 µm for T_2-weightes and PD images. The measurements were performed on a 200 MHz MRI tomograph (Bruker Avance 200 SWB, Bruker BioSpin GmbH, Rheinstetten, Germany). For acquisition parameter, please see Table 5-2.

3.2.3 Imaging of nanoparticles within biofilm matrix

Image contrast is the relative difference of the signal intensity between two sample regions. In MRI the image contrast mainly depends on the nature of the sample and on the device specific and acquisition parameters. To increase the informative value of MRI images, MRI contrast agents - such as magnetic nanoparticles (Fe_3O_4-NP) - are commonly applied to enhance the image contrast between specific compartments and to obtain functional information about the sample. In medicine this approach is widely used for diagnostic purposes (Weishaupt *et al.* 2006). This dissertation focuses on contrast agents which contain paramagnetic ions such as iron in the used Fe_3O_4-NP. The paramagnetic property of the contrast agents add a further relaxation process (T_1 or/and T_2 relaxation times) of ^1H nuclei (free water) in the presence of large magnetic moments induced by free electrons (Callaghan 1991, Kimmich 1997). Particulate contrast agents, such as superparamagnetic iron oxide particles (SPION) can be applied for contrast enhancement (Mahmoudi *et al.* 2011a). But also many molecular contrast agents are available, which carry transition or lanthanide metal ions e.g. iron (Fe^{3+} and Fe^{2+}) (Ito *et al.* 2005) or gadolinium (Gd^{3+}) (Caravan *et al.* 1999, Chan and Wong 2007, Guthausen *et al.* 2015, Machado *et al.* 2014), but also other paramagnetic ions as Ni^{2+} Cr^{3+}, Co^{2+}, Ti^{2+}, Nd^{3+}, Th^{4+} and Mn^{2+} (Kruk *et al.* 2004, Phoenix *et al.* 2008). The contrast agents might be toxic. Therefore, MRI contrast agents need to be chemically stable, biocompatible, rapidly excreted and soluble in water (Aime *et al.* 1998) to minimize negative effects on humans and environment. In the field of biofilm research the application of MRI contrast agents is a promising approach for the characterization of biofilm structure, and mass transport, and especially, in the context of studying the fate of ENP in the environment. This approach represents one step towards the

non-invasive visualization of ENP in the undisturbed biofilm matrix as most studies use *destructive* imaging techniques, such as electron microscopy to proof the attachment of ENP to biofilms (Fabrega *et al.* 2009b, Limbach *et al.* 2008, Rottman *et al.* 2012).

The next paragraphs presenting the basics of contrast enhancement are simplified and without claim to completeness. For more specific information on the mechanisms of relaxation enhancement please consult text books (Bertini *et al.* 2001, Lauffer 1987).

Paramagnetic relaxation enhancement

The visualization of contrast agents within a heterogeneous sample by MRI is based on the change of the relaxation properties (T_1 or/and T_2 relaxation times) of nearby molecules due to paramagnetic relaxation enhancement (PRE). The efficiency of a contrast agent to enhance the contrast is described by their relaxivity r_i (i = 1, 2). r_i (L/(mg·s)) is defined by the slope of relaxation rate $\frac{1}{T_i}$ (1/s) as a function of the contrast agent concentration c (mg/L). The relaxivity of a given contrast agent is mainly influenced by temperature, pH and magnetic field strength. Generally, a prerequisite for T_1 and T_2 relaxation enhancement is a positive magnetic susceptibility e.g. paramagnetism or superparamagnetism caused by unpaired electrons in the contrast agent. The magnetic moment of an electron is much larger than the nuclear magnetic moment of a proton. Therefore it induces local magnetic field fluctuations which can be in a frequency range of the Larmor frequency of the protons of the surrounding molecules and enhance their relaxation. Strong time independent, i.e. static local differences in magnetic susceptibility within a sample can lead to susceptibility artifacts. The NMR relaxation of molecules in the neighborhood of a contrast agent moiety is determined by a complex set of processes on different time scales including:

- molecular rotations characterized by the correlation time τ_R: the molecular rotation can be described by the molecular tumbling time which depends on the size of the molecule.
- diffusion (τ_D): The translational diffusion and therefore the distance of the observed molecules in the bulk nearby the contrast agent need to be considered for the PRE.
- chemical exchange (τ_M): the residence time for chemical exchange between the molecules and the contrast agent.
- electron spin correlation time (τ_E): interactions between unpaired electrons (dipoles) of the contrast agent and the protons of observed molecules enhance the relaxation processes, therefore this time scale play a major role.

Generally spoken, the effect of the contrast agent on the surrounding molecules is measured and not the contrast agent itself. The observed global relaxation rate $\left(\frac{1}{T_i}\right)_{ob}$ (i = 1, 2) (1/s) is the sum of the

contributions of molecular relaxation rate without contrast agent addition $\left(\frac{1}{T_i}\right)_w$ (mainly dominated by water) and the paramagnetic contribution $\left(\frac{1}{T_i}\right)_p$ given by

$$\left(\frac{1}{T_i}\right)_{ob} = \left(\frac{1}{T_i}\right)_w + \left(\frac{1}{T_i}\right)_p . \qquad \text{Equation 3-12}$$

As mentioned before, there is a linear dependency of observed relaxation rate $\left(\frac{1}{T_i}\right)_{ob}$ (i = 1, 2) and the contrast agent concentration c (mg/L) and the slope represents the relaxivity r_i (L/(mg·s)), see Equation 3-13.

$$\left(\frac{1}{T_i}\right)_{ob} = \left(\frac{1}{T_i}\right)_w + r_i \cdot c \qquad \text{Equation 3-13}$$

For more specific information please see Appendix A1.

T_1 and T_2 contrast agents

Although T_1 or T_2 relaxation processes are coupled, contrast agents can be categorized in preferentially changing the T_1 or T_2 relaxation of protons in water molecules. Contrast agents which mainly shorten T_1 are called positive contrast agents. Those positive enhancing agents will appear as bright regions in T_1-weighted MRI by increasing the signal intensity. Examples are paramagnetic molecules carrying gadolinium ions (Gd^{3+}), such as the contrast commonly used medical contrast agent Gadovist (Gd-DO3A-butrol6). Negative contrast agents preferentially shorten the T_2 relaxation by faster spin dephasing. Due to the signal loss, the regions where the negative contrast agents are located appear darker in T_2-weighted MRI images. Examples for Fe_3O_4-NP are BNFdextran and nanomag-D-spio used in this dissertation (chapter 5).

Magnetic resonance imaging of contrast agents for biofilm studies

The spatio-temporally resolved imaging of paramagnetic compounds or ions in biofilm systems has been investigated by only few research groups. On the one hand, for easier data processing MRI contrast agents (e.g. Gd^{3+}-based contrast agents) were applied to enhance the contrast between bulk water and biofilm (Manz *et al.* 2003, Seymour *et al.* 2004a). On the other hand, contrast agents can be applied to generate specific information about biofilm systems and mass transport. The application of contrast agents using MRI gives indications about the

- physical heterogeneity, structure and transport properties of a biofilm system,
- fate of contrast agents in biofilm system and
- partly functionality of a biofilm system.

First approaches in biofilm research have been conducted in the late 90's where the contrast generation, spatial distribution and adsorption of e.g. Cu^{2+} ions in alginate (model biofilm and spiked with microbial cells) were investigated (Nestle and Kimmich 1996). Further on, the mass transport (e.g. diffusion coefficients) and the immobilization of contrast agents was explored by concentration maps based on T_1 and T_2 values in homogenous biofilms (Phoenix and Holmes 2008, Phoenix *et al.* 2008, Phoenix *et al.* 2009, Ramanan *et al.* 2013). This was mainly done in 2D, but also 3D measurements are possible shown in a work about iron ion transport in granular biofilms (Bartacek *et al.* 2009). In the field of environmental remediation and biological WWT, continuing studies deal with the biofilm induced deposition of heavy metals in a bioreactor (porous media). MRI studies enabled to visualize the heavy metal removal (La^{3+}, Cu^{2+}) from wastewater and gave insights into the processes in a bioreactor (Nott *et al.* 2005b, Nott *et al.* 2001). In 2008, the first concentration maps describing the bioremediation of water contaminated with Co^{2+} appeared (von der Schulenburg *et al.* 2008a). Chrome species can be differentiated with MRI assessing the reduction of Cr^{4+} to Cr^{3+} using a biofilm-palladium catalyst in a porous media. Here, the Cr^{3+} concentration was correlated with T_1 relaxation. Besides the monitoring of the biochemical reaction, blocking in the reactor cell was analyzed as well (Beauregard *et al.* 2010). Most of MRI studies repetitively employ microbial monocultures and, thus, studies approaching real multispecies biofilms in combination with contrast agents are still missing. Furthermore, to the author's knowledge, there is no work available using MRI with the aim to specifically examine the interactions and biosorption of ENP with biofilm systems. Steps towards the investigation of the fate of ENP in the environment using MRI are demonstrated by transport studies through porous media (without biofilms) (Baumann and Werth 2005, Cuny *et al.* 2015, Lakshmanan *et al.* 2015).

4 INFLUENCE OF THE WATER MATRIX ON INTERACTIONS OF Fe_3O_4-NP WITH GRANULAR BIOFILMS*

*This chapter has been published in Science of the Total Environment (2015), volume 537: 43-50 in collaboration with K. L. Fetsch, M. Delay, F. Blauert, M. Wagner, M. Franzreb, H. Horn and S. Lackner.

4.1 Introduction

The increasing number of potential applications of ENP is likely contributing to their release into the global water cycle (Delay and Frimmel 2012, Gottschalk *et al.* 2013a, Gottschalk and Nowack 2011). After their release from industry and households, ENP are primarily found in receiving water bodies with WWTP as main point sources (Nowack and Bucheli 2007). ENP are partly removed from the WW by attachment to the biomass, such as sorption, without any special treatment step (Gomez-Rivera *et al.* 2012, Kiser *et al.* 2010, Park *et al.* 2013, Wang *et al.* 2012). For more specific information on the interactions of ENP with biomass from WWT, please see chapter 2.1.2. The removal of ENP can significantly differ considering different types of biomass. Activated sludge exhibiting a more fluffy physical structure is supposed to remove ENP more efficiently from the water phase than for example compact biofilms (Gu *et al.* 2014). This finding emphasizes the need to examine different types of biomass to understand the interactions, and further the mass flows of ENP. Additionally, WWT systems represent a highly complex environment for the interactions of ENP with the biomass, where numerous transformations, such as sulfidation or oxidation, significantly influence their fate (Kaegi *et al.* 2013, Kaegi *et al.* 2011). One of the most important factors for the interactions and fate of ENP is the chemical composition of surrounding water matrix. The chemistry of the water matrix affects the behavior of ENP, by e.g changing their particle properties (Delay *et al.* 2011, Schwegmann *et al.* 2010), see chapter 2.1.1. However, the evaluation of these processes in conjunction with the removal of ENP from the water phase is still a major challenge.

Therefore, this chapter used magnetic Fe_3O_4-NP coated with PVA (polyvinyl alcohol) as model ENP to trace their fate in compact granular biofilms from WWT. Based on their magnetic properties, Fe_3O_4-NP were selectively quantified by their magnetic susceptibility. This enabled for the first time, the *in-situ* quantification of Fe_3O_4-NP in both the water phase, and sorbed to the granular biofilm. With the aim to examine the distribution of Fe_3O_4-NP in granular biofilms, 18 h batch experiments were conducted. The main goals of this chapter were to:

- Investigate the interactions between Fe_3O_4-NP and granular biofilms with respect to chemical parameters of the water matrix.
- Investigate the effect of different granular biofilm size fractions on the removal of Fe_3O_4-NP from the water phase.
- Quantify the biosorption and removal of Fe_3O_4-NP by the granular biofilm matrix by a proper mass balance.

4.2 Materials and Methods

4.2.1 Fe_3O_4-NP: properties, preparation and quantification *via* MSB

The used synthetic Fe_3O_4-NP (chemagen Technologie GmbH, Baesweiler, Germany, (c_{stock}(Fe) = 25 g/L suspended in water)) consisted of superparamagnetic magnetite (Fe_3O_4) cores (~ 15 nm) coated with polyvinyl alcohol (PVA, $(C_2H_4O)_x$). The organic coating (steric) stabilizes the particles and prevents particle oxidation and iron release. The particle size and the zeta potential of Fe_3O_4-NP were measured using dynamic light scattering and laser DOPPLER anemometry, respectively ((n = 10); refractive index for iron oxide: 2.42; adsorption coefficient: 0.01, Zetasizer Nano ZS, Malvern Instruments, Worcestershire, United Kingdom). The prepared suspensions of Fe_3O_4-NP formed larger agglomerates with a size of 194 ± 13 nm (polydispersity index of 0.17), as it is common in natural and technical water systems (Petosa *et al.* 2010). The zeta potential was -7 ± 0.3 at pH value of 8. The isoelectric point was at pH ~ 5.5 - 6 indicating that agglomeration was favorable to happen. Long term stability experiments were conducted for Fe_3O_4-NP in suspensions with ultrapure water (Milli-Q, Merck Millipore, Billerica, MA, USA) over 100 h, see Figure 4-1. The suspensions were stored at room temperature and the concentration of Fe_3O_4-NP in the bulk phase was measured at different time points. The Fe_3O_4-NP were stable over the whole time period.

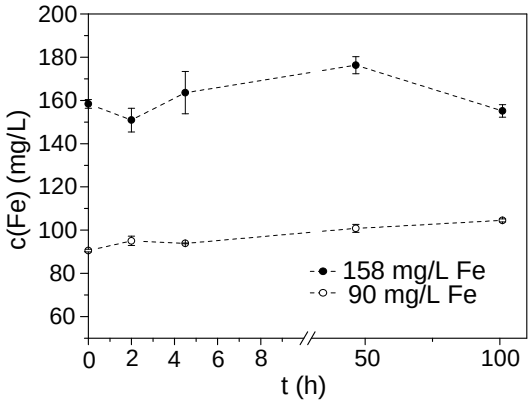

Figure 4-1: Long term stability of suspensions of Fe_3O_4-NP with PVA coating in ultrapure water for initial concentrations of 158 mg/L Fe and 90 mg/L Fe. The concentrations were measured in the bulk of the suspension using MBS.

For preparation prior to the batch experiment, suspensions of Fe_3O_4-NP were diluted (ratio 1:10 and 1:50) with ultrapure water, stirred intensively, and settled for 20 h. The decanted supernatant of those suspensions was further diluted to the desired concentration. For the batch experiments, initial concentrations of Fe_3O_4-NP of c_0(Fe) = 100; 200; 1000 mg/L were used to trace the distribution of Fe_3O_4-NP in the granular biofilm. Chosen concentrations were intentionally higher than environmental relevant concentrations of ENP (Gottschalk *et al.* 2009) to elucidate the detailed interactions with the biofilm. A calibration was performed to correlate the measured magnetic susceptibility (χ_V) with the Fe concentration (c(Fe)) of the Fe_3O_4-NP (Figure 4-2). For further information about the magnetic susceptibility, please see section 3.1.

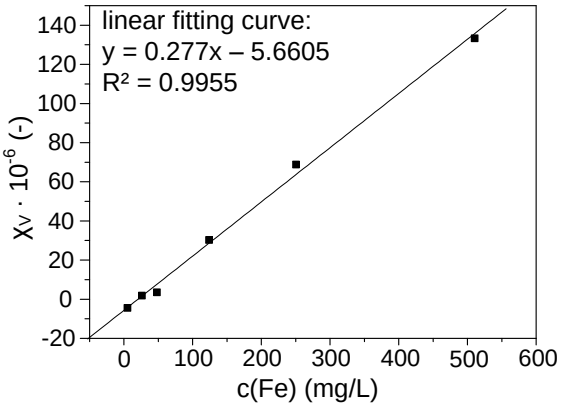

Figure 4-2: Calibration curve of the volume magnetic susceptibility χ_v (n = 3, y-axis) for suspensions of Fe_3O_4-NP (with PVA coating) in ultrapure water and the iron concentration (x-axis) determined by ICP-OES. Standard deviations are too small to be recognized (< 10 %). The working range of the calibration was between 5.5 - 511 mg/L Fe.

For the calibration, the iron concentration was determined by inductively coupled plasma optical emission spectrometry (ICP-OES, Varian VistaPro, Agilent Technologies, Santa Clara, USA; detection limit for Fe: 10 µg/L) after *aqua regia* digestion (HCl and HNO_3 at 200 °C; CEM Mars V, Kamp-Lintfort, Germany). The measurements were done immediately after sampling to achieve reproducible results. Fe_3O_4-NP were also quantified based on their magnetism with the magnetic susceptibility balance (MSB AUTO, Sherwood Scientific, Cambridge, England, range of operation: χ_V of $0.13 \cdot 10^{-6}$ (SI units)). To measure the magnetic susceptibility, a sample volume of 200 µL was filled into the glass sample tube after zeroing the MSB. Before the measurement with the MSB, the filled sample tube was weighted for the mass susceptibility measurement, then, the sample tube was inserted into the MSB and the measurement was automatically undertaken (measurement time 60 s). For more information about the theory of the magnetic susceptibility please see chapter 3.1.

4.2.2 Preparation of granular biofilm and characterization *via* MSB

The granular biofilms were collected from the sides-stream treatment unit for autotrophic nitrogen removal at the WWTP in Heidelberg, Germany. After rinsing with tap water, the granular biofilms were sieved to size fractions of 100 - 250; 250 - 500; 500 - 800 µm to simplify the model system and remove the flocculent suspended biomass. Three biofilm size fractions were chosen to investigate the heterogeneities within one type of granular biofilm, see Figure 4-3.

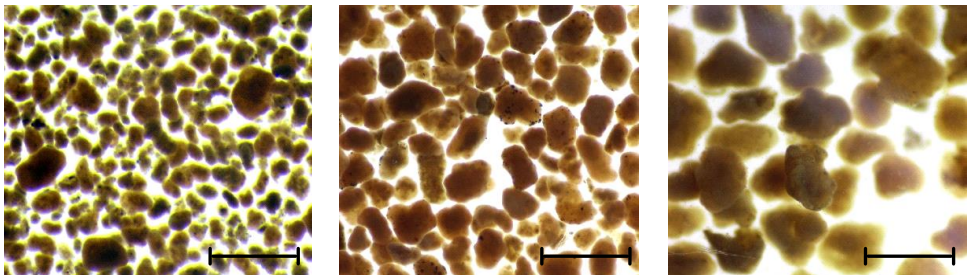

Figure 4-3: Stereomicroscopic images of the three size fractions of granular biofilm in absence of Fe_3O_4-NP (left to right): 100 - 250 µm; 250 - 500 µm; 500 - 800 µm at t = 0 (before the experiment). The scale bar corresponds to 1 mm.

The used volume of the granular biofilm in the batches (c(TSS) = 2 g/L) was 1 mL (size fraction: 100 - 250 µm), 1 mL (250 - 500 µm) and 1.5 mL (500 - 800 µm), respectively. χ_V of the three granular biofilm fractions were measured prior to the addition of Fe_3O_4-NP by MSB, to confirm the diamagnetism (χ_V comparable to water) of the granular biofilm (see values in table Table 3-1). The physical structure and morphology of the granular biofilm were imaged by means of optical coherence tomography (OCT, OCP930SR, Thorlabs GmbH, Dachau, Germany). The organic matter (OM) in the supernatant of the settled granular biofilm (settling time = 1 min) was quantified by chemical oxygen demand (COD) using

tests kits (LCK 414, HACH LANGE GmbH, Düsseldorf, Germany), by the total organic carbon (TOC), and by the dissolved organic carbon (DOC) (Shimadzu, Duisburg, Germany). COD, TOC, and COD measurements were performed only in absence of Fe_3O_4-NP to avoid irreversible contamination of the analytical equipment. Total suspended solid content (TSS) was determined according to European standard methods (DIN-EN-12880 February 2001). The release of ions from the granular biofilm to the supernatant (Ca^{2+}, K^+ and Mg^{2+}) was quantified by ICP-OES after 18 h shaking time. To minimize biological activity the granulated biofilm was stored in tap water at 4 °C. For the experiment, the fresh and chilled biomass was used.

4.2.3 Procedure of batch experiments

Batch experiments (V_{total} = 30 mL) were conducted in duplicates as volume reduction batch experiments. The granular biofilms (c(TSS) = 2; 10 g/L) were spiked with the respective suspension of Fe_3O_4-NP (c_0(Fe) = 100; 200; 1000 mg/L) and shaken overhead for 18 h. Demineralized water was used as medium to keep the electrical conductivity low. The pH value in the batch was adjusted to pH value 7 - 8 before the experiment (using 0.01 mol/L HCl and 0.01 mol/L NaOH). A soft shaker program of 10 rpm was chosen to avoid extended physical damage to the granular biofilm. After a contact time of 0 min, 10 min, 20 min, 30 min, 60 min, 120 min, 180 min and 18 h (1080 min) the granular biofilm was gravitationally settled (60 s). An equilibration time of 18 h was chosen (rather than typical 3 - 4 h), assuming that the maximum "sorption" capacity was not reached. The settling time of 60 s was chosen due to the fast sedimentation of the granular biofilm (TSS = 2 and 10 g/L), which allows to investigate the interaction of the Fe_3O_4-NP with the granular biofilm in short-term within the initial phase. Sedimentation was chosen as separation step because centrifugation could have unintentionally reduced the concentration of Fe_3O_4-NP in the water phase. The supernatant was sampled 2 cm below the water surface, and Fe_3O_4-NP were quantified using MSB (n = 3, measurements of a single sample). Time series of χ_V, electrical conductivity, pH value (using conventional electrodes), COD, TOC and DOC were measured in the batches. Control batches containing only Fe_3O_4-NP and only granular biofilm were conducted alike. The core material and surface functionalization (PVA) of Fe_3O_4-NP are expected to be stable during the whole batch experiment (no granular biofilm addition), because no increase in the electrical conductivity, nor in pH value was detected; χ_V also kept constant. During all batch experiments without Fe_3O_4-NP, no change in the magnetic susceptibility was observed meaning that the granular biofilm did not release substances with detectable magnetism.

4.2.4 Mass balance in batch experiment

To quantify the removal of Fe_3O_4-NP from the supernatant, the removal efficiency was calculated using the ratio of c_0(Fe) and $c(Fe)_t$, according to other studies (Park *et al.* 2013). In this work the term "biosorption" is used, which summarized the total chemical and physical sorption mechanisms of Fe_3O_4-NP to the granular biofilm by sorption to the cells and EPS as well as bio-uptake characterized by other studies (Kiser *et al.* 2010, Kloepfer *et al.* 2005). To gain information about the reversibility of the attachment of Fe_3O_4-NP, the magnetic susceptibility of the granular biofilm was also measured after rinsing at the end of the experiment (after 18 h). For rinsing, the granular biofilm was sampled with a conventional syringe, placed on a sieve (grid size: 66 µm), and carefully rinsed with 10 mL of demineralized water. Afterwards the rinsed granular biofilm was re-suspended in demineralized water and measured using MSB for the quantification of Fe_3O_4-NP. With the help of the magnetic susceptibility, an accurate mass balance of the Fe_3O_4-NP was set up for each batch experiment to evaluate the distribution of Fe_3O_4-NP by

$$m_{\text{Fe } t = 0\text{ h}} = m_{\text{Fe sample } t = 18\text{ h}} + m_{\text{Fe supernatant } t = 18\text{ h}} + m_{\text{Fe biosorption } t = 18\text{ h}} + m_{\text{Fe losses } t = 18\text{ h}}. \quad \text{Equation 4-1}$$

$m_{\text{Fe } t = 0\text{ h}}$ is defined as the initial mass of Fe added to the batch vessel. The term $m_{\text{Fe sample } t = 18\text{ h}}$ is the mass of Fe continuously removed from the batch as samples (volume reduction batch experiment) assuming a homogenous distribution of the particles in the batch. The value of $m_{\text{Fe supernatant } t = 18\text{ h}}$ defines the Fe_3O_4-NP which were still in the supernatant of the settled biomass after a contact time of 18 h (Equation 4-1). $m_{\text{Fe losses } t = 18\text{ h}}$ is the fraction of Fe_3O_4-NP which could not be recovered by sampling. However, these Fe_3O_4-NP can still be located in the batch experiment attached to suspended OM. The rest of the Fe_3O_4-NP was assumed to be lost during the experimental procedure. The total biosorption ($m_{\text{Fe biosorption } t = 18\text{ h}}$) is the sum of Fe_3O_4-NP attached to the biomass ($m_{\text{Fe granular biofilm } t = 18\text{ h}}$) and being located in the interspace between the single granular biofilms ($m_{\text{Fe interspace } t = 18\text{ h}}$):

$$m_{\text{Fe biosorption } t = 18\text{ h}} = m_{\text{Fe granular biofilm } t = 18\text{ h}} + m_{\text{Fe interspace } t = 18\text{ h}}. \quad \text{Equation 4-2}$$

4.3 Results and Discussion

4.3.1 Influence of the granular biofilm on the chemistry of the water matrix

For a deep understanding of the interactions between Fe_3O_4-NP and the different size fractions of granular biofilm, a closer look at the chemistry of the water matrix and biofilm structure during the batch

experiment was necessary. The development of the electrical conductivity during the batch experiments with granular biofilm (no Fe_3O_4-NP) showed the expected increase of the mineral content over time (from 20 µS/cm to 170 µS/cm). Relevant ions for the destabilization of Fe_3O_4-NP were found in concentrations of 8 - 18 mg/L (Ca^{2+}), 1.0 - 1.2 mg/L (Mg^{2+}) and 0.8 - 1.2 mg/L (K^+) for all granular biofilm size fractions after 18 h shaking time, see table Table 4-1.

Table 4-1: Ion concentrations in the water phase of batch experiments after 18 h shaking time (no Fe_3O_4-NP) for the three granular biofilm size fractions.

biofilm size (µm)	Ca^{2+} (mg/L)	Mg^{2+} (mg/L)	K^+ (mg/L)
100 - 250	17.6 ± 0.1	1.0 ± 0.0	1.2 ± 0.0
250 - 500	13.6 ± 0.1	1.0 ± 0.0	1.5 ± 0.0
500 - 800	8.00 ± 0.1	1.2 ± 0.0	1.0 ± 0.0

In contrast, heterogeneities within the granular biofilm were found for the organic matter (OM) content (Figure 4-4, A and B). The granular biofilm size fraction of 250 - 500 µm discharged the most OM. This finding did not correlate with the specific surface area of the granular biofilm size fractions nor with the volatile suspended solid content (VSS), which was between 30 - 42 %.

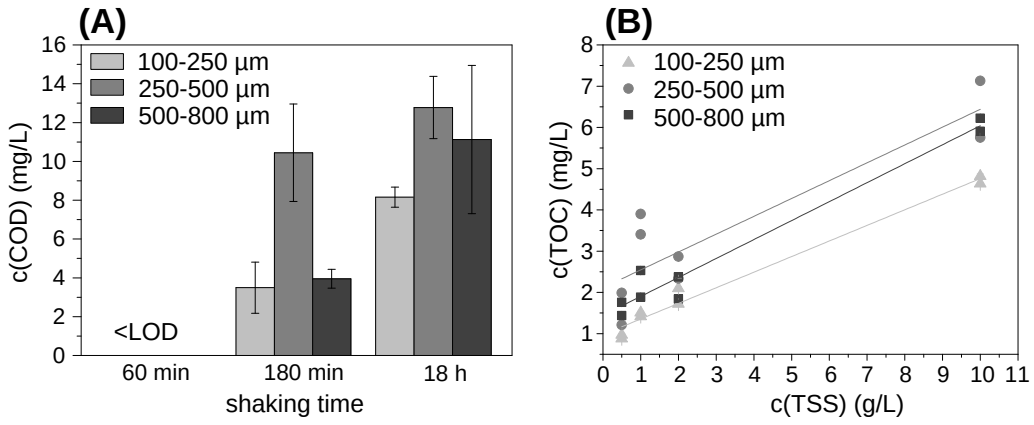

Figure 4-4: Temporal development of the water chemical parameter in batch experiments (blank - no addition of Fe_3O_4-NP): (A) organic matter (batches in triplicates) and (B) correlation of *c*(TSS) and *c*(TOC) after 18 h shaking time (batches in duplicates (*n* = 1) indicated by data points). *c*(COD) for t = 60 min in (B) was below the limit of detection (LOD) of 3.7 mg/L.

Other reasons must be responsible for the enhanced OM release by the granular biofilm size fraction of 250 - 500 µm requiring further investigations. The TOC and DOC results revealed that 80 - 88 % of the OM released by all granular biofilm size fractions during the shaken batch experiment was particulate

matter. Consequently, the granular biofilms do preferentially release particulate OM, rather than dissolved OM. OCT images of the granular biofilm (Figure 4-5, spatial resolution: 8.6 µm/pixel) acquired before and after the batch experiments (no Fe_3O_4-NP) confirmed this finding. The images show the released particulate OM in the supernatant, just above the settled granular biofilm, indicated by the white ellipse. The granular biofilm size fraction of 250 - 500 µm released the most particulate OM followed by 500-800 µm. Furthermore, the three granular biofilm size factions showed a smooth and compact physical structure without fractures due to shaking.

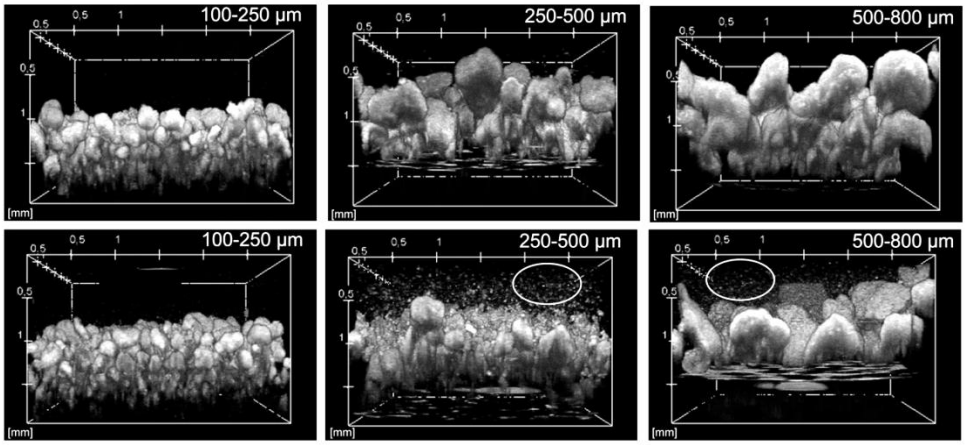

Figure 4-5: Optical coherence tomography (OCT) images (spatial resolution: 8.6 µm/pixel) of the settled granular biofilm size fractions before (upper row, t = 0) and after the batch experiment (lower row, t = 18 h) in the original medium of the batch in the absence of Fe_3O_4-NP. Particulate OM is released by the size fraction of 250 - 500 µm and 500 - 800 µm indicated by the white ellipse.

The temporal development of the pH value over the 18 h shaking showed a slight decrease from 7.6 to 7.1. The slight decrease in pH value and the slight increase of electrical conductivity and OM concentration probably resulted from disruption of extracellular polymeric substances (EPS) of the granular biofilm releasing, e.g. ions and proteins as it can occur in WWT systems. EPS can therefore strongly enhance removal of ENP from the water phase (Kiser *et al.* 2010). Summarizing, OM concentration and the electrical conductivity rose during the experiment and might be a key parameter for the behavior of Fe_3O_4-NP.

4.3.2 Removal of Fe_3O_4-NP from the water phase

Figure 4-6 shows the time resolved development of the iron concentration in duplicates during the batch experiments with Fe_3O_4-NP addition ((A) c_0(Fe) = 100 mg/L; (B) 200 mg/L). All data sets were acquired using MSB and were transferred into iron concentrations by the calibration curve shown in Figure 4-2. In the blank batch experiments without granular biofilm, the Fe_3O_4-NP were the most efficiently removed from the water phase, most likely due to homoagglomeration and sedimentation (Petosa *et al.* 2010).

However, long term stability experiments showed that Fe_3O_4-NP were stable over a period of 100 h in ultrapure water, see Figure 4-1, indicating that particle agglomeration was caused by the few ions present in the demineralized water (electrical conductivity < 50 µS/cm).

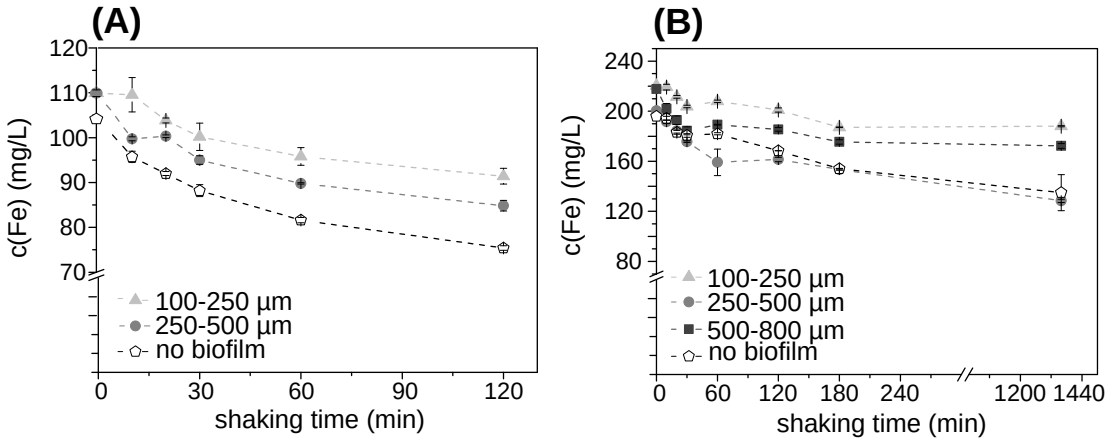

Figure 4-6: Temporal development of *c*(Fe) (mean values (*n* = 3), batches in duplicates) during the batch experiment with (A) c_0(Fe) = 100 mg/L and (B) c_0(Fe) = 200 mg/L for a TSS of 2 g/L for three different size fractions of granular biofilms. Please note that (B) has a break in the *x*-axis where the scale changes from 30 min to 120 min increments.

By spiking the batches with granular biofilms, Fe_3O_4-NP were stabilized compared to batches containing no biofilm, resulting in homogenization of the samples with smaller standard deviations Figure 4-6, A and B. These results are in accordance with the commonly known effect that OM stabilizes ENP suspension (Baalousha 2009, Delay *et al.* 2011, Lowry *et al.* 2012). Also in wastewater matrices the this effect has been recently observed: ZnO-NP and TiO_2-NP were stabilized by OM and the particle size remained constant, indicating that no significant destabilization of ENP and no particle agglomeration occurred (Zhou *et al.* 2015).

Within the three granular biofilm size fractions, *c*(Fe) of 250 - 500 µm decreased the most, followed by 500 - 800 µm, and finally 100 - 250 µm. *c*(Fe) quickly decreased within the first 60 min, possibly due to co-sedimentation with the granular biofilm, particle agglomeration, subsequent sedimentation, or electrostatic interactions leading to the attachment onto the granular biofilm (Brar *et al.* 2010). After 180 min no significant further decrease in the Fe_3O_4-NP concentration was found, unlike other studies where Ag-NP and TiO_2-NP in deionized water spiked with activated flocculent sludge were further reduced (Park *et al.* 2013). Results indicate that the physical structure of the used granular biofilm might hamper the removal of Fe_3O_4-NP. Figure 4-7 presents the removal efficiencies for the batches with c_0(Fe) = 200 mg/L (Figure 4-6, B) for the three granular biofilm size fractions.

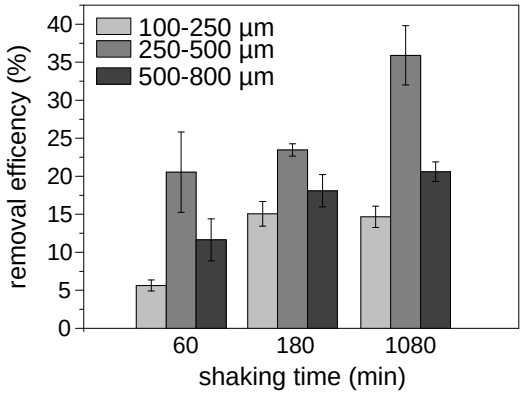

Figure 4-7: Removal efficiencies of Fe_3O_4-NP from the bulk water. Data was obtained by batches presented in Figure 4-6, (B) for c_0(Fe) = 200 mg/L at t = 60 min, t =180 min and t =18 h (averaged data for batches in duplicates).

For the size fractions of 100 - 250 µm and 500 - 800 µm the removal efficiency increased between 60 min and 180 min from 5.6 % to 15.1 % and from 11.6 % to 18.1 %, and remained stable after 180 min. The behavior of the size fraction 250 - 500 µm was different: the removal efficiency increased even after 180 min of contact time. An explanation lies in the dissolved and particulate OM release of the granular biofilm, which can either stabilize Fe_3O_4-NP compared to batches without biomass or lead to an accumulation on Fe_3O_4-NP in a certain phase in the batch, which makes the system rather complex. It should be noted that the results of OM concentrations (Figure 4-4) and removal efficiency (Figure 4-7) were arranged in the same order for the granular biofilm size fractions. The concentration of OM of the size fraction 250 - 500 µm was up to three times higher compared to the other two size fractions, and so was the removal efficiency. The enhanced removal of Fe_3O_4-NP of the size fraction 250 - 500 µm is assumed to be associated to the attachment of Fe_3O_4-NP to particulate OM in the water phase of the batch experiments just above the granulated biofilm, which was higher, compared to the other size fractions as visualized in OCT images. A synergetic effect can be given by the presence of relevant ions, such as Ca^{2+} released by the EPS of the granular biofilm, which can promote stabilization by coating of Fe_3O_4-NP with OM as well as flocculation through complexation with Ca^{2+}. This highlights that heterogeneities within the granular biofilms can influence the interaction and removal of Fe_3O_4-NP. As described in the introduction of this dissertation, depending on the experimental set-up, e.g. batch experiments (Kaegi *et al.* 2013, Rottman *et al.* 2012), pilot WWTP (Hou *et al.* 2013), sequencing batch reactors (Wang *et al.* 2012), or membrane bioreactors (Tan *et al.* 2015), the removal of various ENP can differ significantly and thus their fate cannot be directly compared or predicted (Westerhoff *et al.* 2013). However, compared to the summarized studies in Table 2-1, the presented results of the removal efficiency by granular biofilms is significantly lower.

4.3.3 Mass balance of Fe_3O_4-NP to granular biofilms

In recent scientific literature, ENP attached to biomass from WWT were often qualitatively validated by imaging techniques such as electron microscopy (Kim *et al.* 2010, Park *et al.* 2013, Rottman *et al.* 2012), or fluorescence microscopy (Kiser *et al.* 2010, Otero-Gonzalez *et al.* 2015). However, ENP are generally difficult to quantify from imaging data. The new approach using the magnetic susceptibility for the quantification of Fe_3O_4-NP opens the door to a simple *in-situ* tracing of Fe_3O_4-NP without sample preparation. This offers the possibility to conduct laboratory tests to investigate the detailed distribution of Fe_3O_4-NP in the biofilm. To shed light on the biosorption of Fe_3O_4-NP in the batch experiments, a proper mass balance was established for t = 18 h by means of MSB. According to Equation 4-1, the initial Fe mass $m_{\text{Fe } t = 0\text{ h}}$ consisted of four fractions, see Table 4-2.

Table 4-2: Mass balance of the batch experiments for the biofilm size fractions of 100 - 250 µm, 250 - 500 µm and 500 - 800 µm (duplicates) using c_0(Fe) = 200 mg/L and c(TSS) = 2 g/L. By means of MSB, a detailed Fe mass balance is feasible according to Equation 4-1.

biofilm size / Fe mass	100 - 250 µm (mg Fe)		250 - 500 µm (mg Fe)		500 - 800 µm (mg Fe)	
$m_{\text{Fe } t = 0\text{ h}}$	6.39	6.39	5.77	5.77	6.20	6.20
$m_{\text{Fe sample } t = 18\text{ h}}$	4.03	4.07	3.29	3.34	3.74	3.79
$m_{\text{Fe supernatan } t = 18\text{ h}}$	1.70	1.71	1.13	1.15	1.46	1.50
$m_{\text{Fe biosorption } t = 18\text{ h}}$	0.14	0.14	0.11	0.11	0.15	0.15
$m_{\text{Fe losses } t = 18\text{ h}}$	0.52	0.47	1.24	1.17	0.86	0.77
losses (t = 18 h)	8.1 %	7.3 %	21.5 %	20.2 %	13.8 %	12.5 %

The fractions for Fe_3O_4-NP described as Fe mass located in the samples ($m_{\text{Fe sample } t = 18\text{ h}}$) and in the supernatant ($m_{\text{Fe supernatan } t = 18\text{ h}}$) were subtracted from the initial Fe mass. The losses ($m_{\text{Fe losses } t = 18\text{ h}}$) for all batches were relatively low; < 22 %, indicating a good mass balance closure which was reproducible (duplicates). The biosorption of Fe_3O_4-NP in the settled granular biofilm ($m_{\text{Fe biosorption } t = 18\text{ h}}$) was overall very low. Only 1.9 % of the initially added Fe, corresponding to 140 µg Fe was recovered in the settled granular biofilm of the size fraction of 250 - 500 µm. For 100 - 250 µm and 500-800 µm the values were slightly higher with 2.2 % and 2.4 %, respectively, but they were still lower than expected. Equation 4-2 defines the biosorption ($m_{\text{Fe biosorption } t = 18\text{ h}}$) to consist of Fe_3O_4-NP attached on the biofilm ($m_{\text{Fe granular biofilm } t = 18\text{ h}}$) and being loosely bound and located in the interspace within the granular biofilm ($m_{\text{Fe interspace } t = 18\text{ h}}$). In order to separate those two portions, the biofilm was rinsed to remove the loose Fe_3O_4-NP in the interspace. The results revealed that 11 - 18 µg Fe, corresponding to 9.3 - 13.6 % of the total biosorption

($m_{\text{Fe biosorption } t = 18\text{ h}}$), were still attached to the granular biofilm after rinsing. Consequently, the major part of the attached Fe_3O_4-NP was loosely bound or located in the interspace of the suspended granular biofilm. The presented results emphasize that there was no pronounced interaction between granular biofilm and the PVA coated Fe_3O_4-NP. The attachment of Fe_3O_4-NP can be described as reversible in this case. This might be due to steric repulsion and stabilization by the organic functionalization (PVA) of the used Fe_3O_4-NP, which were slightly negatively charged in the experimental environment. A possible electrostatic repulsion was created by the partly negatively charged granular biofilm. As other studies reported (Gu *et al.* 2014), the limited interaction could also be explained by the compact multilayer structure of the granular biofilm (de Kreuk *et al.* 2007), which could have hindered the biosorption of Fe_3O_4-NP. Summarizing, the Fe_3O_4-NP were only removed by 5 - 35 % and Fe_3O_4-NP partly attached to suspended particulate OM in the water phase. These results indicate that granular biofilm has a higher risk potential to contribute to the release of Fe_3O_4-NP from WWT systems compared to flocculent biofilm.

4.3.4 Parameters influencing the biosorption of Fe_3O_4-NP to granular biofilms

To improve the understanding about the processes driving the biosorption, experiments varying the initial Fe concentrations and TSS concentrations were conducted and presented in Figure 4-8. The results show that the granular biofilm size fraction had a low impact on the total biosorption of Fe_3O_4-NP (Figure 4-8, A)

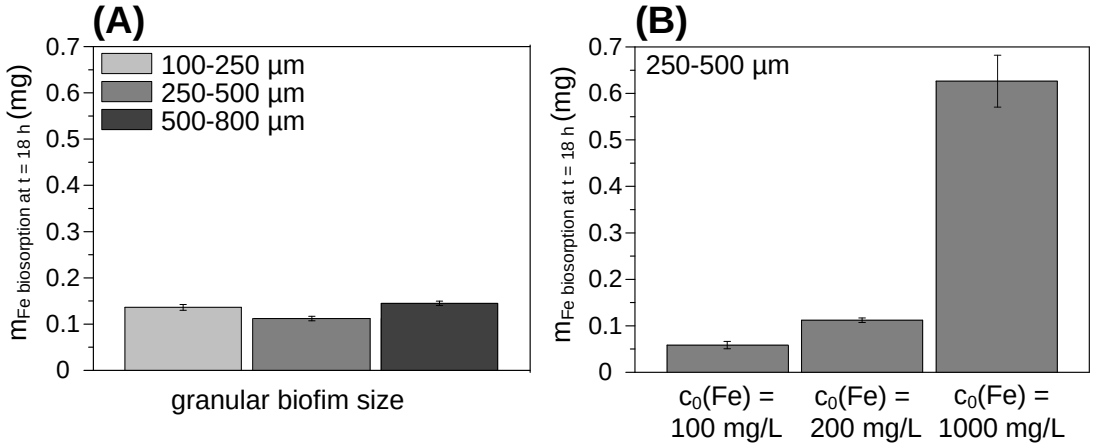

Figure 4-8: Parameters which influence the total biosorption of Fe_3O_4-NP in the granular biofilm: (A) batches with varying granular biofilm size fractions (c(TSS) = 2 g/L) and an initial concentration of Fe_3O_4-NP of c_0(Fe) = 200 mg/L, (B) batches with a granular size fraction of 250 - 500 µm (c(TSS) = 2 g/L) and c_0(Fe) of 100; 200 and 1000 mg/L.

For all size fractions the total biosorption ($m_{\text{Fe biosorption } t = 18\text{ h}}$ - not rinsed) differed only slightly between 0.11 mg Fe and 0.15 mg Fe. The maximum biosorption found was 1.9 µg Fe/mg TSS (biofilm size fraction of 500-800 µm, TSS = 2 g/L, exposure concentration 200 mg/L Fe).

This is contrary to the removal efficiency of Fe_3O_4-NP (see Figure 4-6), which wrongly suggests that there might be a difference in biosorption of Fe_3O_4-NP between the different granular size fractions. The size fraction of 250 - 500 µm has the highest OM release and highest removal, but the biosorption is as low as those for the other size fractions. Consequently, the Fe_3O_4-NP which were removed from the water phase did not necessarily end up sorbed to the granular biofilm. We assume that Fe_3O_4-NP were attached to particulate OM just above the settled granular biofilm in the water phase, as described above. Those Fe_3O_4-NP were covered neither by the measurement in the supernatant nor by the measurement of the granular biofilm. The particulate OM can serve as vehicle for Fe_3O_4-NP and can increase their mobility in the system. Figure 4-6, B presents variation of initial concentrations of Fe_3O_4-NP in the batch experiments with 250 - 500 µm sized granular biofilm. There was a positive linear correlation between c_0(Fe) and the biosorption. According to a model calculation, the granular biofilm surface can be loaded only to < 1 % with Fe_3O_4-NP assuming a monolayer of 200 nm sized Fe_3O_4-NP and spherical granular biofilm with an average diameter of 375 µm. This calculation led to the assumption that a small part of Fe_3O_4-NP interacted with the biofilm (still providing free adsorption sides), and was removed from the supernatant not only by electrostatic mechanisms. A more complete picture can be given by the influence of *c*(TSS) on the biosorption by Figure 4-9.

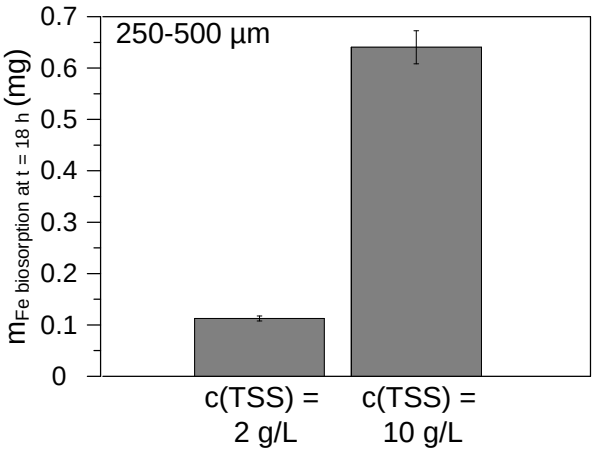

Figure 4-9: Biosorption in batches with a granular biofilm size fraction of 250 - 500 µm and c_0(Fe) of 100 mg/L (averaged data from batches in duplicates).

By increasing the TSS by a factor of 5, the total biosorption was enhanced by approx. factor 5 as well (positive correlation). However, the biosorption of 1.6 µg Fe/mg TSS of the batch experiment with *c*(TSS) = 10 g/L was comparable with the one of the batch employing *c*(TSS) = 2 g/L being 1.4 µg Fe/mg TSS. Those results give indications that physical co-sedimentation contributed to a higher extend to the removal of Fe_3O_4-NP from the supernatant than other interactions with the granular biofilm such as adsorption. To a certain extent, the presented results for Fe_3O_4-NP with a magnetite core can be transferred to other ENP

with similar particle surface properties based on the knowledge that the core material has a minor influence on the fate of ENP (Lowry *et al.* 2012). Further experiments should focus on the transferability of the presented results to other ENP and on the application of the magnetic susceptibility to investigate the behavior of different coated Fe_3O_4-NP in bioreactors for WWT.

4.4 Summary

- Magnetic susceptibility represents a valuable method for the investigation of the fate of Fe_3O_4-NP in real biofilm systems. The magnetic susceptibility provides a simple approach for the *in-situ* quantification of Fe_3O_4-NP in the water phase and in the biofilm matrix with a high precision (error < 2 %).

- The changes in the chemistry of the water matrix, especially OM concentrations, are an important factor to consider when investigating the removal efficiency of Fe_3O_4-NP from the water phase. The removal of Fe_3O_4-NP from the water phase was rather low (5 - 35 %) compared to other studies conducting batch experiments (removal up to 100 %), see Table 2-1. Fe_3O_4-NP were stabilized by dissolved and particulate OM in the water phase, which was released by the granular biofilms itself during the batch experiment.

- A detailed mass balance confirmed that the biosorption of Fe_3O_4-NP to the granular biofilms was low. Less than 2.4 % of the initially added Fe_3O_4-NP were associated with the biofilms after 18 h exposure time. The maximum biosorption found was 1.9 µg Fe/mg TSS (for an exposure concentration of 200 mg/L, exposure load 96 µg Fe/mg TSS).

- Fe_3O_4-NP seemed to be loosely bound to the granular biofilm and desorption occurred after rinsing. The hampered interaction of Fe_3O_4-NP with the biofilm was a result of the smooth surface and compact physical structure of the granular biofilms.

- Indications are given that physical co-sedimentation was a predominant removal process of Fe_3O_4-NP in granular biofilm systems under the assumption that granular biofilms still provide free sorption sides.

5 INFLUENCE OF THE PARTICLE SIZE AND SURFACE FUNCTIONALIZATION OF Fe_3O_4-NP ON INTERACTIONS WITH BIOFILMS*

*This chapter has been published in Acta Biomaterialia (2016), volume 31: 167-177 in collaboration with F. Ranzinger, S. Lackner, V. Grande, A. Baniodeh, A. Powell, H. Horn and G. Guthausen.

5.1 Introduction

The interactions and transport of ENP in the biofilm system are directly related to the biofilm's physical structure and composition. This is of major importance for technical, and environmental systems with respect to local diffusive and convective transport of compounds (solutes and particles) within biofilms (Flemming and Wingender 2010). Different imaging techniques, such as confocal laser scanning microscopy (CLSM), optical coherence tomography (OCT), and MRI, have significantly contributed to the understanding of biofilm structure and functionality (Herrling *et al.* 2015b, Manz *et al.* 2005, Morgenroth and Milferstedt 2009, Neu *et al.* 2010, Ramanan *et al.* 2013, Seymour *et al.* 2004b). Commonly applied techniques to investigate the mass transport of certain componds into biofilms, such as micro electrodes (limited to certain substances e.g. pH, O_2, NO_3^-) (De Beer *et al.* 1994b, Wasche *et al.* 2002) are invasive to the biofilm structure and consequently, the measured mass transfer in disturbed. CLSM techniques offer the possibility to investigate the biofilm structure and its components, however, specific staining agents are necessary and only selective visualization is feasible (Staudt *et al.* 2004, Wagner *et al.* 2009).

^{1}H-MRI is particularly suitable for non-destructive and *in-situ* biofilm investigations with spatial resolution of a few tens of µm (Morgenroth and Milferstedt 2009, Ramanan *et al.* 2013). In particular, various NMR parameters can be exploited to generate dedicated contrast in the images, which is not restricted simply to the ^{1}H spin density. Often, longitudinal (T_1) and transverse relaxation (T_2) times of ^{1}H nuclei are exploited for tailoring the contrast with the aim to characterize biofilm structure, which is crucial to better understand the interactions with ENP. Pure water exhibits relatively long T_2 relaxation times in the range of seconds, whereas T_2 of water inside biofilms is reduced to values about 100 ms

(Codd *et al.* 2011, Vogt *et al.* 2013). In this context, MRI represents the ideal tool to study the interactions between ENP and undisturbed biofilm systems. A perquisite for this is the paramagnetic properties of the target ENP, such as iron based ENP (Fe_3O_4-NP) serving as contrast agents. Those contrast agents (relaxation agents) determine the image contrast by paramagnetic relaxation enhancement (PRE) (Bertini *et al.* 2001, Callaghan 1991). PRE is caused by hyperfine relaxation caused by paramagnetic centers such as iron ions (Fe^{3+} and Fe^{2+}) (Ito *et al.* 2005). For more information on PRE, please see section 3.1.2 in this dissertation.

So far, it has been shown that MRI contrast agents enhance the contrast between bulk water and biofilm (Guthausen *et al.* 2015, Manz *et al.* 2003, Seymour *et al.* 2004a). Also the spatial distribution and adsorption of heavy metal ions in alginate was investigated (Nestle and Kimmich 1996). Of particular interest is the fate of heavy metals and nanomaterials in the environment, which can be estimated by the penetration of contrast agents into biofilms. The investigation of transport and immobilization in the biofilm by the concentration maps based on T_1 and T_2 values in homogenous and monoculture biofilms has been explored in 2D (Phoenix and Holmes 2008, Phoenix *et al.* 2008, Phoenix *et al.* 2009, Ramanan *et al.* 2013) and 3D (Bartacek *et al.* 2009). Most of the studies focus on heavy metal ions or molecular relaxation agents in combination with monoculture biofilms. However, the interactions between differently sized and functionalized Fe_3O_4-NP and multispecies biofilms have not been studied yet.

This chapter focuses on the interactions of differently sized and functionalized Fe_3O_4-NP with fluffy biofilms (similar to biofilm systems as used in chapter 6) in static batch experiments. Here, the transport of ENP in the biofilm system was mainly diffusion dominated. Insights into transport processes and biosorption were obtained by the visualization of Fe_3O_4-NP. The main goals of this chapter were to:

- Investigate the biofilm structure and its contrast generation in MRI images.
- Visualize the biosorption of different Fe_3O_4-NP within the biofilm matrix with respect to their particle size and surface functionalization.
- Assess the reversibility of the biosorption of Fe_3O_4-NP to the fluffy biofilm.

5.2 Materials and Methods

5.2.1 Biofilm cultivation

A laboratory scale moving bed biofilm reactor (MBBR) (volume V = 1 L) was operated over 90 days with a plastic carrier material, type K1 (AnoxKaldnes AB, Sweden). This K1 carrier (polyethylene, length: 9.2 mm, height: 7 mm) is cylindrical, has 4 combs, and a specific surface area of 500 m^2/m^3 (see Figure 5-1, A). The MBBR was continuously fed with acetate (1485 mg/L) as main substrate to grow heterogeneous, mixed culture biofilms on the carrier material (for the composition of the substrate, please see Table 6-1). The reactor was continuously aerated with pressurized air to guarantee mixing and sufficient oxygen supply. The cultivated K1 carriers were stored in tap water at 4°C before the experiment to minimize biological activity and no visible growth was observed during experiment (no substrate available).

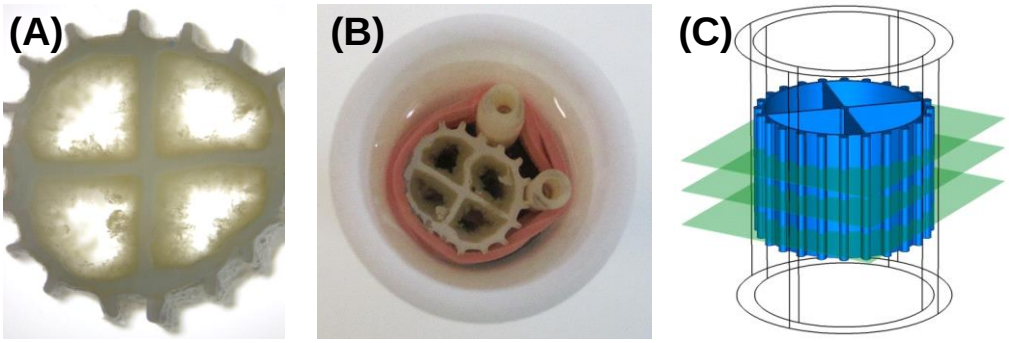

Figure 5-1: Heterotrophic biofilm on carrier material type K1 (AnoxKaldness. Sweden). (A) carrier material (9.2 mm length and 7 mm height) with biofilm. (B) the biofilm carrier is fixed with a rubber band in the MRI sample holder. (C) schematic of the experimental set-up: horizontal layers indicate the orientation of the measured axial slices (here: exemplary for 3 out of 8).

5.2.2 Contrast Agents: preparation and characterization

Fe_3O_4-NP serving as MRI contrast agents with different size, surface functionalization, and paramagnetic centers were applied (Table 5-1). In this case, suspensions of different super paramagnetic iron oxide nanoparticles (SPION) have been used: iron oxide composite particles (iron oxide core, dextran or starch shell) with different surface functionalizations and particle diameters (20 nm and 80 nm) (product name: nanomag®-D-spio and BNF-Dextran, micromod Partikeltechnologie GmbH, Rostock, Germany). Fe_3O_4-NP are known as predominantly T_2 contrast agents. The paramagnetic relaxation enhancement (PRE) was quantified from T_1-weighted and T_2-weighted images at 200 MHz for different contrast agent concentrations, leading relaxation rates as function of concentration. A linear regression finally revealed the relaxivities r_1 and r_2. r_1 and r_2 relaxivities of the different contrast agents in ultrapure water (Milli-Q, Merck Millipore, Billerica, Massachusetts, USA) were measured at concentrations of 0 - 137 mg/L Fe (BNF particles), 0 - 120 mg/L Fe (nanomag® particles) for r_1 and 0 - 13.7 mg/L Fe (BNF particles), 0 - 12

mg/L Fe (nanomag® particles) for r_2. For more specific information on the relaxivity of MRI contrast agents, please see section 3.2 and consult textbooks (Bertini *et al.* 2001).

The zeta potential of the Fe_3O_4-NP was measured using dynamic light scattering and laser DOPPLER anemometry, respectively ((n = 10), refractive index for iron oxide: 2.42; adsorption coefficient: 0.01, Zetasizer Nano ZS, Malvern Instruments, Worcestershire, United Kingdom).

Table 5-1: Properties of the applied MRI contrast agents (Fe_3O_4-NP). The relaxivity was measured at 200 MHz at concentrations of 0 - 137 mg/L Fe (BNF particles), 0 - 120 mg/L Fe (nanomag® particles) for r_1 and 0 - 13.7 mg/L Fe (BNF particles), 0 - 12 mg/L Fe (nanomag® particles) for r_2.

Fe_3O_4-NP	product name	diameter d_p (nm)	surface coating	zeta potential (mV)	applied concentration (mg/L)	*relaxivity* r_1 (L/(mg·s))	*relaxivity* r_2 (L/(mg·s))
BNFDex d80nm	BNF-Dextran	80	dextran	5 ± 5	25.6	0.0021	0.2046
BNFStarch d80nm	BNF-Dextran	80	starch	4 ± 4	25.6	0.0024	0.4585
Dexd20nm	nanomag®-D-spio	20	dextran	-1 ± 3	145.8	0.0027	0.2274
DexCOOH d20nm	nanomag®-D-spio	20	dextran-COOH	-22 ± 8	29.2	0.0178	1.4989

5.2.3 Experimental setup and procedure

Prior to the MRI experiments, K1 biofilm carriers were rinsed with tap water to remove residual substrate and easily detachable particulate organic and inorganic matter attached to the biofilm. In the following, the entire biofilm-carrier-system is defined as the unit of biofilm, carrier material and surrounding bulk water in the sample holder serving a batch vessel (see Figure 5-1, B). Prior to the measurement, a comb of the biofilm carrier was marked to identify the position of the K1 carrier later in the MRI images. A single biofilm carrier was then fixed with a rubber band in a MRI sample holder (serving as batch vessel) made of Teflon, PVC (polyvinyl chloride), and ceramics. The sample holder was completely filled with tap water ($V_{\text{sample holder}}$ = 2 mL) to maintain the biofilm's structure and provide space for the diffusive distribution of the Fe_3O_4-NP (contrast agents) in the bulk water. Biofilm-carrier-systems used for the experiments were first imaged without contrast agent. In long-term exposure experiments, biofilm carriers were stored at 4°C in 2 mL suspensions of different Fe_3O_4-NP (for applied concentrations, see Table 5-1)

for 14 days. The biofilm carriers were imaged by directly inserting them into the sample holder filled with the suspension of Fe_3O_4-NP used before for the exposure. To determine the reversibility of the attachment of Fe_3O_4-NP to the biofilm, the biofilm carriers were removed from the sample holder and rinsed with 100 mL of tap water before imaging the biofilm-carrier-systems again, now with tap water as surrounding medium.

5.2.4 MRI methods and sequence parameters

The experiments were performed on a 200 MHz tomograph (Bruker Avance 200 SWB, Bruker BioSpin GmbH, Rheinstetten, Germany). The superconducting magnet with a 150 mm vertical bore had a magnetic-flux density B_0 of 4.7 T. The Bruker gradient system micro2.5 was used with a ^{1}H-NMR bird-cage (25 mm inner diameter). Pulse sequences were applied as provided by Bruker within Paravision 4.0. The 90° radiofrequency block pulse was 45 µs at 0 dB. A sinc-pulse of 1 ms excited the magnetization (14 dB attenuation). For refocusing, a bandwidth matched sinc-pulse of 0.749 ms (5.5 dB attenuation) was applied. Relaxation measurements of each Fe_3O_4-NP were realized for PRE determination using a multi-slice multi-echo sequence (MSME) (Callaghan 1991 / 1993, Kimmich 1997). Data was processed within ParaVision® 4.0 (Bruker BioSpin GmbH, Karlsruhe, Germany) and via self-written scripts in Matlab® (version R2012a, Matlab Works Inc.; Natick, Massachusetts, USA). Slice selection was achieved by selective rf-pulses combined with a slice selection gradient. 2D images of the selected slices were obtained by the application of read and phase encoding. The K1 carriers were placed into the sample holder with the symmetry axis along $B_0||z$. The measured slices with a slice thickness of 0.8 mm (n = 8), exemplarily indicated by horizontal planes in Figure 5-1 C were orientated in the xy-plane and measured from bottom (1st slice) to top (8th slice). Each slice had a thickness of 0.8 mm; the interslice distance was chosen to 0.2 mm. For further information on the principles of MRI and the contrast generation in MRI images, please refer to textbooks (Callaghan 1991, Kimmich 1997) and chapter 3 of this dissertation.

To find optimal image contrast for the heterogeneous biofilms, a MRI parameter study was performed. The repetition time T_R and the echo time τ_E were varied respectively. A set of parameters was fixed to compare images with opposite contrast for different biofilms and the differently composed Fe_3O_4-NP, see Table 5-2. In addition to predominantly T_1- and T_2-weighted images, proton density (PD-weighted) images were measured as well. Because of the long T_R for T_2-weighted and proton density images, their resolution and number of averages were reduced compared to those used in T_1-weighted images, leading to a suitable overall measurement time while retaining an acceptable image quality. The MRI sequence parameters define the image contrast: Roughly speaking, in T_1-weighted images the biofilm appears bright and the bulk water dark on a conventional intensity based color scale. The opposite applies to T_2-weighted images, where the biofilm appears dark and the bulk water is bright. In PD images the bulk appears bright, and the

biofilm was barely recognizable (low contrast). For more detailed information, please refer to chapter 3.2.2 in this dissertation.

Table 5-2: MRI parameters for the acquisition of MRI images: three types of MRI measurements were performed to achieve different image contrast.

acquisition parameter	T_1-weighted image	T_2-weighted image	proton density (PD) image
T_R (ms)	800	10000	10000
τ_E (ms)	4.5	50	3.2
number of averages	20	4	4
matrix (pixel)	256 x 256	128 x 128	128 x 128
field of view (mm)	17 x 17, 19.5 x 19.5	17 x 17, 19.5 x 19.5	17 x 17, 19.5 x 19.5
spatial resolution (µm)	66 x 66, 76 x 76	133 x 133, 152 x 152	133 x 133, 152 x 152
slice thickness (mm)	0.8	0.8	0.8
interslice distance (mm)	0.2	0.2	0.2
number of slices	8	8	8
measurement time	1 h 8 min 16 s	1 h 25 min 20 s	1 h 25 min 20 s

5.2.5 Image analysis and visualization

The pre-processed MRI data was segmented within Matlab® version R2012a. The pixel intensity distribution is presented in form of histograms. The individual combs of the biofilm carriers were manually cropped from the T_1-, T_2-weighted and PD images (all 8 slices) to remove the influence of the surroundings outside the biofilm carrier. A script calculates the intensity distribution by pixel counting. Manually selected thresholds define segmentation classes. A classification of the pixel intensity is introduced correspondingly, for example, to biofilm (compact and fluffy parts), carrier material and bulk water in images of biofilm carriers without contrast agents. As this step includes a subjective interpretation and rating, the segmentation should be understood as indicator rather than as an unalterable quantification of the images. In case of the presence of contrast agents, classes for carrier material, contrast agent occurrence, and bulk water were defined. As several slices were measured in the MSME, the slice wise analysis allowed the profiling of those segmentation classes also as a function of carrier height.

5.3 Results and Discussion

5.3.1 Characterization of the pure biofilm

In a first step, the image contrast generated by the pure biofilm needs to be examined, to later understand the changes in the image contrast caused by Fe_3O_4-NP. Furthermore, information about the biofilm structure is needed for the comprehensive interpretation of the images, since the mass transfer is directly related to biofilm structure (Ramanan *et al.* 2013) and transport of ENP into the biofilm matrix.

Concerning the image contrast (Figure 5-2); the used fluffy biofilms usually appear bright in T_1- and dark in T_2-weighted images, respectively. The bulk water shows the opposite contrast: it appears dark in T_1- and bright in T_2-weighted images, respectively. The solid carrier material shows no signal (black) as also shown in chapter 3.2.2. For more detailed information please refer to chapter 3. In Figure 5-2, the investigated biofilms appear to be fluffy and heterogeneous and cover the inner phase of the carrier material. Surprisingly, it was observed that the contrast of the heterogeneous biofilm in the images has changed with time after the removal from the moving bed biofilm reactor (MBBR): Figure 5-2 shows T_1- and T_2-weighted images for three biofilm-carrier-systems measured at different times after their removal from the MBBR. The biofilm becomes brighter T_1-weighted images and darker in T_2-weighted images compared to the bulk water with increasing time after removal. This correlation is attributed to the different interactions and mobility of water molecules in the biofilm matrix, leading to different relaxation times. The biofilm shown in Figure 5-2, C (22 days after removal from MBBR) has most likely a more compact biofilm structure than the biofilms depicted in A and B, and therefore, exhibits smaller overall T_1 and T_2 relaxation times. The increased compactness of the biofilm may be the result of a change in structure, e.g., in the composition and physical structure of extracellular polymeric substances (EPS) which serve as protective matrix for the bacteria. Furthermore, it has to be considered that there was no substrate available during the storage of the biofilm (no biological activity assumed) and, therefore, the structure of the EPS might be compacted. The acquired PD images are not shown at this point because the biofilm cannot be distinguished from the bulk water as shown in chapter 3.2.2 and in Figure 5-5 A.

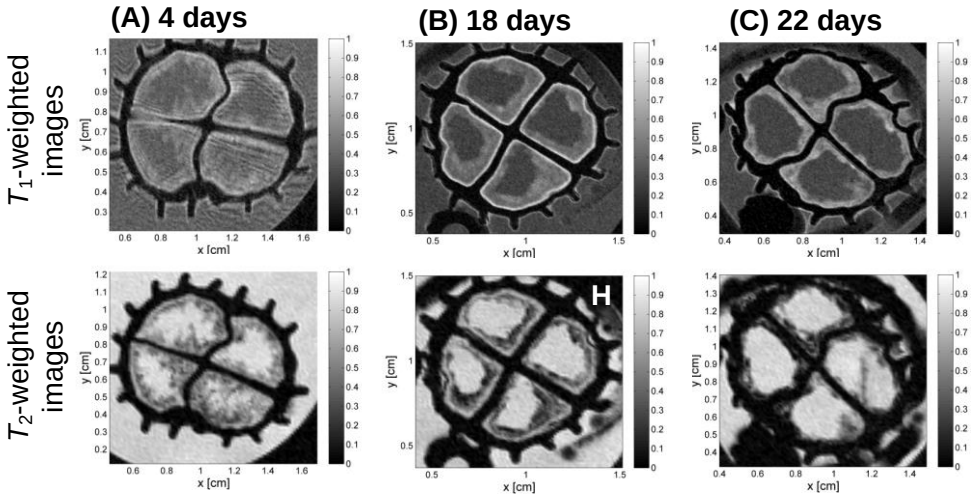

Figure 5-2: MRI T_1- and T_2-weighted images of different biofilm-carrier-systems without contrast agents (no Fe_3O_4-NP) measured at different times after removal from the MBBR (A - C). The image contrast differs with amount and heterogeneity of the biofilms even though they were cultivated in the same bioreactor. Blurred lines in T_1-weighted image (A) were due to motional artefacts. The histogram of the image indicated with "H" is shown in Figure 5-3.

Figure 5-3 presents the histogram of the T_2-weighted image of the biofilm-carrier-system after 18 days of removal from MBBR (indicated by "H"). The histogram of the pixel intensities (related to image brightness) shows two main peaks, one referring to the carrier material with lowest pixel intensities (up to a value of 26), and one for the bulk water with high pixel intensities (from value 183). Between these peaks the contribution of the biofilm can be found. Compact and fluffy biofilm parts (as seen in the images) were distinguished in the histogram by manually setting a threshold (at value 107).

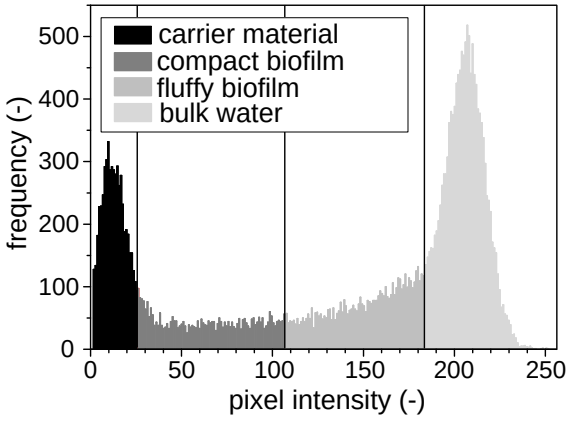

Figure 5-3: Histogram and segmentation classes (mean of all 8 slices, thresholds at 26, 107, 183) of the T_2-weighted image of the biofilm-carrier-system indicated with "H" (after 18 d of removal from MBBR, Figure 5-2). The pixel intensity is directly related to the brightness in the images.

The image quantification allows the monitoring of changes of these segmentation classes along the carrier height (Figure 5-4): As expected the portion representing the carrier material stays constant, whereas the biofilm and the bulk water portions vary strongly (dashed lines indicate the mean values). These deviations derived from the inclined carrier material which led to different local flow conditions in the MBBR and caused heterogeneous biofilm structures, compactness, and coverages. It is likely that different microorganisms within the biofilm additionally increased the heterogeneity of the biofilm. In summary, the biofilm structure and compactness determine the initial image contrast, which will later to be compared to the contrast generated by the added contrast agents (Fe_3O_4-NP).

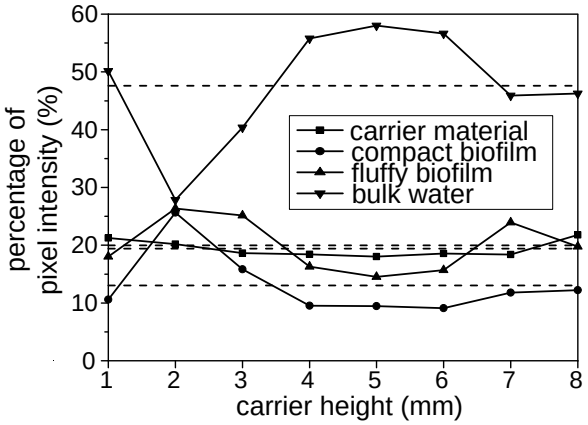

Figure 5-4: Variation of the segmentation classes (obtained by histogram in Figure 5-3) over the carrier height of a biofilm (in absence of Fe_3O_4-NP). Dashed lines indicate mean values of the single profiles of the segmentation classes.

5.3.2 Visualization of Fe_3O_4-NP in the biofilm matrix

The question about the behavior and mobility of pollutants, such as, ENP in the environment, and especially their interaction with biological systems is in the focus of recent scientific literature (Delay and Frimmel 2012, Lowry *et al.* 2010, Nowack and Bucheli 2007). One approach to address this question is the spatial observation of differently sized and functionalized ENP, here Fe_3O_4-NP, in real biofilms by means of MRI. In the following, the achieved results represent the first step towards the *non-invasive* and *in-situ* observation of ENP within the undisturbed biofilm matrix.

To emphasize the contrast generated by Fe_3O_4-NP in the biofilm system, an example for BNFDexd80nm (particle characterization given in Table 5-1) is demonstrated in the following. Especially in PD images the biosorption of Fe_3O_4-NP can easily be visualized due to drastic changes in the contrast, as the pure biofilm does not generate any contrast in the images (Figure 5-5 A). By subfigures B, it is emphasized that

BNFDexd80nm have a strong affinity to the biofilm's surface, which turns darkish by attachment of BNFDexd80nm. The BNFDexd80nm were homogenously suspended in the bulk water and approached the biofilm surface mainly by diffusion. BNFDexd80nm favorably attached onto the biofilm surface and outer layers possibly by an entrapment in EPS (Brar *et al.* 2010, Limbach *et al.* 2008). No full penetration can microscopically be observed by the images. The impact of the biosorption on the biological activity of the biofilms still remains unclear at this point and needs further investigations. Besides the attachment of Fe_3O_4-NP to the biofilm surface, these images demonstrate the suitability of Fe_3O_4-NP for the direct imaging of the biofilm surface. Usually, the attachment of different ENP to biofilms (or single microorganisms) and other kinds of biomass, such as activated sludge, is imaged by electron microscopy (Fabrega *et al.* 2009b, Schwegmann *et al.* 2010) or fluorescent microscopy (Kiser *et al.* 2010). However, those imaging techniques have certain disadvantages, such as invasiveness to the biofilms and limited field of view to the biomass (e.g. field of view in electron microscopy is on the nm to µm scale). For further information on biofilm imaging, please see section 3.2.2 and 3.2.3 in this dissertation.

Interestingly, a concentration gradient of BNFDexd80nm along the carrier height was observed in the exposure experiments as pictured by PD images at 2 mm and 7 mm carrier height, see Figure 5-5, B. This observation applies to all Fe_3O_4-NP used in chapter 5.

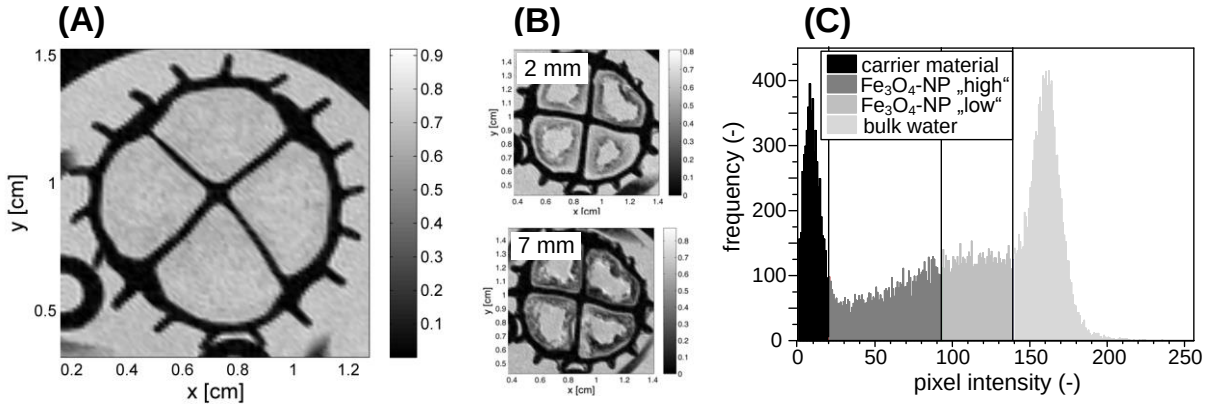

Figure 5-5: PD images of a pure biofilm (A) and a biofilm at a carrier height of 2 mm and 7 mm of the long-term experiment after injection of BNFDexd80nm (Fe_3O_4-NP). Areas containing a "high" or "low" amount of BNFDexd80nm were identified in the images (B) and distinguished in the histogram (C) (mean value of all 8 slices, thresholds: 20, 107, 183).

The histogram (C) emphasizes in accordance with the PD images (B) that there were regions in the biofilm containing different amounts ("high"/"low") of BNFDexd80nm. Therefore, manual thresholds were set at values of 20, 107 and 183 to distinguish these fractions. Compared to the histogram in Figure 5-3, the pixel intensities are remarkably shifted to lower values due to the darkish regions exhibited by the added BNFDexd80nm. Figure 5-6 depicts that BNFDexd80nm mainly sorbed to the upper biofilm carrier parts starting from 4 mm as demonstrated in the profiles of the fractions of "high" and "low" amounts of

BNFDexd80. This can be explained by the restricted diffusive transport of BNFDexd80nm into the biofilm matrix, as it was lying on the bottom of a batch vessel for 14 days of exposure under stagnating conditions. Fe_3O_4-NP have a low self-diffusion coefficient compared to smaller more diffusive water compounds as e.g. substrates (Peulen and Wilkinson 2011). Therefore, the distribution in the biofilm system might not be homogenous. The presently used spatial resolution of 66 µm allows the investigation of the structure of the biofilms and the biosorption of Fe_3O_4-NP, but cannot reveal the molecular interaction mechanisms. With the help of the images, not only indications for the fate of Fe_3O_4-NP, but also for the mass transport of potential substrates are given. From the mass transport point of view, tracing such contrast agents in biofilms can also be an approach to gain information about mass transfer of substrates, even though they are much smaller than the used Fe_3O_4-NP (e.g. Glucose has a molecular diameter of ~1 nm). However, the mass transfer depends on a variety of parameters, such as e.g. the biofilm structure, biological activity and the interaction processes. Further experimental work using different kinds of contrast agents should be done.

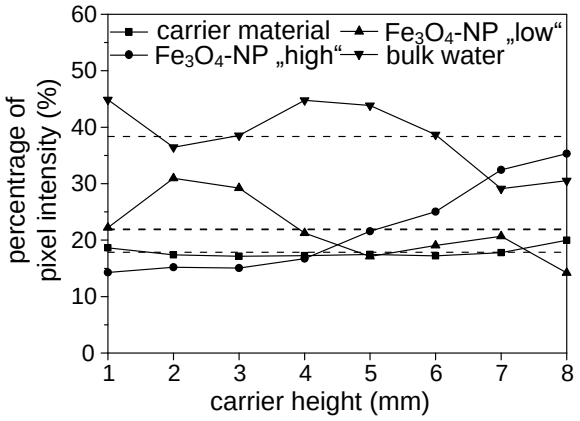

Figure 5-6: Segmentation classes along the carrier height in the biofilm-carrier-system. The segmentation class of water is larger in the middle of the carrier. The concentration of BNFDexd80nm (Fe_3O_4-NP) depends on the carrier height as indicated by the two fractions with "high" and "low" concentrations of Fe_3O_4-NP.

5.3.3 Biosorption and immobilization of Fe_3O_4-NP in the biofilm

Five kinds of Fe_3O_4-NP were investigated in long-term experiments to characterize their interactions and penetration into fluffy biofilms, as this is a recent research need with respect of the fate of ENP in the environment (Gottschalk *et al.* 2013b, Westerhoff *et al.* 2013). For all Fe_3O_4-NP the same iron concentration (to achieve a comparable contrast) was injected to achieve comparable image contrast (Table 5-1), consequently the particle number varied. The biofilms were stored for 14 days in a suspension of Fe_3O_4-NP, were then imaged and afterwards rinsed to assess the reversibility of the attachment. This

was done under stagnating conditions. Consequently, diffusion of Fe_3O_4-NP into the biofilm was the lone transport mechanism.

Figure 5-7 presents the results of the long-term exposure experiments for all used Fe_3O_4-NP. The majority of Fe_3O_4-NP sorbed onto the biofilm, as visible by negligible changes in signal intensity in the bulk water (outside the biofilm carrier) before and after rinsing (where the bulk water was replaced by fresh Fe_3O_4-NP free water). The image contrast of the PD images (for BNFStarchd80nm, BNFDexd80nm and Dexd20nm) and the T_1-weighted image (for DexCOOHd20nm) did not change after rinsing, which was also proved by histograms (data not shown). This highlights the high affinity of the investigated Fe_3O_4-NP to the biofilm surface.

Fe_3O_4-NP	in Fe_3O_4-NP suspension	after rinsing
BNFStarchd80nm	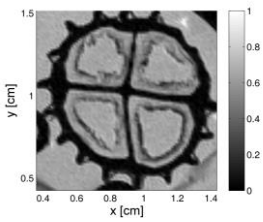	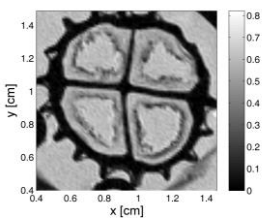
BNFDexd80nm	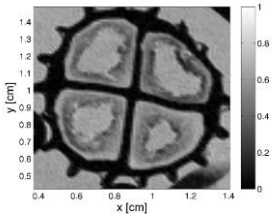	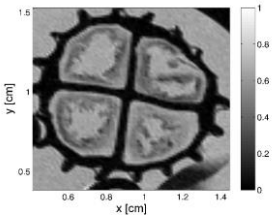
Dexd20nm	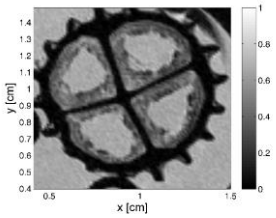	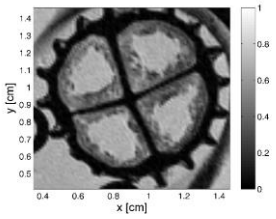
DexCOOHd20nm	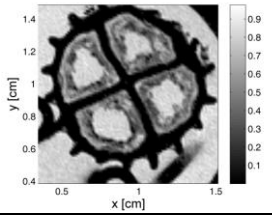	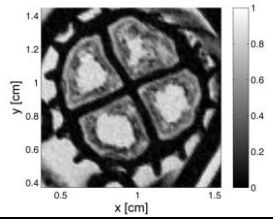

Figure 5-7: PD images (for BNFStarchd80nm, BNFDexd80nm and Dexd20nm) and T_1-weighted images (for DexCOOHd20nm) of long-term experiments for all Fe_3O_4-NP used: the biofilm carriers were stored in an aqueous contrast agent solution for 14 days (first column) and rinsed afterwards (second column) to investigate the reversibility of the sorption of Fe_3O_4-NP. Biofilms can slightly change their physical structure (detachment) after rinsing.

Generally, all types of Fe_3O_4-NP sorbed to the biofilm surface and outer biofilm layers, as mentioned earlier. However, the penetration depth of the used Fe_3O_4-NP differed: Dexd20nm showed a more homogeneous and deeper penetration into the biofilm than BNFDexd80nm as well as BNFStarch80nm. Therefore, differences in effective particle size of the Fe_3O_4-NP of the same chemical composition might lead to the limited penetration into the biofilm matrix. This effect has also been shown by other studies. The particle size and small self-diffusion coefficients lead to a lower mobility in the biofilm system (Peulen and Wilkinson 2011). In this context, the results underline that the type of Fe_3O_4-NP, as well as the structure of the biofilm, are relevant parameters to take into consideration when looking at the interactions of Fe_3O_4-NP with biofilms.

It seems that the particle surface functionalization had a minor impact on the interaction and penetration depth of Fe_3O_4-NP into the biofilm matrix: there are no visible differences in the penetration depth between BNFDexd80nm and BNFStarch80nm (particle diameter of 80 nm) as well as between Dexd20nm and DexCOOHd20nm (particle diameter of 20 nm). Moreover, the zeta potential was found to have no significant impact in this case, as DexCOOHd20nm exhibits a more negative zeta potential compared to Dexd20nm (see Table 5-1) and no visible differences in the penetration depth can be noted. Very surprisingly, the immobilization of all Fe_3O_4-NP was irreversible over the investigated exposure time (of 14 days), comparing the MRI images in Figure 5-7 before and after rinsing. By rinsing the fluffy biofilms, some changes in the biofilms' physical structure occurred, which were visible in PD and T_1-weighted images, however, the image contrast was maintained. To gain more quantitatively information, future work should focus on data processing and image analysis to determine e.g. biofilm thickness, penetration depths or concentration maps of Fe_3O_4-NP within the biofilm matrix. The presented results contribute to a better understanding of interactions and transport of differently composed ENP in heterogeneous biofilm systems. The images allow general assumptions about the biofilm heterogeneity, structure and transport properties, which are needed for the estimation of mass transport of substrates and particles. The irreversible biosorption of ENP might represent a key factor in their distribution and transport in the natural environment, where biofilms are ubiquitous (Costerton *et al.* 1995).

5.4 Summary

- MRI proved to be an elucidating approach to investigate the interaction of differently sized and functionalized Fe_3O_4-NP within heterotrophic biofilm systems. MRI acquisition parameters were optimized for T_1- and T_2-weighted as well as PD images exhibiting a good contrast for the biofilm and Fe_3O_4-NP.

- The structure of the biofilm, being partly fluffy and more compact, was distinguished by NMR relaxation parameters which determine the image contrast in T_1- and T_2-weighted and PD images. This gives indications about transport processes and permeability for dissolved and particulate water compounds into the biofilm matrix.

- The investigated Fe_3O_4-NP has a strong affinity to the biofilm surface and the attachment occurred quickly. Fe_3O_4-NP mainly sorbed to the biofilm surface and outer layers, but no full penetration could be observed.

- The influence of the particle size on the interactions with biofilms was visualized: smaller Fe_3O_4-NP (20 nm diameter) penetrated deeper into the biofilm matrix than bigger ones (80 nm diameter). Moreover, all Fe_3O_4-NP used were irreversibly immobilized within the biofilm matrix. This immobilization might be a key factor for the fate and eco-toxicity of Fe_3O_4-NP in natural and technical systems.

- Despite the particle size, the particle surface functionalization and the resulting zeta potential had a minor influence on the biosorption and penetration depth of Fe_3O_4-NP into the biofilm in this case.

6 INFLUENCE OF THE EXPOSURE TIME ON INTERACTIONS OF Fe_3O_4-NP WITH BIOFILMS*

*This chapter has been published in Science of the Total Environment (2016), volume 544: 722-729 in collaboration with S. Lackner, O. Tatti, G. Guthausen, M. Delay, M. Franzreb and H. Horn.

6.1 Introduction

When ENP enter into WWTP, their removal from the water phase is driven by the interactions with the biomass in the biological treatment step (Brar *et al.* 2010, Kiser *et al.* 2010), as stated in the introduction of this dissertation (chapter 1). Modelled and measured concentrations of ENP in WWTP effluents were summarized in Gottschalk et al. (2013) stating that their concentrations are in the range of a few ng/L up to 5 µg/L. However, the detailed characteristics for the removal and biosorption of ENP are still unclear. Recent studies show that the removal of different ENP is influenced by a complex framework of parameters, e.g. type of biomass (flocculent sludge or granular sludge (Gu *et al.* 2014)) and experimental setup, as well as type of bioreactor (e.g. batch experiments (Kaegi *et al.* 2013, Rottman *et al.* 2012), sequencing batch reactors (Wang *et al.* 2012, Yang *et al.* 2015), membrane bioreactors (Tan *et al.* 2015) or pilot WWTP (Hou *et al.* 2013, Kaegi *et al.* 2011)).

Apart from conventional activated sludge systems which are mostly used for removal experiments of ENP, moving bed biofilm reactors (MBBR) might be used where the biomass is organized in form of biofilms attached to plastic carrier materials (McQuarrie and Boltz 2011, Odegaard 2006, Odegaard *et al.* 1994, Wessman *et al.* 2004). In this context, it has recently been stated that biofilms in general serve as efficient "*sponges*" for ENP, but efforts to elucidate the fundamental mechanisms driving the interactions of ENP and biofilms are still at an early stage (Ikuma et al., 2015). Especially for newer WWT technologies employing biofilms, research is needed to evaluate if the mentioned "*sponge-like*" behavior for ENP can be transferred to different types of biofilms. Most studies investigate the interactions of ENP with monoculture biofilms for simplification (Jing *et al.* 2014, Wirth *et al.* 2012). However, only few studies use real multispecies natural or technical biofilms (Battin *et al.* 2009, Fabrega *et al.* 2011). To the authors´ knowledge, there is no study addressing the fate of ENP in heterotrophic biofilm systems in a

MBBR. The behavior of ENP entering MBBR is still uncertain and needs to be investigated to evaluate the risk potential for the release of ENP into the environment.

In this chapter, Fe_3O_4-NP with silica coating were employed to assess their pathways and interactions with biofilms in continuous flow systems, such as flow cells and MBBR. Fe_3O_4-NP were utilized as model nanoparticle allowing simple quantification due to their magnetism *via* the magnetic susceptibility as shown in chapter 4 (Herrling *et al.* 2015a). Single biofilm carriers were exposed to Fe_3O_4-NP at short contact times (5 min); complementary Fe_3O_4-NP were introduced into a MBBR and observed for 27 d to investigate the interactions at different time scales. The main goals of this chapter were to:

- Investigate the biosorption of Fe_3O_4-NP onto heterotrophic biofilms in flow cell experiments at short contact times.
- Investigate the removal and biosorption of Fe_3O_4-NP during MBBR operation over 27 days.
- Establish a detailed mass balance for Fe_3O_4-NP to get insights into the time and concentration dependent biosorption in the biofilm matrix.
- Visualize the local biosorption of Fe_3O_4-NP in the biofilm matrix by MRI.

6.2 Materials and Methods

6.2.1 MBBR operation and biofilm characterization

A laboratory scale MBBR (V_{MBBR} = 700 ml) filled with K1 polyethylene carrier material of 9.2 mm length and 7 mm height (AnoxKaldnes AB, Sweden) with a filling ratio of 25 % using 110 plastic carriers was operated for 6 months (Figure 6-1, C). The carrier material (Figure 6-1, A) had a specific surface area of 500 m^2/m^3. In this chapter, the same type of biofilm carrier has been used as in chapter 5 and 7. The reactor was fed with acetate (1485 mg/L) as sole substrate for the cultivation of heterotrophic biofilms, see Table 6-1.

Table 6-1: Substrate composition for the cultivation of heterotrophic biofilms in MBBR.

substrate compound	concentration (mg/L)
$CH_3COONa\ 3{\cdot}H_20$	1485
K_2HPO_4	52
NH_4CL	183
$FeSO_4\ 7{\cdot}H_2O$	8
$MgSO_4\ 7{\cdot}H_2O$	10
$CaCl_2\ 2{\cdot}H_2O$	12
trace elements	0.01 mL added to 1 L of substrate
trace element composition	**concentration (mg/L)**
H_3BO_3	100
$CoCl_2\ 6{\cdot}H_2O$	100
$CuSO_4\ 5{\cdot}H_2O$	30
$FeCl_3\ 4{\cdot}H_2O$	870
$MnCl_2\ 4{\cdot}H_2O$	135
$MoNa_2\ 2{\cdot}H_2O$	80
$ZnSO_4\ 7{\cdot}H_2O$	100
KI	30
$NiSO_4$	70

The hydraulic retention time (HTR) for biofilm cultivation (3 months) was set to 15 h, and then stepwise reduced to 5 h for the Fe_3O_4-NP exposure experiments. Thorough mixing and oxygen saturation was guaranteed by aeration with pressurized air. The pH value was set to 8 - 9 by dosing acidic water (0.014 % HCl solution). The electrical conductivity (~1500 µS/cm) remained stable over the whole experiment. During reactor operation, the soluble chemical oxygen demand (COD, filtered with 0.45 µm filter) using tests kits (LCK 414, HACH LANGE GmbH, Düsseldorf, Germany) was monitored. The amount of biomass attached to the carriers was quantified by determining the total suspended solid content (TSS) using 5 carriers. Biofilms were imaged using a stereomicroscope (Stereomicroscope SMT, Rathenow, Germany).

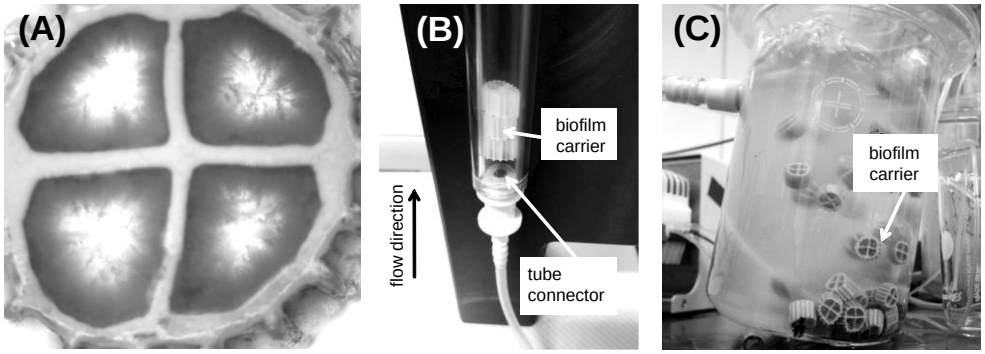

Figure 6-1: (A) heterotrophic biofilm cultivated on a plastic carrier with a diameter of 9 mm (K1, AnoxKaldnes, Sweden). (B) experimental setup of the flow cell where biofilm carriers are placed and exposed to different concentrations of Fe_3O_4-NP while the HRT was kept constant (flow direction from bottom to top indicated by the arrow). (C) MBBR with biofilm carriers mixed by aeration (no Fe_3O_4-NP addition).

6.2.2 Fe_3O_4-NP: preparation and characterization *via* MSB

Suspensions of Fe_3O_4-NP (MagPrep25 silica magnetic nanoparticles, c_{stock}(Fe) = 35 g/L, Merck KGaA, Darmstadt, Germany) with a primary particle size of 25 nm were used. Fe_3O_4-NP consist of a magnetite core (Fe_3O_4) and a silica shell which prevented oxidation or release of iron ions. The core and shell are expected to be stable over the whole experiment. Prior to the experiments, Fe_3O_4-NP suspensions were diluted in ultrapure water (Milli-Q, Merck Millipore, Billerica, Massachusetts, USA), mechanically mixed, treated in ultrasonic bath (1 h), and settled for 20 h. Then, the stable decanted supernatant was diluted to the desired concentration of Fe_3O_4-NP (c(Fe) = 200; 400; 1000 mg/L). The concentration of Fe_3O_4-NP in the liquid phase and adsorbed in the biofilms was determined based on their magnetic property using a magnetic susceptibility balance (MSB) for magnetic susceptibility measurement (χ) (Sherwood Scientific, Cambridge, England, detection limit of $\chi_{V\,min} = 0.13 \cdot 10^{-6}$ (SI units) provided by the manufacturer). To calculate the concentration of Fe_3O_4-NP (here, with silica coating), the magnetic susceptibility was correlated with their iron concentration (Figure 6-2) determined by inductively coupled plasma optical emission spectrometry (ICP-OES, Varian VistaPro, Agilent Technologies, Santa Clara, USA; calibration limit for Fe: 10 µg/L; after *aqua regia* digestion). ICP-OES has a high precision for Fe of 0.05 % (detection limit: 10 µg Fe). The MSB enables the *in-situ* detection of Fe_3O_4-NP and requires no sample preparation. To obtain reproducible results the χ_V (n = 3) was directly measured after sampling. For measurements of Fe_3O_4-NP in the liquid phase, 200 µL of the sample were pipetted into a MSB glass sample tube (sample height in the tube (I) = 2.5 cm)) and inserted into the MSB (measurement time = 60 s). For the quantification of the Fe_3O_4-NP sorbed to the biofilm (mixed phase system (solid-liquid)) the biofilm had to be removed from the carrier material prior to the measurement. Therefore, single carriers were stored for 12 h in NaOH solution (0.2 g/L; Sigma-Aldrich, Taufkirchen, Germany). The carrier

material was then removed from the vessel and the magnetic susceptibility of the suspended biofilm was quantified using the MSB as described above. For further information about the theory and precision of the magnetic susceptibility, please refer to the chapter 3.1 and to Herrling *et al.* 2015a.

For the basic characterization of Fe_3O_4-NP, the particle size (hydrodynamic diameter) was measured by dynamic light scattering and laser DOPPLER anemometry (Zetasizer Nano ZS, Malvern Instruments GmbH, Herrenberg, Germany). As refraction index (RI) and absorption (Abs.) for the measurement, values of iron oxide were used (RI = 2.420, Abs.= 0.010). Furthermore, zeta potential was measured with a combination of laser DOPPLER electrophoresis and phase analysis light scattering (M3-PALS), applying the Smoluchowski equation using the same device. The measurements were done in ultrapure water, because the matrix effects of the substrate disturbed the measurement. Fe_3O_4-NP have a particle size of 87 ± 20 nm (at *c*(Fe) = 4.4 mg/L), indicating that they tend to form agglomerates. The point of zero charge (*c* (Fe) = 4.4 mg/L) was between a pH value of 5-6. In the relevant pH range for MBBR operation (pH value 8 - 9) Fe_3O_4-NP had a zeta potential of ~ -20 mV.

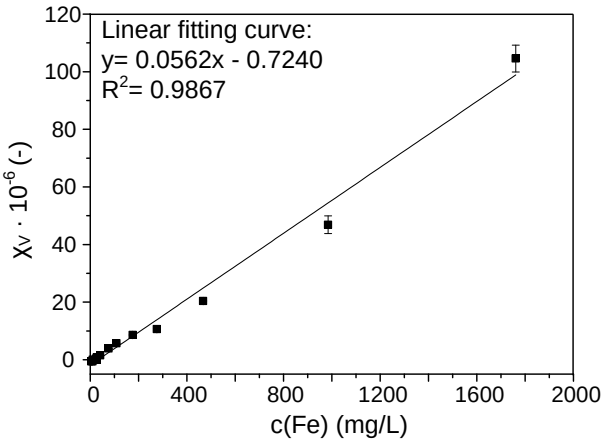

Figure 6-2: Correlation of the magnetic volume susceptibility (χ_v) (*y*-value) of Fe_3O_4-NP coated with silica determined *via* MSB with the Fe concentration (*c*(Fe), *x*-value) measured *via* ICP-OES. Standard deviations (n = 3) are too small to be seen in this graph. The working range was 4.4 mg/L Fe - 1762 mg/L Fe. Linear fit of a calibration curve resulted in a correlation coefficient of 0.9867, which reflects the good quality of the linear correlation.

6.2.3 Flow cell experiment and mass balance

Flow cell (FC) experiments were conducted using a transparent plastic tube serving as flow cell (V_{FC} was 7.8 mL to10.7 mL depending on the number of carriers inserted ($n_{\text{blank carrier}}$ and $n_{\text{biofilm carrier}}$). The FC was connected to a peristaltic pump (REGLO Digital MS-4/12, ISMATEC, Germany), see Figure 6-1, B. The desired number of carriers was placed into the flow cell directly at the bottom inlet. The inner crosses of the carriers were aligned to reduce flow resistance. Prior to the experiments, the FC system was pre-

conditioned with a Fe_3O_4-NP suspension (c(Fe) = 1000 mg/L) which was recirculated for 2 h. The experimental series were conducted in triplicates (except tube-1000 and 3bio-400 (duplicates)) varying the number of biofilm carriers and the injection concentration ($c_{\text{pulse injection}}$(Fe), $V_{\text{injection FC}}$ = 1 mL), see Table 6-2.

Table 6-2: Summary of flow cell (FC) experiments with varying numbers of blank ($n_{\text{blank carrier}}$) and of biofilm carriers ($n_{\text{blank carrier}}$). All experiments were conducted in triplicates (except tube-1000 and 3bio-400 (duplicates)). $c_{\text{pulse injection}}$(Fe) is the concentration of the pulse injection and $m_{\text{Fe enty FC}}$ corresponds to the total iron mass of the pulse. c_{FC} (Fe) is the calculated exposure concentration in the flow cell. $m_{\text{Fe loading FC}}$ represents calculated loading of Fe_3O_4-NP per carrier assuming that the Fe_3O_4-NP sorb homogenously to all biofilm carriers.

experiment	$n_{\text{blank carrier}}$	$n_{\text{biofilm carrier}}$	$c_{\text{pulse injection}}$(Fe)	$m_{\text{Fe enty FC}}$	c_{FC} (Fe)	$m_{\text{Fe loading FC}}$
	-	-	(mg/L)	(µg Fe)	(mg/L)	(µg Fe/carrier)
tube-1000	-	-	1000	946	88	-
10blank-1000	10	-	1000	946	105	-
10bio-1000	-	10	1000	946	123	95
3bio-1000	7	3	1000	1080	138	360
3bio-400	7	3	400	381	49	127
3bio-200	7	3	200	201	26	67

For the experiments, demineralized water was pumped through the system with flow velocities of 1.7 mm/s to 2.3 mm/s without recirculation (from bottom to top). The HRT was kept constant (~1.3 min). To start the experiment, Fe_3O_4-NP suspensions ($c_{\text{pulse injection}}$(Fe) = 200; 400; 1000 mg/L) were injected as a pulse into the system and the demineralized water was continuously pumped through as eluent. The concentration of Fe_3O_4-NP was measured manually at the outlet (n = 3) *via* MSB by collecting the total eluent in sampling vessels. At the end of each flow cell experiment (~ 5 min of perfusion until detection of pure water as eluent) a mass balance for Fe_3O_4-NP was established accordingly by

$$m_{\text{Fe entry FC}} = m_{\text{Fe outlet FC}} + m_{\text{Fe sediment FC}} + m_{\text{Fe biosorption FC}} + m_{\text{Fe losses FC.}} \quad \text{Equation 6-1}$$

The total mass of iron added to the flow cell system ($m_{\text{Fe entry FC}}$) equals the Fe_3O_4-NP passing the flow cell ($m_{\text{Fe outlet FC}}$), plus Fe_3O_4-NP which settled during the experiment ($m_{\text{Fe sediment FC}}$) on the tube connector (indicated in Figure 6-1, B), plus the portion of Fe_3O_4-NP which sorbed to the biofilm ($m_{\text{Fe biosorption FC}}$). Within this study, the term biosorption is used as the sum of all sorption processes of ENP (chemical and physical sorption processes and bio uptake) to the biofilms according to Kiser et al. (2010). The losses

described by $m_{\text{Fe losses FC}}$ are attributed to the experimental procedure or due to loosing Fe_3O_4-NP by opening-up the flow cell system.

6.2.4 MBBR experiment and mass balance

A continuous flow experiment was conducted in the MBBR to investigate the effect of the real water matrix on the fate and biosorption of Fe_3O_4-NP (Table 6-3).

Table 6-3: The MBBR (V_{MBBR} = 700 mL) was operated with 110 biofilm carriers ($n_{\text{biofilm carrier}}$) at a HRT of 5 h (inlet flow rate 130-160 mL/h). The iron mass added to the MBBR was $m_{\text{Fe entry MBBR}}$ = 100 mg Fe. c_{MBBR}(Fe) is the calculated exposure concentration and $m_{\text{Fe loading MBBR}}$ is the loading of Fe_3O_4-NP per carrier assuming that all Fe_3O_4-NP ($m_{\text{Fe entry MBBR}}$) homogenously sorb to all biofilm carriers.

experiment	$n_{\text{biofilm carrier}}$	$m_{\text{Fe entry MBBR}}$	c_{MBBR}(Fe)	$m_{\text{Fe loading MBBR}}$
	-	(mg Fe)	(mg/L)	(µg Fe/carrier)
MBBR	110	100	150	940

The original reactor liquid was sieved to remove particulate matter (13.6 µm precision sieve), and used as water matrix for the experiment. The exposure concentration (c_{MBBR}(Fe)) was in the same concentration range as the ones used for the flow cell experiments(c_{FC}(Fe)). The loading of Fe_3O_4-NP per carrier ($m_{\text{Fe loading MBBR}}$), assuming that all Fe_3O_4-NP homogenously sorb to all biofilm carriers in the MBBR without reaching saturation, was 3 - 14 times higher than for the flow cell experiments (compare Table 6-2 and Table 6-3). This was defined due to the increased complexity of the system (MBBR) where more uncertainties and losses for the recovery of Fe_3O_4-NP were expected. To start a MBBR experiment, the stock solution of Fe_3O_4-NP ($c_{\text{injection MBBR}}$(Fe) = 35 g/L) of $V_{\text{injection MBBR}}$ = 3 mL was directly added into the MBBR reactor vessel while aeration was on to ensure thorough mixing. During the MBBR experiment samples of 5 mL were taken for the magnetic susceptibility measurements (n = 3), positioning a conventional syringe 6 cm below the water surface of the MBBR after 5 min settling time (no aeration). Samples from the MBBR liquid were taken every 15 min starting from 80 min and from 4 h each hour, and starting from 20 h once per day for 27 days. The concentration of Fe_3O_4-NP was measured manually by the MSB (n = 3). Biofilm carriers were imaged using a stereomicroscope upfront the magnetic susceptibility measurement for the quantification of Fe_3O_4-NP sorbed to the biofilm matrix. To trace the distribution of the Fe_3O_4-NP a mass balance was established over the operation period of 0-5 h, 0-18 h and 0-24 h according to equation Equation 6-2. After 24 h of operation time, Fe_3O_4-NP were completely washed out of the MBBR.

$$m_{\text{Fe entry MBBR}} = m_{\text{Fe outlet MBBR}} + m_{\text{Fe liquid MBBR}} + m_{\text{Fe biosorption MBBR}} \cdot n_{\text{biofilm carrier}} + m_{\text{Fe sampling MBBR}} + m_{\text{Fe losses MBBR}}. \quad \text{Equation 6-2}$$

The initially added mass of Fe ($m_{\text{Fe entry MBBR}}$) can be described as the sum of mass of Fe leaving the MBBR *via* the outlet ($m_{\text{Fe outlet MBBR}}$), plus the Fe mass still being in the MBBR liquid ($m_{\text{Fe liquid MBBR}}$), plus Fe_3O_4-NP sorbed to the biofilm carriers ($m_{\text{Fe biosorption MBBR}}$), and plus the Fe mass which was removed from the MBBR by the sampling routine ($m_{\text{Fe sampling MBBR}}$). The Fe mass which could not be recovered during the experiment is summarized in the term $m_{\text{Fe losses MBBR}}$.

6.2.5 MRI methods

To support the quantitative results obtained by magnetic susceptibility, biofilm carriers were imaged using MRI for *non-invasive* visualization of the biosorption of Fe_3O_4-NP in the biofilm. Prior to MRI, the carriers where shaken overhead (30 rpm, for 12 h) in Fe_3O_4-NP solutions (V = 30 mL) of c(Fe) = 90 mg/L and c(Fe) = 350 mg/L, which are in the same exposure concentration range as the flow cell and MBBR experiments. Fe_3O_4-NP serve as contrast agents in MRI. The influence of Fe_3O_4-NP on the relaxation properties (T_1 relaxation) of ^{1}H nuclei (mainly in water molecules) in the biofilm was investigated using a high-field (200 MHz) MRI tomograph (Bruker Avance 200 SWB, Bruker BioSpin GmbH, Rheinstetten, Germany). The single carriers were placed into the tomograph with tap water as surrounding medium using an in-house sample holder. The superconducting magnet had a magnetic-flux density B_0 of 4.7 T and a 150 mm vertical bore. The Bruker gradient system micro2.5 was used with a ^{1}H-NMR bird-cage (25 mm inner diameter). The images were taken applying a modified multi-slice multi-echo sequence (MSME). For the acquisition parameter, please see Table 6-4. Please consult text books for the principles of MRI (Callaghan 1991, Kimmich 1997) and chapter 3 in this dissertation for further information on the imaging of biofilms and Fe_3O_4-NP.

Table 6-4: MRI acquisition parameters for the visualization (T_1-weighted images) of Fe_3O_4-NP within the biofilm matrix.

acquisition parameter	value
T_R (s)	0.8
τ_E (ms)	4.5
number of averages	20
matrix (pixel)	256 x 256
field of view (mm)	15 x 15
spatial resolution (µm)	58 x 58
slice thickness (mm)	0.8
interslice distance (mm)	0.2
number of slices	8
slice orientation	axial
measurement time	1 h 8 min 16 s

6.3 Results and Discussion

6.3.1 Flow cell experiments: biosorption of Fe_3O_4-NP at short contact times

To investigate the behavior of Fe_3O_4-NP in a simplified experimental environment, series of flow cell experiments were performed using demineralized water as eluent (Table 6-2). The investigated heterotrophic biofilms were light brownish and exhibited fluffy and open structures (see Figure 6-1). However, no detachment of biofilm layers was observed in the flow cell experiments, in which biofilms were exposed to Fe_3O_4-NP for a short time period. The applied concentrations of Fe_3O_4-NP were higher than the expected environmental concentrations for nanomaterials (Gottschalk *et al.* 2013b) to better identify the driving forces and their distribution. Figure 6-3, A presents the mass balance of the normalized Fe mass ($m_{Fe\ norm}$) for the flow cell experiments according to Equation 6-1 with a good mass balance closure of 4 - 30 %. The amount of biofilm in one single carrier was stable (86 ± 5 mg TSS/carrier (n = 5)), contributing to low variability of the data.

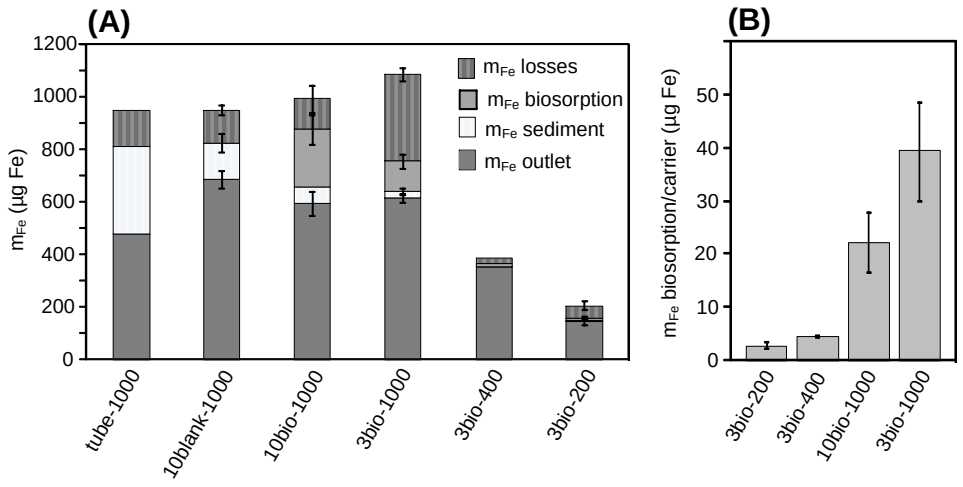

Figure 6-3: (A) Mass balance for m_{Fe} in the different flow cell (FC) experiments (see Table 6-2). The experiments were conducted in triplicates (except tube-1000 and 3bio-400 (duplicates)). Here, $m_{Fe\ outlet}$ defines the Fe_3O_4-NP passing the flow cell by the effluent, $m_{Fe\ sediment}$ are the settled Fe_3O_4-NP during the flow cell experiment and $m_{Fe\ biosorption}$ represents Fe_3O_4-NP sorbed on all biofilm carriers. The portion of $m_{Fe\ losses}$ (4 - 30 %) indicates that a reliable mass balance closure is achieved. (B) biosorption per carrier in experiments with 3 biofilm carriers and varying concentrations of Fe_3O_4-NP.

A positive effect of the blank carrier material on the stability of Fe_3O_4-NP is highlighted by the comparison of the empty tube (tube-1000) and assembled with 10 blank carriers (10blank-1000). The lower Fe_3O_4-NP retention in the flow cell filled with blank carrier compared to the one without carrier material, is shown by less sedimentation ($m_{Fe\ sediment}$) and more efficient transport of Fe_3O_4-NP through the flow cell to the outlet ($m_{Fe\ outlet}$). The better mixing kept Fe_3O_4-NP in suspension. Comparing 10blank-1000 and 10bio-1000 the stabilizing effect of the biofilm on Fe_3O_4-NP was evident from the increased portion of Fe_3O_4-NP in the outlet, and decreased portion of settled Fe_3O_4-NP. It is assumed that dissolved and particulate organic matter (OM) which was likely released from the biofilm matrix (i.e. EPS) stabilized the Fe_3O_4-NP in the flow cell. Results of chapter 4 (Figure 4-4) showed that biomass from a WWTP is able to release OM, which stabilized Fe_3O_4-NP in the bulk liquid. OM is known for its ability to coat the surface of ENP, leading to steric as well as electrostatic stabilization (Delay *et al.* 2011, Zhang *et al.* 2009).

It was observed that the portion for $m_{Fe\ outlet}$ was high (up to 65 % of input Fe_3O_4-NP) for all flow cell experiments, indicating that the transport of Fe_3O_4-NP was favored. The mass balance gives evidence on biosorption of Fe_3O_4-NP by biofilms ($m_{Fe\ biosorption}$). Possible mechanisms for the attachment might be electrostatic attraction due to the negatively charged biofilm and sorption (chemisorption and physical sorption), as well as entrapment of Fe_3O_4-NP in the open and heterogeneous structures of the biofilm (Brar *et al.* 2010, Ikuma *et al.* 2015). In the presented mass balance, $m_{Fe\ biosorp}$ represents the total biosorption in all biofilm carriers used in the experiments (either 3 or 10) being aware of the fact that there was no

preferential biosorption found on the biofilm carriers located at the entrance of the flow cell. By decreasing the number of biofilm carriers (from 10 to 3) providing lower biofilm surface areas (comparing 3bio-1000 and 10bio-1000), the total biosorption was reduced by 13 %.

Figure 6-3, B shows the correlation between the pulse injection concentration of Fe_3O_4-NP and the biosorption per carrier. There is a positive correlation for the experiments with 3 biofilm carriers. This positive correlation indicates that the biofilms might still provide free sorption sites and saturation has not yet been reached. Being aware of the limited data set, future experiments should focus on sorption rate experiments. However, the gained results demonstrate that the total biosorption per carrier was rather low compared to the input Fe_3O_4-NP (see Table 6-2). Loadings of Fe_3O_4-NP of <5 µg Fe per carrier (for $m_{Fe\ entry}$ FC = 201 and 381 µg Fe) and ~40 µg Fe per carrier (for $m_{Fe\ entry}$ FC = 1080 µg Fe) were found. This highlights that transport of Fe_3O_4-NP in the surrounding bulk liquid was more dominant than the sorption to the biofilm in this case. Therefore, at short contact times in a time scale of minutes, the interaction of Fe_3O_4-NP and the fluffy biofilms is only weakly defined. Due to the measured particle size of Fe_3O_4-NP (~85 nm), cellular penetration and uptake can most likely be excluded (Peulen and Wilkinson 2011). As the particle surface of ENP has a higher impact on the behavior in suspension than the core material (Lowry *et al.* 2012), the observed behavior in biofilm systems can be transferred to other ENP with comparable surface properties and sizes to a certain extent.

6.3.2 Fe_3O_4-NP in MBBR: fate and biosorption at long contact times

To investigate the behavior of Fe_3O_4-NP under more realistic conditions, a lab-scale MBBR experiment was performed (Table 6-3). Here, complex hydraulic conditions due to the movement of the carriers (Herrling *et al.* 2015b) and a close to real waste water chemistry are expected to influence the fate of the Fe_3O_4-NP. The detailed distribution of Fe_3O_4-NP during MBBR operation is shown by a mass balance after 5 h, 18 h, and 24 h after injection according to Equation 6-2. From 24 h no change in the concentration of Fe_3O_4-NP in the MBBR liquid as well as in the biosorption was detected. Therefore, the mass balance focuses on the time period of 0-24 h. The mass balance enables to appoint possible interactions between the Fe_3O_4-NP and the biofilms (Figure 6-4): surprisingly, Fe_3O_4-NP were mainly washed out of the MBBR instead of being retained in the biofilms by biosorption. Over an operation time of 0 - 24 h the portion of Fe_3O_4-NP released by the MBBR increased from 13 to 57 % ($m_{Fe\ outlet\ MBBR}$) emphasizing its low retention capacity. This result is supported by the decrease of Fe_3O_4-NP in the bulk liquid ($m_{Fe\ liquid}$) of the MBBR. Fe_3O_4-NP were efficiently removed to 98 % from the liquid after 24 h of operation time. However, the Fe_3O_4-NP did not necessarily end up sorbed in the biofilms as the portion for the biosorption ($m_{Fe\ biosorption}$) decreased from 17 % to 0.5 %. This is contrary to the findings in other WWT

systems were the majority of ENP is accumulated in the biomass, e.g. 90 % of Ag-NP in a pilot WWT plant (Kaegi *et al.* 2011) or 78 % of TiO-NP in a lab scale WWT system (Gartiser *et al.* 2014).

A negligible portion of the Fe_3O_4-NP was removed by sampling ($m_{Fe\ sampling\ MBBR}$) not affecting the mass balance result. We are aware of the losses ($m_{Fe\ losses}$) being higher than in the flow cell experiments due to the increased complexity of the system. However, after 24 h, 60% of Fe_3O_4-NP could be recovered and the temporal trend of the data gives insights into the fate of Fe_3O_4-NP in technical biofilm systems. This mass balance gap is slightly higher as the ones reported for other mass balances of ENP in bioreactors for WWT (e.g. 18 % balance gap) (Gartiser *et al.* 2014).

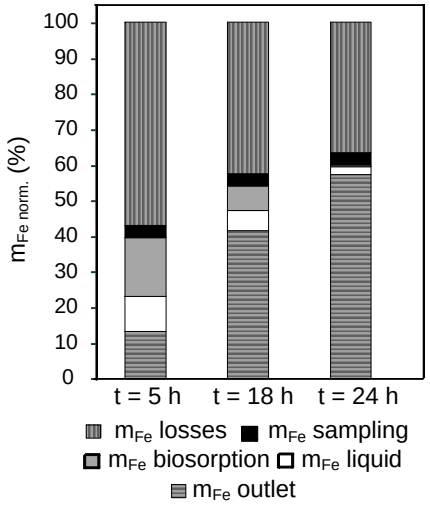

Figure 6-4: Mass balance of the MBBR experiment after 5 h, 18 h and 24 h: $m_{Fe\ outlet}$ represents the portion of Fe_3O_4-NP transported through the outlet of the MBBR, $m_{Fe\ liquid}$ is the portion of Fe_3O_4-NP suspended in the MBBR bulk liquid, $m_{Fe\ biosorp}$ corresponds to Fe_3O_4-NP attached to the biofilms, $m_{Fe\ sampling}$ represents the Fe_3O_4-NP which were removed by sampling and $m_{Fe\ losses}$ are the Fe_3O_4-NP which could not be recovered. Fe_3O_4-NP were determined using magnetic susceptibility (n = 3).

To find answers for the extensive washout of Fe_3O_4-NP, a closer look on the biofilms is needed. Figure 6-5 presents the temporal development of the concentration of Fe_3O_4-NP in the bulk liquid of the MBBR and the simultaneous biosorption of Fe_3O_4-NP per biofilm carrier. Contrary to other studies with sampling intervals of several days (Wang *et al.* 2012), in this work samples were taken more frequently. This reveals that Fe_3O_4-NP in the bulk liquid were removed very quickly from the wastewater within the first hour and completely removed within 24 h. After 1 min contact time, the biosorption in the MBBR reached ~40 µg Fe per carrier ($m_{Fe\ biosorption}$/carrier), similar to the results of the flow cell experiment 3bio-100 (Figure 6-3). This finding highlights that flow cell experiments can help to improve the understanding of the behavior of Fe_3O_4-NP in biofilm based reactors, such as MBBR systems, even though the general hydrodynamic conditions are different.

An unexpected trend occurred in the time resolved biosorption per carrier which could not be revealed by the mass balance. The biosorption first increased until 3 h after the injection of Fe_3O_4-NP and decreased again reaching a low and stable level from 24 h to 27 days ($m_{Fe\ biosorp}$<10 µg Fe per carrier). The maximum biosorption of Fe_3O_4-NP per carrier was 273 µg Fe corresponding to 3.2 µg Fe/mg TSS. Stereomicroscope pictures (Figure 6-6) visualize the biosorption of Fe_3O_4-NP on and in the biofilms (becoming dark brownish).

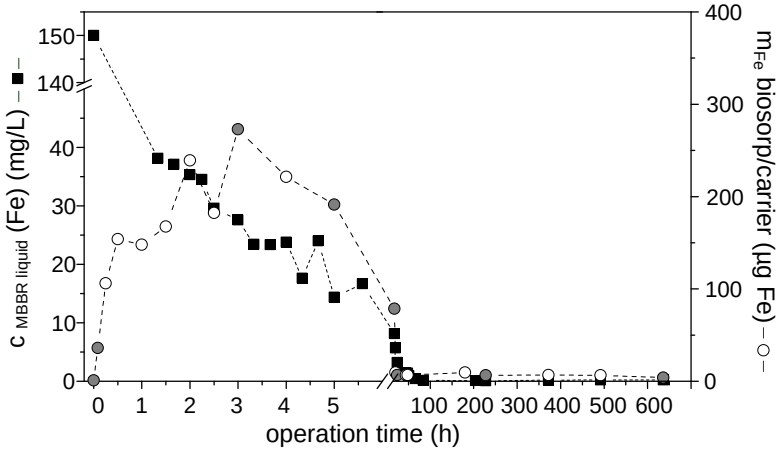

Figure 6-5: Temporal development of the concentration of Fe_3O_4-NP in the MBBR bulk liquid (squares) and simultaneous biosorption (dots) during MBBR operation up to 648 h (27 d). Please note that the *x*-axis (changing scale increments) and *y*-axis have breaks. Gray dots refer to stereoscopic images in Figure 6-6.

The decrease of the measured biosorption per carrier starting at 3 h (Figure 6-5) can be explained by the detachment of biofilm parts which were loaded with Fe_3O_4-NP. Such a loss of biofilm might occur due to mechanical as well as metabolic stress. The bacteria in the biofilm parts with Fe_3O_4-NP can locally be affected by lower substrate supply causing the biofilm structure to collapse and finally detach. Similar effects were found by Jing et al. (2014) where outer biofilm layers in monoculture biofilms were detached after exposure to CeO-NP as a self-protecting mechanism. However, as only outer biofilm layers might be affected, the biological activity stayed stable during the MBBR experiment as monitoring by the COD turnover; the effluent COD remained constant indicating no measurable toxic effect of Fe_3O_4-NP (see Appendix Figure A- 1). Other nanomaterials were also reported to have a low impact on COD removal in sequencing batch reactors (Wang *et al.* 2012) and laboratory-scale activated sludge system (Otero-Gonzalez *et al.* 2015). Compared to activated sludge systems (Kiser *et al.* 2010) and membrane bioreactors (Tan *et al.* 2015), where nanomaterials are mostly retained by sorption to the biomass (up to > 98 %); in the presented MBBR with heterotrophic biofilms a major portion of Fe_3O_4-NP was released *via* outlet. This is due to the stabilization of Fe_3O_4-NP by OM in the bulk liquid followed by washout and due to the detachment of biofilm parts loaded with Fe_3O_4-NP from the carriers and subsequent washout. The

extensive washout found is not in accordance with other studies employing continuous flow WWT systems as e.g. by Limbach et al. (2008) where only 6% of input CeO-NP exit a model WWTP. To avoid further transport into the environment, Fe_3O_4-NP retention in this case will depend on the efficiency of post settling or other solid retention systems such as filtration as suggested by other studies (Wang *et al.* 2012, Westerhoff *et al.* 2013).

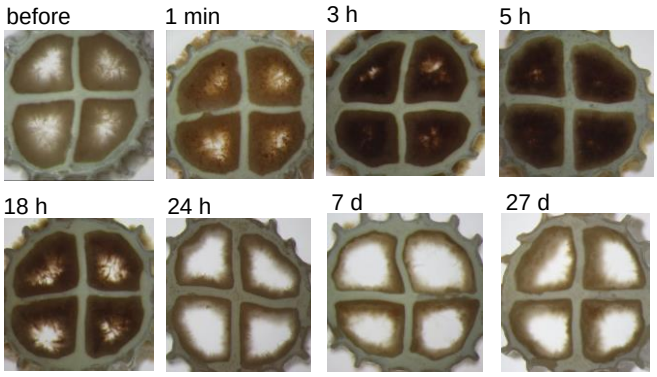

Figure 6-6: Stereomicroscopic images of the biofilm carrier before and after exposure to Fe_3O_4-NP. Images refer to gray data points (dots) in Figure 6-5.

In conclusion, the exposure time is of subordinated relevance for the interaction of Fe_3O_4-NP with the biofilm system as the biosorption occurred quickly (within minutes, see also chapter 5) and the transport of Fe_3O_4-NP in the bulk water was generally dominant. However, the time scale of observation has to be considered when looking at the long-term effects of the exposure (e.g. biofilm detachment, desorption etc.).

6.3.3 Visualization of biosorption

For the detailed visualization of the biosorption of Fe_3O_4-NP in the biofilm, MRI T_1-weighted images (spatial resolution of 66 µm) were taken after the exposure to different iron concentrations (c_0(Fe) = 0 mg/L, 90 mg/L and 350 mg/L), see Figure 6-7. MRI images give a deeper insight into the biosorption than stereoscopic images which only prove the visible attachment (Figure 6-7). In particular, the advantage of this imaging technique is the possibility of *non-invasive* and *in-situ* observations of wet biological samples compared to other destructive imaging methods such as electron microscopy, which is often applied to prove the sorption of nanomaterial to biomass from WWT (Fabrega *et al.* 2009b, Limbach *et al.* 2008, Rottman *et al.* 2012). In Figure 6-7, the blank biofilm appears bright, and the bulk water dark gray due to the differences in their spin relaxation time T_1 (left image). The carrier material appears completely black as no signal is exhibited. By the sorption of Fe_3O_4-NP to the biofilm (middle and right image), the biofilm becomes darker as the surrounding bulk water. Fe_3O_4-NP serve as contrast agents enabling their

visualization with MRI. Consequently, the image contrast is enhanced (see also other sections (3.2.3) and figures (Figure 5-5 and Figure 5-7) of this dissertation).

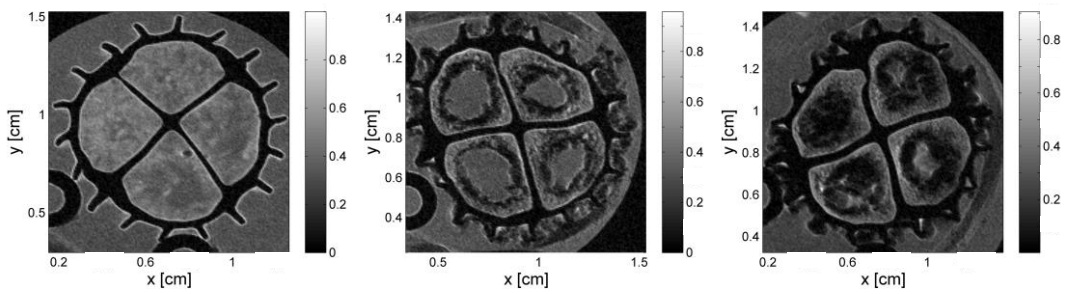

Figure 6-7: MRI images (T_1-weighted images) of a blank biofilm carrier and biofilm carriers exposed to Fe_3O_4-NP of 90 mg/L Fe and 350 mg/L Fe (left to right). The spatial resolution is 58 µm.

Fe_3O_4-NP mainly attached to the surface and outer layers of the biofilm as also demonstrated for other types of Fe_3O_4-NP in chapter 5. The biofilm was not fully penetrated by Fe_3O_4-NP as suggested by the stereoscopic images. It seems that Fe_3O_4-NP were captured by the fluffy structures of the biofilm surface and that there was a transport limitation over the biofilm depth. This finding supports the assumption that EPS might have collapsed after the exposure of Fe_3O_4-NP contributing to the detachment of Fe_3O_4-NP loaded biofilm parts from the carrier material. Using electron microscopy, it has recently been shown that SiO_2-NP and ZnO-NP can be structurally embedded and sorbed to the biofilm surface without necessarily disrupting the cell membranes (Hou *et al.* 2014, Sibag *et al.* 2015). This can explain why the removal of COD during the MBBR experiment remained constant and no measurable inhibition of the microbial activity took place (see Appendix Figure A- 1). Other studies also reported on changes in the biofilm structure after exposure to inorganic ENP: for example, increase and compression of EPS as a consequence of a protection mechanism (Hou *et al.* 2015) and reduction of the particle size of biomass (Yuan *et al.* 2015). In contrast, there are also studies available claiming no structural changes in the biofilm after exposure to ENP (Shang *et al.* 2015).

The exposure to 350 mg/L Fe in visibly led to a higher biosorption in comparison to 90 mg/L Fe as the dark regions in the biofilm representing Fe_3O_4-NP expanded. This is in accordance with the mass balance of the flow cell experiments (Figure 6-3), which proved that there was a positive correlation between the concentration of Fe_3O_4-NP and the biosorption. These results lead to a better understanding of the fate of Fe_3O_4-NP in MBBR systems with heterotrophic biofilms and give indications about the general distribution of ENP in WWT systems.

6.4 Summary

- The combination of the magnetic susceptibility and MRI is an excellent approach to elucidate the behavior of Fe_3O_4-NP in MBBR with biofilm carriers in detail. For example, it was seen that the removal of Fe_3O_4-NP by the biofilm used was remarkably lower than those of other studies found in literature.

- The influence of the exposure time on the biosorption of Fe_3O_4-NP to fluffy biofilms was of subordinated relevance for the initial biosorption. The interaction as defined weakly: Fe_3O_4-NP sorbed quickly onto the biofilms within minutes and the transport of Fe_3O_4-NP was more dominant than the biosorption in the initial phase.

- Transport of Fe_3O_4-NP was the predominant process in flow cells and MBBR, as both systems exhibit complex hydrodynamic conditions. This results in a low total biosorption. The maximum biosorption was 3.2 µg Fe/mg TSS in the MBBR (exposure concentration 150 mg/L Fe, exposure load 10.9 µg Fe/mg TSS) after the 3rd hour of exposure time.

- Besides the transport by fluid flow, the mobility of Fe_3O_4-NP in the bulk water was enhanced most likely by their stabilization with OM released by biofilm's EPS (compare chapter 4). Therefore, most Fe_3O_4-NP exited the flow cell (up to 85 %) and the MBBR (57 %) *via* the effluent, emphasizing the low retention capacity of the used biofilm systems.

- Fe_3O_4-NP sorbed mainly to the biofilm surface and no full penetration of the biofilm occurred. However, changes in the biofilm structure were observed after an exposure of 3 h in the MBBR: biofilm parts loaded with Fe_3O_4-NP detached and were washed out. However, the MBBR performance was maintained.

7 INLFUENCE OF THE BIOFILM STRUCTURE ON THE FLOW REGIME IN BIOFILM SYSTEMS*

*This chapter has been published in Biotechnology and Bioengineering (2015), volume 112(5): 1023-1032 in collaboration with G. Guthausen, M. Wagner, S. Lackner and H. Horn.

7.1 Introduction

Besides traditional activated sludge systems, where the biomass is organized in the form of sludge flocks, special attention has also been paid to biofilm systems (Lazarova and Manem 1995). Biofilms attached to carrier materials are e.g. applied in moving bed biofilm reactors (MBBR) (Rusten *et al.* 1995). Among others, great advantages of this technology are the high biomass contents and smaller footprints leading to a more cost-efficient treatment (McQuarrie and Boltz 2011). The MBBR process requires thorough mechanical or hydrodynamic mixing where carriers are continuously circulated to facilitate sufficient mass transport to the biofilm growing on the carriers (Odegaard *et al.* 1994, Rusten *et al.* 2006). In order to maintain an equally distributed thickness of the biofilm by shear forces, turbulence in the reactor is essential (Odegaard 2006). Boltz and Daigger (2010) reported some uncertainties in reactor-scale hydrodynamics concerning the biofilm-bulk phase interaction and reactor design. Thus, the effect of biofilm structure and morphology in correlation with mass transport processes in MBBR must be understood in more detail.

It is well known that the presence and structure of biofilms influence the local flow regime and transport of substrates into the biofilm (De Beer *et al.* 1994b, Flemming and Wingender 2010). The interaction between the biofilm matrix and the bulk phase is mainly driven by the interplay between diffusion and advection (Waesche *et al.* 2002). Apart from this predominant transport process (Stewart 2003), diffusion of substrates and nutrients plays a key role with respect to the metabolic activity, which usually is the limiting factor for the treatment of waste waters with biofilms (Boltz and Daigger 2010). The hydrodynamic conditions in the boundary layer at the biofilm surface directly influence reactor performance by driving the bulk-biofilm interaction. For the investigation of biofilm structure and functionality, imaging techniques have become indispensable. While traditional microscopy techniques

have limitations concerning *in-situ* observation and invasiveness (Neu *et al.* 2010), magnetic resonance imaging (MRI) has been proven to be an ideal tool for non-destructive and *in-situ* imaging of living biological samples with a strong potential in biofilm research. MRI is especially suitable for investigations of thick biofilms at the mm-scale or meso-scale (Morgenroth and Milferstedt 2009, Ramanan *et al.* 2013). Besides biofilm imaging, fluid flow around biofilm surfaces can be investigated qualitatively and quantitatively (Lewandowski *et al.* 1993) with the advantages of this method being without directional preference and able to record various parameters at the same time (Fukushima 1999). More recently, MRI methods were used to measure local flow velocities, shear stress and the impact of biofilm distribution, growth, and detachment on water flow fields surrounding biofilms growing in simple geometries such as tubes (Manz *et al.* 2003, 2005, Nott *et al.* 2005a, Seymour *et al.* 2004a, Wagner *et al.* 2010a). However, reality is often much more complex.

Not only addressing the mass transport of substrates, but also with respect to the transport of particles within the biofilm system, the hydrodynamics are important to consider. When engineered nanoparticles (ENP) enter WWT systems, such as MBBR, their direct interaction with the biofilms present will determine their fate in the MBBR, but also potential mass flows into the environment. A perquisite for the interaction and attachment of ENP to biofilms, is their transport towards the biofilm surface in water phase (Ikuma *et al.* 2015). The transport of ENP depends among others on the particle size, particle shape, particle charge and on the hydrodynamics of the surrounding bulk water. The transport of ENP can also be related to agglomeration as well as sedimentation processes (Christian *et al.* 2008, Elimelech *et al.* 1995) which might also impact the fate of ENP in the biofilm system. In the following the main focus lies in the influence of the biofilm structure on the local flow field, which can indirectly give indications for the transport of ENP within the biofilm system.

To get an insight into the driving forces for mass transport processes, flow velocity maps of blank and with biofilm cultivated carriers from WWT were measured. Due to the principle of relativity of motion, this approach can be used to investigate the interaction between biofilm and flow field. The main goals of this chapter were to:

- Investigate the real structure of the biofilm on carrier materials used in WWT.
- Quantify the flow regime in blank carrier materials compared to carriers with biofilms in three different orientations with respect to the main flow directions using 2D MRI flow velocity maps.
- Correlate the biofilm structure and the surrounding flow field.

7.2 Materials and Methods

7.2.1 Biofilm cultivation

A laboratory scale nitrifying MBBR (Volume V = 1 L) was operated for more than 100 days with K1 carrier material (AnoxKaldnes AB, Sweden) at a filling ratio of 40 %. The reactor with a hydraulic retention time of ~ 19 h was continuously fed with ammonium (500 mg-N L^{-1}). The reactor was aerated with pressured air to ensure mixing, as well as oxygen saturation. The reactor reached almost complete nitrification with residual nitrite concentrations of 5 - 10 mg/L NO_2^--N. The K1 carrier material is cylindrical with a cross inside and has a specific surface area of 500 m^2/m^3. The same biofilm systems are used in chapter 5 and 6, see Figure 6-1, A. For the MRI flow experiments, a single K1 carrier (9.2 mm length, 7 mm height) was taken and rinsed with tap water to remove remaining substrate and particulate matter prior to insertion into the MRI. Nitrifying biofilms were chosen for this experiment due to their stable structure.

7.2.2 Experimental setup and procedure

Blank K1 carriers and carriers with biofilm were separately placed into a silicon tube (inner diameter: 10 mm, length: 40 cm) at laminar flow conditions. The tube was placed into the bird cage (diameter : 25 mm) of the tomograph described below. The tube was connected to a peristaltic pump (REGLO Digital MS-4/12, ISMATEC, Germany) and tap water was pumped through from bottom to top without recirculation. For each of the selected scenarios (A - C) a new K1 with biofilm was used. Each carrier was placed in the experimental setup in three different orientations referring to the following scenarios depicted in Figure 7-1: A. vertically for axial forced flow, B. in an angle of 20° to the *z*-axis and C. 90° rotated to the *x*-axis to achieve transverse flow through the carrier. The green layer (in *xz* direction for A and B, *xy* for C) and red layer (*yz* direction for A and B) indicate the defined slices of the MRI measurements. The experiment was conducted at three volumetric flow rates of 1, 2 and 3 ml/min, corresponding to mean flow velocities in axial direction of 0.21, 0.42 and 0.64 mm/s for each scenario A - C.

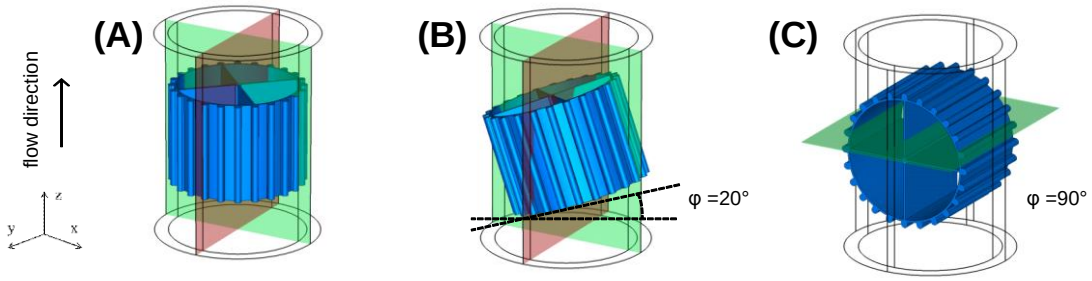

Figure 7-1: Scenarios (A – C): The biofilm carriers are oriented (A) vertically to the forced flow along *z* (sagittal images), (B) in an angle of 20° to the *z*-axis (sagittal images) and (C) 90° rotated to the *x*-axis to force transverse flow through the carrier (axial images). The measured slices are indicated as green (*xz* for (A) and (B), *xy* for (C)) and red (*yz* for (A) and (B)) layer.

7.2.3 MRI methods

The experiments were performed on a 200 MHz MRI tomograph (Bruker Avance 200 SWB, Bruker BioSpin GmbH, Rheinstetten, Germany). The superconducting magnet had a magnetic-flux density B_0 of 4.7 T and a 150 mm vertical bore. The Bruker gradient system micro2.5 was used with a ^{1}H-NMR bird-cage (25 mm inner diameter). Nuclear magnetic resonance (NMR) pulse sequences were used as provided by Bruker within Paravision 4.0. The 90° radiofrequency block pulse was 45 µs at 0 dB. The shaped pulses, used in the imaging sequences, were sinc-pulses of 1 ms for excitation (14 dB attenuation). For refocusing, a bandwidth matched sinc-pulse of 0.749 ms (5.5 dB attenuation) was applied. The 2D, slightly T_2 weighted proton density distribution and the displacements for flow velocity were measured by application of a multi-slice multi-echo sequence (MSME). Phase contrast imaging, flow encoding sequence (FLOW-PC) was also used. For MRI parameters please see Table 7-1.

Table 7-1: Acquisition parameters of MRI experiments to determine the flow in biofilm carriers.

acquisition parameter	method	
	MSME	FLOW-PC
T_R (ms)	1000	2000
τ_E (ms)	3.229	13.440
rare factor	-	1
number of averages	16	8
matrix (pixel)	128 x 128	128 x 128
field of view (mm)	14 x 14, 15 x 15, 17.5 x 15.7	14 x 14
spatial resolution (µm)	103 x 103, 117 x 117, 137 x 137	103 x 103
slice thickness (mm)	0.5	1
inter slice distance (mm)	1	-
slice orientation	axial, sagittal, coronal	axial, sagittal
flow encoding direction	-	*z*
measurement time	34 min 8 s	1 h 8 min

Multi-slice, multi-echo imaging (MSME)

The MSME sequence is one of the most common sequences in MRI (Callaghan 1991). A slice selection is realized by selective rf-pulses combined with a slice selection gradient, which is applicable in every spatial direction. 2D images of the selected slice were obtained by read and phase encoding. The sequence can also be used for time-of-flight experiments: In the case of the flow direction along $z||B_0$, i.e. the axis of the magnetic field, the slice selection gradient is chosen also along *z*, resulting in an at least partial saturation of an axial slice. Later in the experiment, the detected slice is chosen to be either sagittal or coronal. Due to the previously excited axial slice, a saturation stripe will be observed in the detected slice, which reflects a possible shift of the volume elements according to the local flow velocities and the time between the measurements of the two slices. Concluding, flow will deform and displace the stripes. For laminar flow a parabolic shape can be observed. In case of multiple excited slices, the saturation stripes are aligned parallel without flow. The deformation and displacement of the saturation stripes is proportional to the local flow velocity in each pixel and the time passed between excitation and detection of the slices. Their intensity depends on the delay between the excitation of the axial slices and the detection of the sagittal slice (Callaghan 1991, Kimmich 1997). In this study the slices were measured

successively from top to bottom, where the first measured slice appears in the lightest gray value and the last is the darkest.

Flow phase contrast imaging (FLOW-PC)

Velocities can also be measured via phase contrast flow imaging (Callaghan 1991, Callaghan and Xia 1991, Kimmich 1997). Phase contrast flow imaging relies on the fact that the signal phase is sensitive to velocity of magnetization elements. Therefore, comparing images with and without a flow encoding gradient reveals a flow velocity image. In this study the flow velocity was measured in *z*-direction. FLOW-PC images directly provide flow velocity maps of axial flows. This method is commonly used for the investigation of flow fields around biofilms (Manz *et al.* 2003, Wagner *et al.* 2010a). The application of both flow measurement techniques (MSME and FLOW-PC) provides distinct information about the system: as the visualization of biofilms morphology and flow local velocity distributions as well as flow velocity maps.

7.2.4 Digital image analysis and visualization

The Fourier-transformed and pre-processed MRI data was analyzed with Matlab® version R2012a (Matlab Works Inc.; Natick, Massachusetts, US) for background suppression and flow velocity image visualization. Mean and maximum flow velocities were calculated for the defined regions of interest. These regions were set in between the carrier material including the biofilm for each section excluding regions outside of the carrier. For biomass quantification and further image processing, ImageJ (Rasband, W.S., ImageJ, U. S. National Institutes of Health, Bethesda, Maryland, USA, http://imagej.nih.gov/ij/, 1997-2014.) was used. Manual thresholding was applied to transform the MSME images into binary images. Out of binary data the biomass structural parameters of each section were calculated by pixel counting out of three images.

7.3 Results and Discussion

7.3.1 Flow regimes in blank carriers: effect of the geometrical orientations

In the experiments, the biofilm carriers were fixed in three different geometrical positions into a tube (Figure 7-1) reflecting possible orientations of carriers moving inside a MBBR more or less freely, depending on filling degree and mixing intensity. The impact of carrier orientation relative to the surrounding fluid is still uncertain (McQuarrie and Boltz 2011), but crucial for better understanding of

mass transport processes. The set of MRI images shown in Figure 7-2 represents the different flow field scenarios of a blank K1 carrier. In Figure 7-2, the upper row presents the MSME images whereas the bottom row shows the FLOW-PC flow velocity maps of the scenarios A - C. It is important to stress that scenario C provides the *xy* plane compared to A and B where the *xz* plane is shown (compare Figure 7-1). In Figure 7-2 MSME and FLOW-PC measurements provide distinct information about the system.

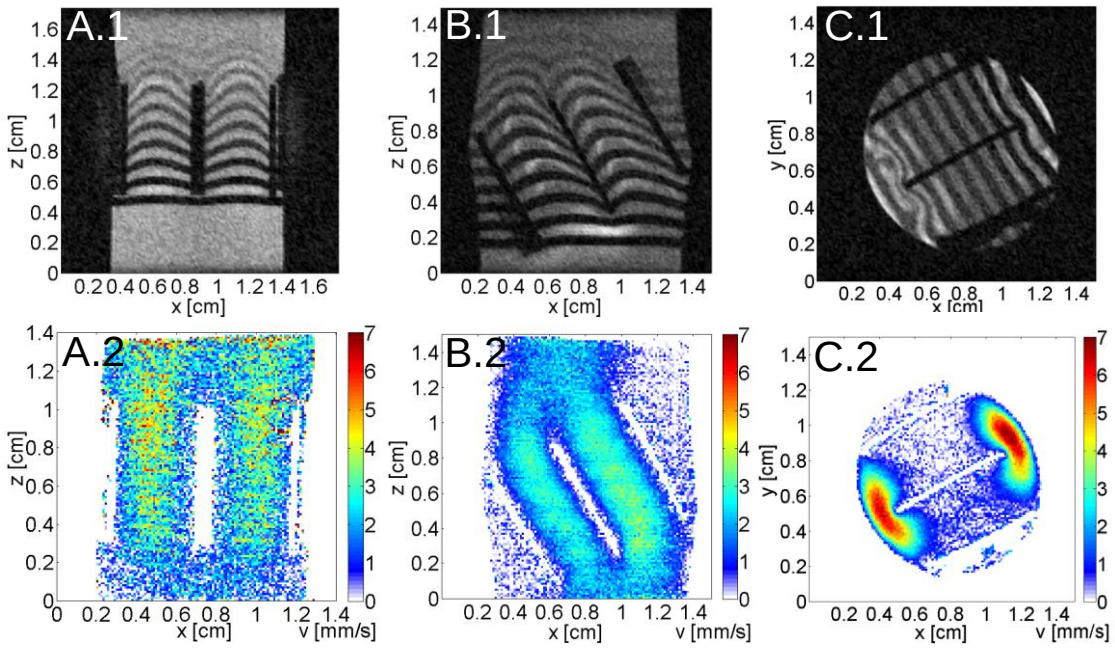

Figure 7-2: Scenarios (A - C) of the blank carrier measured at the green layer plane (see Figure 7-1). The overall flow is in *z*-direction with a flow velocity of 0.64 mm/s. In the upper row (A.1, B.1, C.1) MSME images and in the bottom row (A.2, B.2, C.2) FLOW-PC images are illustrated. The color bar encodes the flow velocity in mm/s in FLOW-PC images.

In the MSME images (A.1, B.1 and C.1), a good contrast is achieved between the blank carrier and the surrounding water (grey scale encoding) mainly due to the different transverse relaxation times T_2 of these two materials. The dark horizontal lines inside the carrier are the mentioned saturation stripes. During preparation the initial slice thickness of the MSME measurements was defined to be equal 0.5 mm. At the time of detection, some of the stripes expanded, the observed slice thickness correlates with the distribution of the local flow velocities at a specific location. In A.1 and B.1 the expected behavior for a laminar flow of a Newtonian fluid through a conduit according to the Hagen-Poiseuille law is observed. A parabolic flow velocity distribution is expected which is clearly visible in image A.1. In the case of C.1 the fluid inside the carrier is stagnant. Due to the different upstream flow angles, the profiles in B.1 are distorted and obviously illustrate the change in the direction of the flow field due to the 20° angle of the carrier with respect to the *z*-axis. Light grey pixels in B.1 in-between the saturation stripes can be understood as in-flow artifacts. While images A.1, B.1 and C.1 give an intuitive insight into the flow

fields, the FLOW-PC (A.2, B.2 and C.2) images show the flow velocity along the *z*-direction. Flow velocity profiles taken at the same position from both methods coincide well within the experimental precision. For further evaluation of local mean ($\bar{v}$) and maximum (v_{max}) flow velocities shown in Table 7-2, FLOW-PC data of A.2, B.2 and C.2 were used. The values refer to the two imaged sections of the carrier.

Table 7-2: Mean ($\bar{v}$) and maximum (v_{max}) flow velocities for the blank carriers (Figure 7-2) and the carriers with biofilm (Figure 7-3) of the applied flow velocities in the tube of 0.21 mm/s and 0.42 mm/s and 0.64 mm/s (corresponding to the volumetric flow rates of 1, 2, 3 ml/min). The values were extracted from the FLOW-PC velocity maps of regions of interest between the carrier materials for the two imaged sections. Data was pre-processed setting a threshold for noise removal.

	volumetric flow rates (ml/min)	A.2 blank	A.4 biofilm	B.2 blank	B.4 biofilm	C.2 blank	C.4 biofilm
$\bar{v}$	1	0.67	1.33	0.76	0.88	0.74	0.71
(mm/s)	2	1.24	2.71	1.39	1.57	1.30	1.32
	3	2.40	4.30	2.09	2.16	1.66	1.76
v_{max}	1	1.67	4.32	1.69	4.45	2.64	2.58
(mm/s)	2	3.45	8.52	2.91	7.45	5.06	4.98
	3	5.20	14.02	4.98	9.41	6.79	6.95

By the comparison of scenario A and B, $\bar{v}$ in the blank carrier increases by around 10 % due to hydrodynamic pressure and reduction of the diameter. Scenario C was chosen as a model to analyze the transverse flow component of the surrounding local flow field when the carrier is oriented in an angle of 90° to the flow direction. The fluid passes mainly through small regions at the sides of the carrier without being forced to flow through the carrier itself (C.1, C.2). Due to channeling in the side regions in scenario C; v_{max} (3 ml/min) of the blank carrier (6.79 mm/s) is higher than in scenarios A (5.20 mm/s) and B (4.98 mm/s), respectively. Nevertheless, the advective transport inside the carrier is limited. The regions of the highest flow velocities expand approximately 1 mm into the inner cavities of the carrier with a total height of 7.2 mm. This leads to restricted fluid exchange and to regions where very low fluid flow and thus stagnation occurs. As expected the mean flow velocity in the carrier increases corresponding to the volumetric flow rate (Table 7-2, A.2, B.2 and C.2). This has also been theoretically described in current literature by McQuarrie and Boltz (2011): the advection of water through the rotating carrier depends on the direction of flow and relative angle of the carrier to the main flow direction. Here, the measured data highlight that this impact emphasizes an engineering challenge of carrier design.

7.3.2 Flow regime in carriers with biofilm

For effective waste water treatment, substrate transport should be possible towards the complete biofilm surface inside the carrier (Christensson and Welander 2004, Rusten *et al.* 1995). Thus, the biofilm morphology is an essential parameter. For carriers with biofilm, a detailed description of the biofilm morphology is required to understand the flow fields and *vice versa*. The local flow is modified by the biofilm structure creating narrow pathways and a reduction of the inner carrier diameter. These factors overlap with the effect of geometrical changes described in the previous paragraph. In Figure 7-3, MSME images (A.3, B.3 and C.3) show the carriers with biofilm.

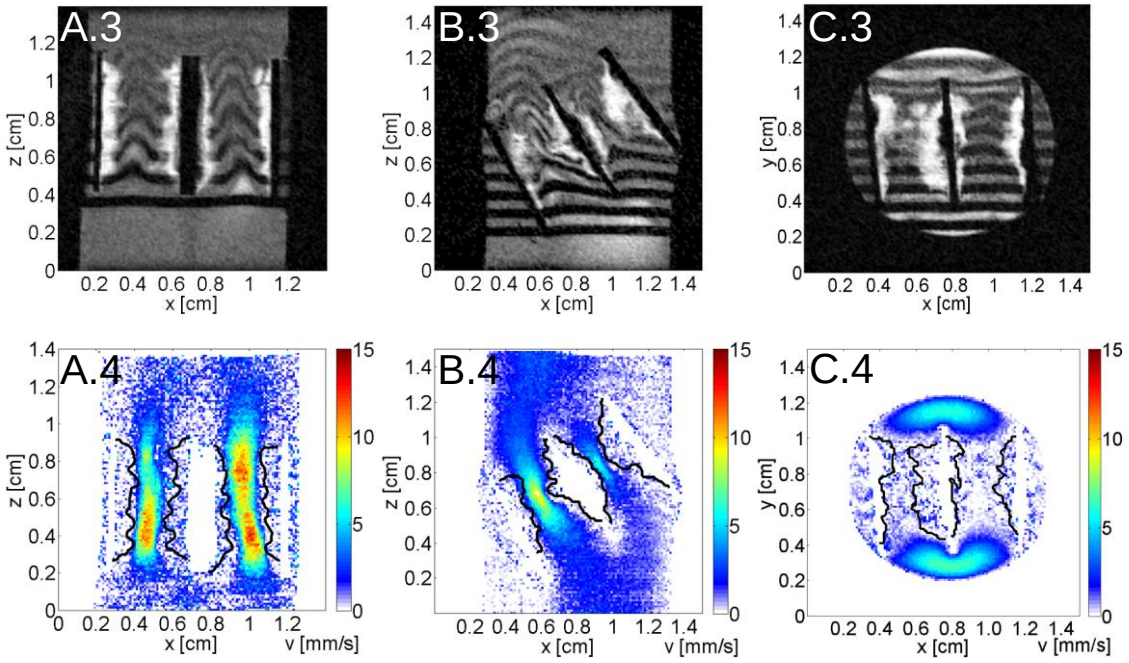

Figure 7-3: Scenarios (A - C) of carriers with biofilm measured at the green layer plane (see Figure 7-1). In MSME images (A.3, B.3 and C.3) white areas with high intensities indicate biofilms; black areas showing no signal represent tube and carrier material. Black lines in FLOW-PC images (A.4, B.4 and C.4) mark the biofilm superposed from MSME images. The color bar encodes the flow velocity in mm/s in FLOW-PC images.

The biomass grew on the whole inner surface of the carriers but not visibly outside on external surfaces. This originates from enhanced shear stress, collisions with other carriers in the reactor, and subsequent abrasion of biofilm (Odegaard 2006). In A.3, B.3 and C.3 biofilm appear as light gray areas attached to the carrier material (black). The contrast is provided due to the quite different relaxation times of the materials: the polymeric carrier material has a short longitudinal relaxation time T_1, but also a short transverse relaxation time T_2 such that the magnetization is decayed before being refocused to an echo in MSME and FLOW-PC. Water exhibits a long T_1 relaxation time in the order of 2 - 3 s, which is shortened

in the biofilm. This also applies to the transverse relaxation time T_2 in the biofilm. Despite a similar ^{1}H spin density in water and biofilm containing up to 95 % water (Neu *et al.* 2010), a good contrast can be achieved by exploiting these relaxation differences. Thus, no contrast agents were needed to improve the contrast between biofilm and bulk liquid unlike other studies (Manz *et al.* 2003, Seymour *et al.* 2004a). The images have a maximum spatial resolution of 103 µm/pixel which is sufficient to analyze biofilm structure at the meso-scale.

In the corresponding FLOW-PC images (A.4, B.4 and C.4) the biofilm/bulk interface is indicated as a black line. These lines are the result of the superposition of the MSME information of the biofilm surface position from binary MSME datasets and the FLOW-PC velocity maps. The transfer of the biofilm surface coordinates to flow velocity maps are in a good agreement with the surrounding flow field. The carrier in Figure 7-3, A.3 contains a relatively equal distributed biomass along the carrier height; in comparison, the biofilms in B.3 do have a more complex morphology. The images of these scenarios might suggest that the orientation of the carrier relative to the upstream flow had an impact on the biofilm morphology due to detachment. But the biofilm carriers were treated in the same way prior to the measurements. Biofilms were thoroughly rinsed with water to remove residual substrate and loose biofilm parts. No biofilm detachment was expected to happen during the flow experiments. These stable biofilm structures affect the local flow regime as summarized in Table 7-2: $\bar{v}$ increased by a factor of 1 - 2.2 and v_{max} by a factor of 1.9 - 2.7 compared to the blank carrier in scenarios A and B. In the case of scenario B the increase of the mean flow velocities due to biofilm was around 10 % (B.2 and B.4 in figure 3 and 4) while in scenario A the values doubled. As the flowing water is forced through the carrier to different extent in the three scenarios, the reasons are the reduction of the cross section while keeping the overall flow rate constant, and the fact that the biofilm disturbed the symmetry of the flow system. This leads to disturbed flow constraints by the spatially heterogeneous biofilm structures (Manz *et al.* 2005, Wagner *et al.* 2010a). Furthermore, blocking and distraction of the primary flow due to biofilm structures which produce flow components in different directions are possible (Gjersing *et al.* 2005, Hornemann *et al.* 2009, Seymour *et al.* 2004a). The mentioned behavior can be found in the velocity histogram in Figure 7-4.

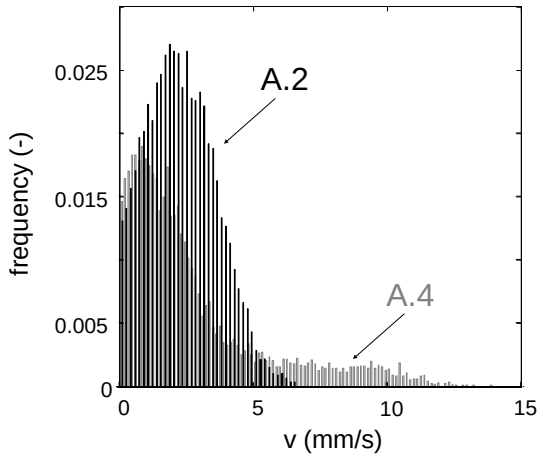

Figure 7-4: The histogram data in black refers to image A.2 of the blank carrier of Figure 7-2 and the histogram in gray refers to image A.4 of the carrier with biofilm from Figure 7-3. The distribution of the flow velocities of the blank carrier is broadened compared to the one of the biofilm loaded carrier.

The distribution of the flow velocities of the blank carrier was compared to that of the biofilm loaded carrier. For image A.4 ($\bar{v}_{(3ml/min)}$ = 4.30 mm/s) the velocity distribution is broadened and differs from the histogram of the blank carrier in A.2 ($\bar{v}_{(3ml/min)}$ = 2.40 mm/s) because of enhanced surface effects caused by the biofilm. The same is valid for high velocities due to channeling as a consequence of the reduced biofilm-free space in the carrier. Focusing again on the flow velocity maps in Figure 7-3, as expected, the flow velocity has its highest values of $v_{max(3ml/min)}$ = 14.02 mm/s for A and 9.41 mm/s for B at the centerline and drops towards the biofilm surface. Very low flow velocities (blue color scale) in the biofilm itself and stagnation were detected mainly in the outer regions and assumedly less dense parts of the biofilm, images A.4 and B.4. Manz *et al*. (2003) and others (Vogt *et al.* 2013) showed that there is no advective flow through biofilm cell clusters as long as they are not fractured (Stewart 2012) or patchy. In scenario C, the presence of the biofilm has almost no influence on the local flow field within the carrier as visible in image C.4. The flow regime is comparable with that of the blank carrier in figure 3, C.2. The mean flow velocities of $\bar{v}_{(3ml/min)}$ = 1.66 mm/s (C.2) and 1.76 mm/s (C.4) slightly increased due to additional restrictions caused by the biofilm. This scenario represents the case where mass transfer and substrate availability will be extremely low in the center of the carrier and mainly driven by diffusion. As mass transfer in biofilms is driven by both advection and diffusion (De Beer *et al.* 1994a), the flow velocity maps can be divided into regions which have a high (A.4 and B.4) and a low (C.4) impact on mass transfer processes. Odegaard (2006) reported that substrate penetration into biofilms of e.g. ammonia is partly limited to < 100 µm. Hence the biofilm thickness plays a key role with respect to substrate supply as this study deals with thick and dense biofilms. These K1 biofilm carriers are typically applied for treatment of industrial and municipal waste water worldwide (Wessman *et al.* 2004). An optimization of the carriers can e.g. be achieved by modification of their height. While other studies showed that the

carrier size and shape do not influence the performance of a WWT plant (Odegaard *et al.* 2000), the results of this study emphasize that the carrier orientation and biofilm morphology are crucial for mass transport processes in µm-scale. Although the scenarios are only models for possible situation in a MBBR, the results show already the variety of flow fields in the carriers, which need to be statistically weighted for a thorough description of the overall behavior of mass transfer in such reactors.

7.3.3 Correlation of flow distribution and biomass distribution

Until this point, only results only from two carrier sections in an *xz* plane of scenario A and B of a carrier were taken into account (see green layers in Figure 7-1). For a comprehensive interpretation the whole carrier has to be considered including the *yz* plane (additional red layer shown in Figure 7-1). The used biofilm carrier can be understood as an interconnected system of four sections in which the fluid/bulk liquid will be distributed unevenly. The flow distribution strongly depends on the amount of biofilm present in each section. Table 7-3 provides the biofilm morphology and structural parameters of each section of the measured layers in the *xz* and *yz* planes. To describe the biofilm morphology the maximum biofilm thickness of each biofilm, defined by the position of *left* and *right* in each section a and b was calculated. Complementary, Figure 7-5 explains how the biofilm influences the flow distribution in the carrier depending on biofilm thickness and occupation in each section. The results of the flow distribution of the total volumetric flow passing through the four carrier sections of scenarios A and B at volume flow rates of 1, 2 and 3 ml/min depending on the biomass occupation is summarized. The fractions of the total volumetric flow were calculated based on the flux density of the FLOW-PC 2D data. Due to the large stagnant areas scenario C was not taken into account.

Table 7-3: Biofilm morphologies shown in MSME images of the green (*xz*) and red (*yz*) layer of scenario A and B, see Figure 7-1. The table presents of the data of biomass occupation, percentage of the area the biofilm covers in each section and the maximum biofilm thickness (L_{max_left}/L_{max_right}) of each biofilm in section a and b (n = 3), respectively.

carrier section	biomass occupation (mm^2)	coverage of section (%)	max. biofilm thickness L_{max_left} (mm)	max. biofilm thickness L_{max_right} (mm)	image
A.3 *xz* a	8.5 ± 0.26	28.0	1.1 ± 0	1.4 ± 0	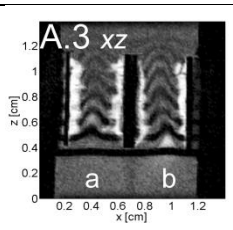
A.3 *xz* b	5.8 ± 0.29	20.6	0.9 ± 0.09	1.0 ± 0	
A.3 *yz* a	7.6 ± 0.21	25.4	0.8 ± 0.05	1.7 ± 0.05	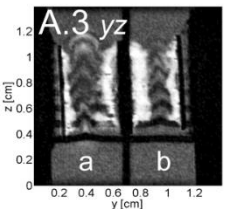
A.3 *yz* b	10.4 ± 0.26	40.0	1.3 ± 0.05	0.8 ± 0.05	
B.3 *xz* a	5.1 ± 0.82	18.7	1.2 ± 0.1	1.4 ± 0.09	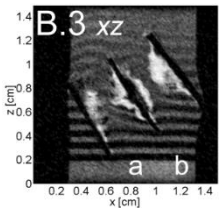
B.3 *xz* b	6.7 ± 0.77	25.9	0.7 ± 0.09	1.8 ± 0.05	
B.3 *yz* a	5.2 ± 0.76	18.5	1.6 ± 0.1	0.6 ± 0.1	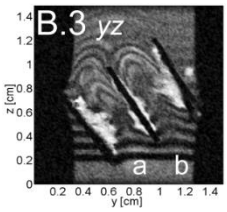
B.3 *yz* b	4.6 ± 1.13	16.0	0.6 ± 0.05	1.8 ± 0.14	

For scenario A the biomass occupation varies from 5.8 to 10.4 mm^2 (see black columns in Figure 7-5). The corresponding coverage of the total section is also delivered by Table 7-3 where the maximum is 40 % in A.3, *yz* plane, section b with the highest biomass occupation of 10.4 mm^2. Accordingly, this plane corresponds to the lowest flow proportions of 12.3 - 15.6 % followed by A.3 *xz* a with 18.1 - 24.3 %. The biofilm of A.3 *yz* b reached a maximum biofilm thickness of 1.3 mm and a minimum channel width of 1.3 mm, see Table 7-3. The data of the flow distribution in scenario A (Figure 7-5, upper graph) allows to observe that a high flow resistance is created in sections with high biomass occupation (A.3 *yz* b) or by biofilm with expanding structures (A.3 *xz* a). This leads to flow evasion through less covered sections and

in turn to increased flow velocities (A.3 *xz* b and A.3 *yz* a). One consequence might be a constant biofilm thickness in these less covered sections because of higher shear stress and in turn increased biofilm thickness in sections filled with higher biomass content because of flow velocity reduction.

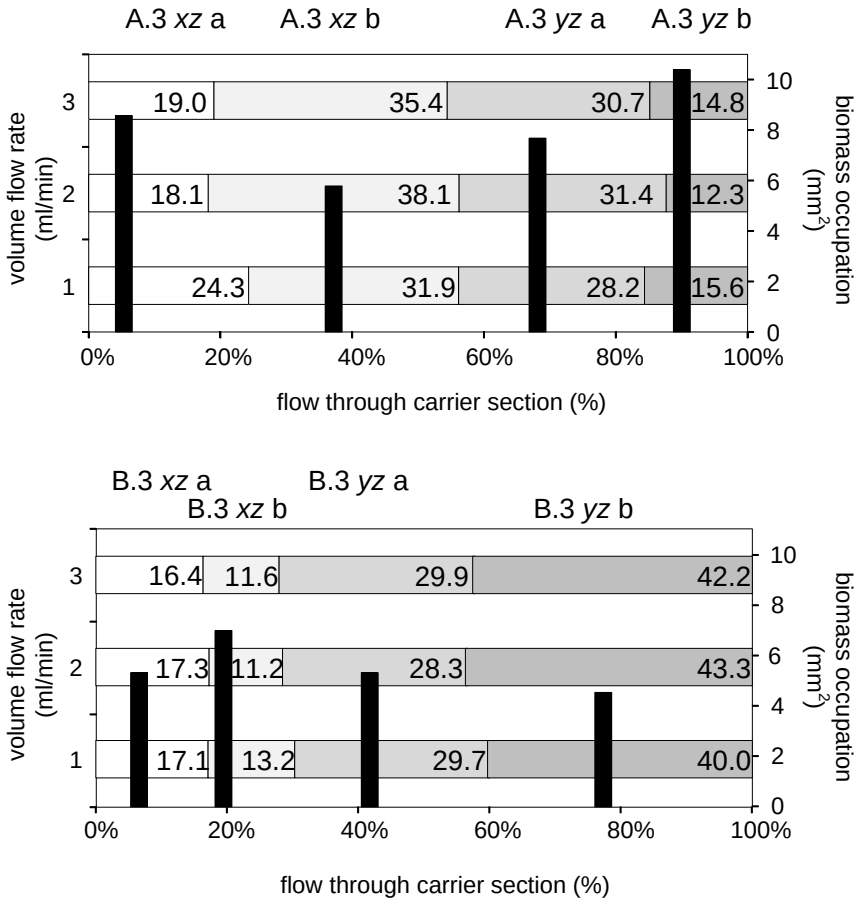

Figure 7-5: Correlation of flow fractions and biomass occupation for a whole carrier of scenarios A (above) and B (below): the path ways of the forced flow through the carrier is illustrated as percentage for each section a and b of the green and red layer (compare Table 7-3) with varying biomass occupation (indicated as black bars, values see right *y*-axis) measured for the three different volumetric flow rates (left *y*-axis).

Due to flow velocities and high biomass content, the diffusion of solutes is probably additionally hampered, as diffusion limitation is commonly the limiting factor in biofilm systems with high biomass occupation (Boltz and Daigger 2010). In scenario B the influence of the biofilm morphology is even more pronounced. The biomass occupation varies only in the range of 4.6 to 6.7 mm^2 but a huge difference exists between the flow distributions. The biofilm carriers in B.3 are characterized by narrow pathways having a minimum channel width of 1.1 mm (B.3 *xz* a) or 0.8 mm (B.3 *xz* b) restricting the fluid flow. This leads to the fact that B.3 *yz* a and B.3 *yz* b conduct around 70 % of the total volumetric flow rate by a biomass occupation of 5.2 and 4.6 mm^2. As mentioned, the biofilm morphology drives the fluid flow by comparing the flow fractions mean values in sections B.3 *xz* a (16.9 %) and B.3 *yz* a (29.3 %): the sections

have a comparable amount of biomass but distinct flow fractions. This behavior can be explained by the distinct biofilm thickness L_{max_left} and L_{max_right}, see Table 7-3. In B.3 *xz* a narrow channel is created with maximum biofilm thicknesses of 1.2 mm and 1.4 mm. In comparison B.3 *yz* a shows more open structures with thicknesses of 1.6 mm and 0.6 mm and a minimum channel width of 1.5 mm. Consequently, biofilms are able to partially close sections of a carrier and block fluid flow. Important to state at this point is that there is no linear correlation between the biomass occupation and the percentage of the flow through the carrier sections. The unclear correlation between biomass occupation and percentage of flow through a carrier section in scenario A and B (Figure 7-5) can be explained by the presented biofilm morphologies where the maximum biofilm thickness and minimum channel width are influencing parameters. The data are consistent for the volume flow rates of 1, 2 and 3 ml/min. The presented data is valid for a defined measurement environment where the carrier material was fixed in the tube. In reality the biofilm carrier move randomly in the MBBR and might change their position relative to the upstream flow angle. To be closer to realistic conditions, the applied volumetric flow rates were kept low at 0.21 - 0.64 mm/s. The different flow regimes in the carrier sections have an impact on the local substrate supply. As commonly known the substrate supply is enhanced by the higher flow velocities by compression of the concentration boundary layer and higher advection, as experimentally shown in a biofilm carrier (Masic *et al.* 2010). Other studies conducted in tube reactors showed that blockage by biofilm growth (Manz *et al.* 2003) and metal deposition (Nott *et al.* 2005b) can also increase the mean flow velocities. Similar effects are found in the biofilm carriers; the bulk liquid flow in tubes cannot by-pass the blocked regions. The presented results can be a base for the progress of other research fields as reactor engineering and carrier design by predictive modeling. Simulations can be experimentally validated with the help of MRI measurement techniques (Pintelon *et al.* 2012, Seymour *et al.* 2007). In water technology MRI measurements can provide complementary data, as e.g. for biofouling of membranes (Creber *et al.* 2010). Furthermore CFD simulations can be used to verify the experimental MRI results and interpretations and *vice versa*, e.g. shown in a study about flow cell geometries (Dalitz *et al.* 2012). Additional research is still needed in MBBR biofilm hydrodynamics for a better understanding of mass transport and linking between the biofilm and reactor-scale.

7.4 Summary

- MRI represents the ideal tool to investigate the undistributed interactions between the biofilm and its surrounding flow field. It was visualized that the physical structure and morphology of the

biofilm has a crucial impact on the flow velocity in the bulk water. Results give indications for the mass transport of solutes and particulate compounds in the water matrix.

- The orientation of the carrier to upstream flow angle was a dominant factor for the local flow velocities at the biofilm surface. A rotation of 20° of the blank carrier material caused ~10 % increase of the mean flow velocity in the bulk water. At the orientation of a 90° angle to the upstream flow direction, regions of stagnation were formed, where almost no fluid exchange was observed. Then, diffusion is the predominant transport process for fluids and its dissolved and particulate components.

- Through the combination of MSME and FLOW-PC measurements, the influence of the biofilm structure on the local flow field was examined. The presence of the heterogeneous biofilm increased the local flow velocities in the inner face of the carrier up to factor 2 compared to the blank carrier. Therefore, the advective transport was increased.

- Structural parameters of the biofilm (such as e.g. the biofilm thickness and biofilm occupation) gave indications for their surrounding local flow regime. However, there was no linear correlation between the fluid flow through the carrier and biomass occupation due to uneven flow evasion through open pathways.

8 EVALUATION OF THE USED METHODS

8.1 Magnetic susceptibility balance

This dissertation demonstrated, for the first time, the successful combination of MSB and MRI for the detailed investigation of the interactions between inorganic Fe_3O_4-NP and biofilm systems. This new analytical approach enabled the time resolved quantification and visualization of Fe_3O_4-NP within the biofilm matrix in an *in-situ* and *non-invasive* manner.

The MSB has turned out to be a promising method to follow the distribution of Fe_3O_4-NP in heterogeneous biological systems. In this context, MSB has never been used before. In particular, specific data on the concentrations of Fe_3O_4-NP in the bulk water and in the biofilm matrix was obtained - independently from the water composition and biofilm matrix. The generated results in chapter 4 and 6 provide reliable data on the biosorption of Fe_3O_4-NP and improve the general understanding of their distribution in biological systems, such as biofilms in WWT. This sensitive method satisfies specific needs for the quantification of Fe_3O_4-NP in complex samples and delivers replicable results (error < 2 %) at economic cost (purchase price < 20,000 €) compared to other methods for the quantification of Fe_3O_4-NP (e.g. atomic spectroscopy (~ 100,000 €)) by:

- simple handling and fast (measurement time < 60 s) data acquisition
- small sample volumes (10 - 200 µL) without sample preparation
- *in-situ* und *non-invasive* measurement in liquid, solid and mixed phase (liquid-solid) samples
- quantification of e.g. Fe_3O_4-NP down to 100 µg/L range, with the possibility to easily enrich the concentration by magnetic separation.

The MSB overcomes certain analytical limitations for the quantification of inorganic Fe_3O_4-NP of more complicated and costlier analytical techniques, such as atomic spectroscopy where a chemical digestion of metallic ENP is needed (see section 3.1.2). Furthermore, the application of a MSB opens the door to investigate other ENP with magnetic properties (e.g. Cu-based NP). In this context, using ENP with a magnetic core and different surface coatings (e.g. Ag, TiO_2, Ce and organic coatings) appears highly attractive to investigate the behavior of ENP in environmental samples and the impact of the particle surface coating (e.g. on toxicity, mobility and biosorption).

8.2 Magnetic resonance imaging

MRI is a high performance and multifaceted technique allowing the completely *non-destructive* and *in-situ* 2D- and 3D-imaging of Fe_3O_4-NP within the biofilm matrix, while additional information, such as

water dynamics (diffusion and flow velocity measurements) can be acquired. Compared to MRI, other imaging techniques, such as electron microscopy and fluorescence microscopy are either destructive to the biofilm, do not reveal the real biofilm structure, or require special (e.g. fluorescent) ENP or dyes for the visualization of the ENP within the biofilm matrix. However, MRI exhibits very high purchase and maintenance costs and is limited in its spatial resolution. Using the currently available NMR hardware, a spatial resolution down to a few tens of µm is feasible, which is, so far, not sufficient to explore the cellular uptake of Fe_3O_4-NP. Advantageously, the relatively large field of view (in this dissertation up to 20 mm x 20 mm) allows a representative overview on the whole biofilm sample.

In chapter 4 and 6, the biosorption and immobilization of differently sized and functionalized Fe_3O_4-NP within fluffy biofilms was successfully visualized. The presented images are only phrasing local concentrations of Fe_3O_4-NP in the biofilm matrix by changes in the image contrast and do not give quantitatively information yet. However, perspectives for a more quantitative analysis are given by concentration maps of Fe_3O_4-NP. Those concentration maps would provide data on e.g. penetration, transport and wash out of Fe_3O_4-NP in the biofilm matrix. The acquired concentration maps would require intensive mathematical image processing for the interpretation of the data. Another possible application of MRI address the mass transport of contrast agents into the biofilm matrix using effective diffusion coefficients, as demonstrated by Ramanan *et al*. (2013) and Phoenix *at al*. (2008). This paves the way for the investigation of varieties of ENP (modified as MRI contrast agents) in the context of their environmental fate.

9 SUMMARY AND PERSPECTIVES

9.1 Summary

The aim of this dissertation was to examine the interactions of inorganic Fe_3O_4-NP with real biofilm systems. Exposure experiments were conducted to qualitatively and quantitatively characterize the biosorption and removal of Fe_3O_4-NP in batches, flow cells and in a lab-scale MBBR. The investigations focused on the influence of the following parameter:

- **chemistry of the water matrix,**
- **particle size and surface functionalization and**
- **exposure time**

on the interaction of Fe_3O_4-NP with two different types of biofilms (fluffy and compact structure). An overview of the conducted experiments is given in Table 1-1. From the achieved results, certain conclusions were compiled, which contribute to the current knowledge about the interaction processes (highlighted by frames in Figure 9-1).

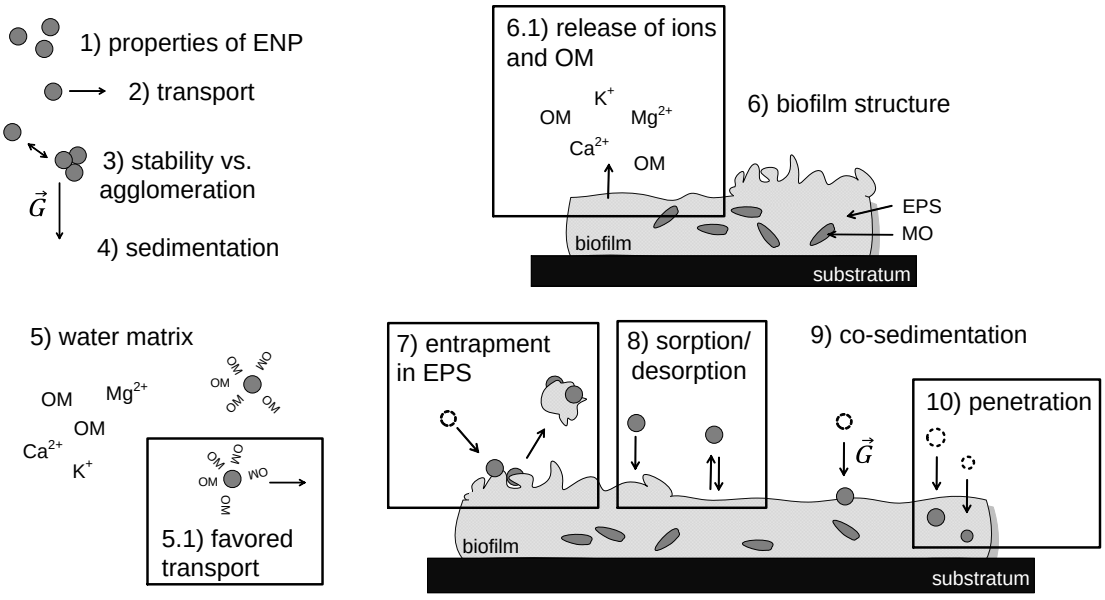

Figure 9-1: Graphical summery of the conclusions found in this dissertation (framed), which contribute to the known interaction processes between ENP and biofilms (summarized in 2.1.2). Numbers in this figure refer to environmental parameters and processes involved in the interactions between ENP and biofilms exhibiting different physical structures. Abbreviations: OM: organic matter, MO: microorganisms, EPS: extracellular polymeric substances, $\vec{G}$: force of gravity. The proportions in this figure are out of scale.

Within this dissertation, the summarizing term "biosorption" is used to describe all chemical and physical sorption processes for the attachment of ENP to biofilm. With the aim to trace the fate and biosorption of ENP in biofilm systems, no distinction between different interaction mechanisms in terms of molecular interactions or physical forces is compiled within this work. However, the indications for predominant interaction processes are given in the presented case studies. In the following, numbers in bold refer to Figure 9-1.

9.1.1 Influence of water matrix

Granular biofilms were exposed to Fe_3O_4-NP coated with PVA in series of batch experiments (chapter 4). The results obtained by MSB show that Fe_3O_4-NP were only removed by 5 - 35 % from the bulk water, which is significantly less compared to removal efficiencies found in the literature (see Table 2-1). This might be due to the stabilization of Fe_3O_4-NP by dissolved and particulate organic matter (OM) in the bulk water **(5)**. OM was released by the biofilm matrix (EPS) itself **(6.1)** and correlated with the total suspended solid (TSS) concentration of the granular biofilms. The biofilm also released low amounts of ions, which thus did not have a significant influence on the removal of Fe_3O_4-NP from the bulk water in this case **(6.1)**. Unexpectedly, the biosorption of the Fe_3O_4-NP onto the granular biofilms was low (only 2.4 % of input Fe_3O_4-NP) and reversible as desorption after rinsing occurred **(8)**. This can be attributed to the smooth and compact structure of the granular biofilms **(6)**, which most likely hinders the interactions. The results suggest that the interactions of Fe_3O_4-NP with granular biofilms are hampered and instead of biosorption, other processes such as co-sedimentation **(9)** might be responsible for the desired removal of Fe_3O_4-NP from the bulk water.

In conclusion, OM turned out to be a predominant parameter of the water matrix responsible for mass flows of Fe_3O_4-NP in granular biofilm systems. This finding can easily be transferred to other natural and technical biofilm systems due to the omnipresence of OM. The stabilizing effect of organic molecules from EPS on ENP in the bulk water has been demonstrated for freshwater biofilms as well (Kroll *et al.* 2014). However, which specific organic molecules of EPS preferentially stabilize ENP and their impact on the degree of biosorption requires further research.

9.1.2 Influence of particle properties

To explore the influence of the particle properties on the degree of biosorption, fluffy biofilms were exposed to differently sized and functionalized Fe_3O_4-NP under static conditions (only diffusion dominated transport) (chapter 5). The visualization using MRI revealed that Fe_3O_4-NP mainly attached to the outer biofilm layers - independent of their particle surface functionalization, i.e. organic molecules (dextran, starch or hydroxyl (chapter 5)) or inorganic shell (silica (chapter 6)). The attachment happened

quickly (within minutes) and no full penetration of the biofilm matrix was observed. Despite the particle surface, the particle size is a decisive parameter **(10)**: smaller Fe_3O_4-NP (diameter of 20 nm) visibly penetrated deeper into the biofilm matrix than larger ones (80 nm). Interestingly, the surface functionalization of Fe_3O_4-NP did not significantly influence the penetration depth into the biofilm matrix. After an exposure of 14 days, all investigated Fe_3O_4-NP were irreversibly immobilized within the fluffy biofilm matrix **(8)** and no desorption occurred.

In conclusion, these results imply that especially the particle size might be a key factor for the estimation of mass flows of Fe_3O_4-NP in biofilm systems. Most commercially available ENP form large particle agglomerates (>100 nm) in environmental water matrixes (Petosa *et al.* 2010, Zhang *et al.* 2008), therefore, the penetration of ENP into biofilms might be hampered approaching more realistic scenarios. Research on the combined effect of particle size and different organic molecules (OM/NOM) should provide more specific information about the trade-off between penetration into the biofilm and stabilization in the bulk.

9.1.3 Influence of exposure time

To study the influence of the exposure time on the interactions of silica coated Fe_3O_4-NP with fluffy biofilms, exposure experiments in continuous flow systems (flow cell and MBBR) were performed (chapter 6). Fe_3O_4-NP were quantified using MSB. The results prove that even at complex hydrodynamic conditions, Fe_3O_4-NP were stabilized in the bulk water by OM and, therefore, their transport was enhanced **(5.1)**. Due to the enhanced transport and hampered interaction of Fe_3O_4-NP with biofilm in the flow field, the exposure time was of minor influence. The results demonstrate that in both systems, flow cells and in a MBBR, 57 - 65 % of the input Fe_3O_4-NP were transported through the effluent. Consequently, the retention capacity of the used biofilm systems was poor. Only 16.6 % of the input Fe_3O_4-NP sorbed onto the biofilms. However, the biosorption of Fe_3O_4-NP happened quickly within minutes. After 3 h of exposure in the MBBR, detachment of the outer biofilm parts loaded with Fe_3O_4-NP has occurred and led to further washout of Fe_3O_4-NP **(7)**.

In conclusion, the exposure time is of subordinated relevance for the initial interaction of Fe_3O_4-NP with the biofilm system as the biosorption occurred quickly and the transport of Fe_3O_4-NP in the bulk water was dominant. However, the time scale of observation has to be considered when looking at the long-term effects of the exposure (e.g. biofilm detachment, desorption etc.). Concerning WWT systems, these findings are of great importance: the retention of ENP is not guaranteed by the biofilm system and might therefore depend on other water treatment steps (see section 9.2.2).

9.1.4 Influence of biofilm structure on flow field

To estimate the transport of Fe_3O_4-NP to the biofilm surface - being a perquisite for their interaction (**2**) - the flow field in a carrier based biofilm was investigated (in absence of Fe_3O_4-NP) in chapter 7. The results obtained by MRI demonstrate that the biofilm structure had a significant influence on the surrounding flow velocities on the µm to mm scale. In carrier sections with a high biofilm occupation the flow resistance is increased, e.g. flow velocities are significantly decreased and stagnation can occur in narrow pathways created by the biofilm. Thereby, the biofilm thickness and coverage of the biofilm are important factors to consider. Depending on the orientation of the carrier to the flow field, this effect leads to flow evasion through less biofilm covered sections. Those sections experience higher flow velocities and the possible risk of biofilm detachment. Nevertheless, there was no clear correlation between biofilm coverage and flow ratio. Within the biofilm matrix only diffusion dominates the transport of fluids.

In conclusion, the biofilm structure determines the local flow regimes and therefore, the diffusive and advective transport of ENP which is critical for their fate in biofilm systems. A closer look into this topic is needed by further investigations involving ENP, such as Fe_3O_4-NP serving as MRI contrast agents.

9.2 Evaluation and perspectives

9.2.1 Influence of biofilm structure

The biofilm's physical structure is a predominant parameter for the fate of Fe_3O_4-NP in biofilm systems. To gain quantitative information about the biosorption, the concentration of Fe_3O_4-NP in two different types of biofilms (compact and fluffy structure) was measured using MSB (chapter 4 and 6). Figure 9-2 depicts a graphical summery of the influence of the biofilm structure on the fate of Fe_3O_4-NP based on the conducted experiments.

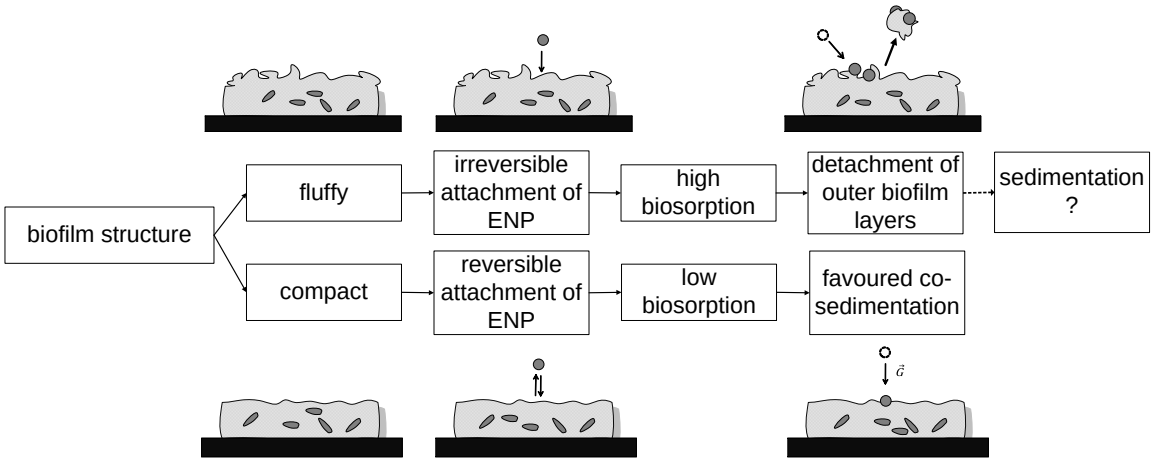

Figure 9-2: Graphical summary: influence of the biofilm structure (fluffy or compact) on the behavior and biosorption of ENP (Fe_3O_4-NP) in biofilm systems elucidated within this dissertation. This figure is complementary to Figure 9-1 and Figure 2-2. The proportions of the figure are out of scale.

The results achieved in chapter 4 highlight that the interactions with Fe_3O_4-NP were hampered by a smooth surface and compact biofilm structure (e.g. granular biofilms). The attachment of Fe_3O_4-NP was reversible (desorption occurred) and most of the Fe_3O_4-NP were loosely bound to the surface of the compact biofilm. In turn, this was related to a low biosorption: the maximum biosorption for biofilms with compact structures was 1.9 µg Fe/mg TSS (at an exposure load of 96 µg Fe/mg TSS) after 18 h of exposure time in a closed batch system (chapter 4). Reasons for the low biosorption might be the stabilization of Fe_3O_4-NP by OM and the enhanced transport in the flowing bulk water, as mentioned earlier. This gives indications that co-sedimentation processes are favored. In future experiments, the loading of Fe_3O_4-NP for the investigated biofilms should be confirmed by sorption models.

In comparison, in biofilms exhibiting a fluffy structure the biosorption of Fe_3O_4-NP was irreversible and no desorption occurred under the investigated experimental conditions unlike the compact biofilms. The fluffy biofilm surface might favor an interaction by the entrapment of Fe_3O_4-NP in EPS leading to a higher (Gu *et al.* 2014) and more persistent biosorption. The maximum biosorption was 3.2 µg Fe/mg TSS

(at an exposure load of 10.9 µg Fe/mg TSS) after 3 h of exposure in a continuous flow system (MBBR, HRT ~ 5 h). In spite of the irreversible attachment, Fe_3O_4-NP gained mobility by the detachment of outer biofilm parts loaded with Fe_3O_4-NP after 3 h of exposure time (MBBR). However, the fate of the Fe_3O_4-NP in detached biofilm parts remains unclear, e.g. sedimentation might be favored.

9.2.2 Indications for the fate of ENP in WWT

Within this dissertation, in particular the retention capacity of the investigated biofilms systems was rather low and transport of Fe_3O_4-NP was favored. Being aware that the maximum concentrations of Fe_3O_4-NP in the compact and fluffy biofilms (1.9 and 3.6 µg Fe/mg TSS, respectively) cannot directly be transferred to other experimental conditions, they are in the same concentration range as those of other inorganic ENP in the literature (for different kinds of biomass): In sequencing batch reactors, a maximum concentrations of 10 µg Ag/mg TSS for Ag-NP after 177 days of operation (HRT of 10 h) (Yang *et al.* 2015) and 13.2 µg Ti/mg TSS for TiO_2-NP (HRT of 10 h) (Kiser *et al.* 2009) were reported. In a membrane bioreactor a maximum concentration of 28 µg Ag/mg MLSS (mixed liquor suspended solids) for Ag-NP after 285 d of operation (HRT of 16 h) (Yuan *et al.* 2015) was found. Nevertheless, also far lower biosolid concentrations of inorganic ENP (up to three orders of magnitude) have been reported by Gottschalk *et al.* 2013b. Due to the high variability, the need of strategies to control the release of ENP from WWT systems employing biofilms is emphasized. Assuming the transport processes to be favored in the biological treatment step and that detachment of ENP loaded biofilm parts can occur, the retention of ENP will depend on the efficiency of post settling (e.g. excess sludge system) or other separation processes such as filtration and membranes (Wang *et al.* 2012, Westerhoff *et al.* 2013, Zhang *et al.* 2008).

Additionally, the reversibility of the biosorption is a relevant factor to bear in mind for the estimation of mass flows of ENP in the environment. As the biomass from WWT is still disposed in landfills and applied to agricultural soils (Blaser *et al.* 2008, Brar *et al.* 2010), their release into the environment might be mitigated. The results lead to the conclusion that the investigation of the structure of the used biofilm systems (surface and inner structure) might help to estimate the degree and reversibility of the biosorption in a particular scenario.

9.2.3 Loose ends

- As demonstrated in this work, only minimal success was achieved in removing ENP from the water phase by various biofilm systems. Striking differences were seen in the degree of biosorption and immobilization of ENP in compact or fluffy biofilms structures. How do other

biofilm structures, such as streamers influence the biosorption of ENP in realistic water matrices? Results would give information about the environmental behavior of ENP.

- MRI was used to visualize the degree of penetration and immobilization of ENP within the biofilm matrix in a *non-invasive* and *non-destructive* manner. However, the interactions observed in this dissertation were on the µm to mm scale and did not consider interactions with single cells. Can the immobilization be correlated with the *nano*-specific toxicity in real biofilm systems? How is the penetration affected by specific organic molecules of EPS?

- The flow regime in real biofilm systems was determined (without ENP addition) highlighting that the biofilm structure drives the flow velocities. The next step would be to link the biofilm surrounding local flow field with advective and diffusive transport of ENP. How stable is the biosorption in a complex flow field, especially concerning desorption of ENP and changes in the biofilm structure?

APPENDIX

A.1 Theory of paramagnetic relaxation enhancement

To better understand PRE it is divided into two contributions in the most simple model: the interactions between the paramagnetic species with directly bound water molecules (inner sphere relaxation enhancement) and interactions with unbound or nearby diffusive water molecules (outer sphere relaxation enhancement). The paramagnetic relaxation $\left(\frac{1}{T_i}\right)_{\mathrm{p}}$ is the sum of the contributions by the outer sphere $\left(\frac{1}{T_i}\right)_{\mathrm{OS}}$ and the inner sphere relaxation $\left(\frac{1}{T_i}\right)_{\mathrm{IS}}$.

$$\left(\frac{1}{T_i}\right)_{\mathrm{p}} = \left(\frac{1}{T_i}\right)_{\mathrm{OS}} + \left(\frac{1}{T_i}\right)_{\mathrm{IS}} \qquad \text{Equation A.1-1}$$

Both phenomena are described in diverse theories and equations (Bertini *et al.* 2001, Bloembergen 1957, Freed 1978, Solomon 1955). The inner sphere relaxation attributes to the hyperfine interactions between the electrons of the contrast agents and the protons (nuclei) by dipole and other spin interactions. Generally, the contribution by the inner sphere relaxation depends on the molar concentration of the paramagnetic compound c_{p} in mg/L, the number of coordinated water molecules at paramagnetic ion *p*, the relaxation time of the inner sphere bound water molecules ($T_{1\,\mathrm{M}}$ in s) and their mean residence time τ_{M} in s for chemical exchange mainly related to T_1.

$$\left(\frac{1}{T_1}\right)_{\mathrm{IS}} = \frac{c_{\mathrm{p}}}{55.6} \cdot \frac{1}{T_{1\,\mathrm{M}} + \tau_{\mathrm{M}}} \qquad \text{Equation A.1-2}$$

The more paramagnetic centers and the more bonded water molecules having a short residence time in a contrast agent, the stronger the inner sphere contribution will be resulting in a shortened T_1. $T_{1\,\mathrm{M}}$ is influenced by the molecular rotational correlation time τ_{R} which is describes the rotational molecular tumbling time of the whole molecule. Molecular tumbling causes local magnetic field fluctuations suitable to enhance T_1 and T_2 relaxation times. The higher the molecular size and the more immobilized the contrast agent is, the lager τ_{R} will be. In addition, the correlation time of chemical exchange of the water molecules play a major role.

Summarizing, the mechanisms for the inner sphere relaxation depend on large number of interactions and time scales as often described by Solomon and Bloembergen equations (Bloembergen 1957) where $T_{1\,\mathrm{M}}$ is further categorized by dipole-dipole interactions (interaction proton and electron dipole) and scalar interactions (exchange interaction between proton and electron spins as well as Curie contribution). For

more specific information please consult textbooks and review articles (Bertini *et al.* 2001, Bottrill *et al.* 2006, Laurent *et al.* 2007).

The outer sphere relaxation is based mainly on the interaction of nearby diffusing or loosely bound water molecules near the paramagnetic molecules. The outer sphere relaxation is a more complex and not well understood and describable phenomenon of dynamics and diffusion. Generally, this process depends on the electronic relaxation time of the paramagnetic ion and the translational diffusion correlation time τ_D. τ_D is defined by $\frac{d^2}{D}$ depending on the sum of diffusion coefficients D in m^2/s for the water molecules and paramagnetic center and their closest distance to each other d in m. Consequently, the proximity of the water molecules to the paramagnetic ion is important to consider as well as the correlation between τ_D, temperature and viscosity. For nanoparticles as MRI contrast agents the outer sphere relaxation is dominant as no direct binding site for water molecules are available (Bertini *et al.* 2001, Caravan *et al.* 1999, Laurent *et al.* 2008).

A.2 DLVO theory

From the thermodynamic point of view, the DLVO theory helps to understand the total interaction energies between particles when approaching other particles or solid surfaces. The total interaction energy between two particles is the sum of the electrostatic repulsion energy (double layer force and born force) and or VAN-DER-WAALS forces as a function of the distance between two particles or a particle and a solid surface. DLVO basically describes that the repulsive forces are high and attractive forces are low when particles are far away from each other. The closer the particles are approaching each other overcoming a the energy barrier – the higher the attractive forces and aggregation occurs (Derjaguin and Landau 1941, Israelachvili 2010).

A.3 COD concentration during MBBR operation

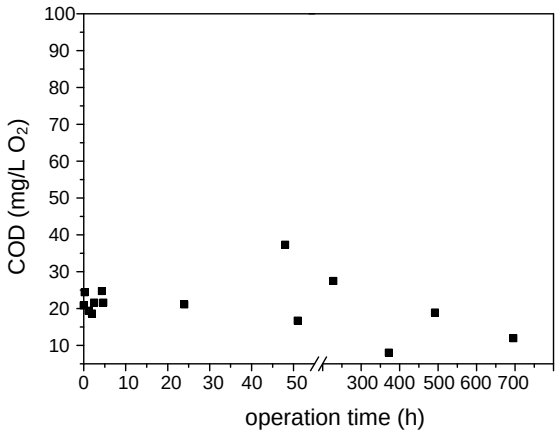

Figure A- 1: COD concentration during the MBBR experiment (operation time after addition of silica coated Fe_3O_4-NP).

A.4 Curriculum vitae

Maria Pia Herrling, born on 13th of April in 1988 in Pforzheim, Germany
E-Mail: mpherrling@gmail.com

Academic career and research

05/12-dato	Research associate (PhD candidate), Chair of Water Chemistry and Water Technology (Faculty of Chemical Engineering and Process Engineering) at Karlsruhe Institute of Technology (KIT), Germany under the guidance of Prof. Harald Horn and Prof. Susanne Lackner
05/14-08/14	Research stay at the Magnetic Resonance Laboratory of the Center for Biofilm Engineering (CBE), Montana State University, Bozeman, USA under the guidance of Prof. Sarah Codd and Prof. Joseph Seymour
10/07-04/12	German diploma with distinction in Geoecology, KIT, Germany Main subjects: water technology and water chemistry, geographic information systems, landscape ecology and soil mineralogy
09/09 -02/10	Student exchange program at the Polytechnic University of Catalonia, Barcelona, Spain, Attendance of the master program environmental engineering
07/98-07/07	German Abitur at Reuchlin-Gymnasium, Pforzheim, Germany

Awards, grants and programs

01/14-12/15	Doctoral scholarship (2 years) financed by the German Carl-Zeiss Foundation
01/15	Networking-Grant for international research cooperation founded by the Karlsruhe House of Young Scientists (KHYS), KIT
05/14-08/14	Research Scholarship for the Research stay at Montana State University, USA founded by Karlsruhe House of Young Scientists (KHYS), KIT
01/14-dato	Attendance at the Graduate School for Climate and Environment (GRACE), key qualification program for young researches, KIT
07/13-10/14	Career-building and mentoring-program (X-Ment) for junior female leaders founded by the European Social Fund, KIT
08/13	Winner of the "Digital Image Beauty Competition", International Conference of Magnetic Resonance Microscopy 2013, Cambridge, UK

Engineering experience

07/11-01/12	Graduate student at the Institute of Geochemistry at KIT in cooperation with the engineering consultants ARCADIS, Karlsruhe, Germany Diploma thesis: "Analysis of water and particulate matter in the groundwater remediation plant Mannheim Luzenberg"
03/10-01/13	Student assistant at ICP engineering consultants for water and soil, Karlsruhe, Germany

NOMENCLATURE

Abbreviations

CLSM	confocal laser scanning microscopy
EMNP	engineered magnetic nanoparticle
ENP	engineered nanoparticle
EPS	extracelluar polymeric substances
FID	free induction decay
FLOW-PC	flow phase contrast sequence
FT	fourier transform
HA	humic acid
ICP-OES	inductively coupled atomic emission spectroscopy
IS	inner sphere relaxation
MBBR	moving bed biofilm reactor
MBR	membrane bioreactor
MO	microorganisms
MRI	magnetic resonance imaging
MS	magnetic susceptibility
MSB	magnetic susceptibility balance
MSME	multi slice multi echo sequence
NMR	nuclear magnetic resonance
NOM	natural organic matter
rf	radio frequency
NP	nanoparticle
ob (index)	observed
I	spin
OECD	Organisation for Economic Cooperation and Development
OS	outer sphere relxation
OCT	optical coherence tomography
p (index)	paramagentic
PCZ	point of zero charge
PVA	polyvingyl alcohol
PRE	paramagnetic relaxation enhancement

RI	refrective index
SBR	sequencing batch reactor
SPION	super paramagnetic iron oxide nanoparticles
TOF	time of flight experiment
w (index)	water
WWT	wastewater treatment
WWTP	wastewater treatment plant

Mathematical symbols

B_0	T	static magnetic field amplitude
B_1	T	high frequency magnetic field amplitude
c	kg/L	concentration
C	-	MSB constant
c_p	kg/L	concentration of paramagnetic compound
D	m^2/s	self diffusion coefficient
d	m	distance
d_{diff}	m	thickness of the GOUY-CHAPMAN layer
d_{ST}	m	thickness of the STERN layer
ΔE	J	energy diffrence
G	T/m	amplitude of spatial gradient
G_{ph}	T/m	frequency encoding gradient
G_r	T/m	phase encoding gradient
G_s	T/m	slice selection gradient
$\hbar$	J·s	reduced planck's constant ($6.626/2\cdot\pi\cdot10^{-34}$ J·s)
I_{MSB}	m	height in sample tube (MSB)
L	m	biofilm thickness
M	A/m	magentization
M_0	A/m	magnetization in thermal equilibrium
m_i	kg	mass of a substance *i*
$M_{x,y,z}$	A/m	components of the magnetization
N	-	number of nuclei
R	m^3/kg	reading signal sample (MSB) for mass magnetic susceptibility
r	m	position vector
R_0	m^3/kg	reading signal of empty sample tube (MSB) for mass magnetic susceptibility

r_i	L/(mg·s)	relaxivity (i = 1, 2)
T	K	temperature
t	s	time
T_1	s	longitudinal relaxation time
$T_{1\,M}$	s	relaxation time of the inner sphere bound water molecules
T_2	s	transversal relaxation time
$T_{2,\,eff}$	s	effective transversal relaxation time
T_R	s	repetition time in NMR pulse sequence
V	m^3	volume
$\dot{V}$	m^3/s	volumetric flow rate
$\bar{v}$	m/s	mean flow velocity
v_x, v_y, v_z	m/s	flow velocity in x, y, z direction
x, y, z	m	cartesian coordinates

Greek symbols

μ	$A \cdot m^2$	magnetic moment
$\overline{\mu_0}$	H/m	inductive constant (MSB)
μ_0	N/A^2	magnetic field constant
γ	1/(T·s)	gyromagnetic ratio for ^1H: 2.675×10^8 1/(T·s)
ζ	V	zeta potential
ρ	kg/m^3	density of a substance
ρ_{PD}	$moles/m^3$	spin density
τ_C	s	correlation time
τ_D	s	translational diffusion correlation time
τ_E	s	echo time in NMR pulse sequence
τ_M	s	residence time
τ_R	s	rotational correlation time
φ	°	angle of magnetization
χ_M	m^3/kg	mass magnetic susceptibility
χ_v	-	volume magnetic susceptibility
ω_0	rad/s	larmor frequency at B_0
ω_1	rad/s	angular frency at B_1
$\Delta\omega$	rad/s	line width

Formula

$y = \beta_0 + \beta_1 \cdot x$	linear fit β_0: intercept β_1: slope
$\bar{x}$; $\bar{y}$	average value, mean $\bar{x} = \frac{1}{n}\sum_{i=1}^{n} x_i$; $\bar{y} = \frac{1}{n}\sum_{i=1}^{n} y_i$
R^2	coefficient of determination

Units

A	amphere
g	gram
H	henry
J	joule
K	kelvin
m	meter
N	newton
rad	radian
s	second
T	tesla
V	volt

REFERENCES

Abragam, A. (**1989**) *Principles of Nuclear Magnetic Resonance*, Oxford Science Publications, Oxford.

Agilent-Technologies (**2010**) *Agilent 720/730 Series ICP-OES: Specifications*, Agilent Technologies, Publication number: 5990-6713EN.

Ahamed, M., AlSalhi, M.S. and Siddiqui, M.K.J. (**2010**) *Silver nanoparticle applications and human health*. Clinica Chimica Acta 411(23-24): 1841-1848.

Aime, S., Botta, M., Fasano, M. and Terreno, E. (**1998**) *Lanthanide(III) chelates for NMR biomedical applications*. Chemical Society Reviews 27(1): 19-29.

Auffan, M., Rose, J., Bottero, J.-Y., Lowry, G.V., Jolivet, J.-P. and Wiesner, M.R. (**2009**) *Towards a definition of inorganic nanoparticles from an environmental, health and safety perspective*. Nature Nanotechnology 4(10): 634-641.

Baalousha, M. (**2009**) *Aggregation and disaggregation of iron oxide nanoparticles: Influence of particle concentration, pH and natural organic matter*. Science of the Total Environment 407(6): 2093-2101.

Baalousha, M., Manciulea, A., Cumberland, S., Kendall, K. and Lead, J.R. (**2008**) *Aggregation and surface properties of iron oxide nanoparticles: Influence of ph and natural organic matter*. Environmental Toxicology and Chemistry 27(9): 1875-1882.

Bartacek, J., Vergeldt, F.J., Gerkema, E., Jenicek, P., Lens, P.N.L. and Van As, H. (**2009**) *Magnetic resonance microscopy of iron transport in methanogenic granules*. Journal of Magnetic Resonance 200(2): 303-312.

Barth, H.G. (**1984**) *Modern methods of particle size analysis*, Wiley, New York.

Battin, T.J., Kammer, F.V.D., Weilhartner, A., Ottofuelling, S. and Hofmann, T. (**2009**) *Nanostructured TiO2: Transport Behavior and Effects on Aquatic Microbial Communities under Environmental Conditions*. Environmental Science & Technology 43(21): 8098-8104.

Baumann, T. and Werth, C.J. (**2005**) *Visualization of colloid transport through heterogeneous porous media using magnetic resonance imaging*. Colloids and Surfaces a-Physicochemical and Engineering Aspects 265(1-3): 2-10.

Beauregard, D.A., Yong, P., Macaskie, L.E. and Johns, M.L. (**2010**) *Using Non-Invasive Magnetic Resonance Imaging (MRI) to Assess the Reduction of Cr(VI) Using a Biofilm-Palladium Catalyst*. Biotechnology and Bioengineering 107(1): 11-20.

Benn, T.M. and Westerhoff, P. (**2008**) *Nanoparticle silver released into water from commercially available sock fabrics*. Environmental Science & Technology 42(11): 4133-4139.

Bertini, I., Luchinat, G. and Parigi, G. (**2001**) *Solution NMR of paramagnetic molecules: Applications to metallobiomolecules and models*, Elsevier Science, Amsterdam.

Blaser, S.A., Scheringer, M., MacLeod, M. and Hungerbuehler, K. (**2008**) *Estimation of cumulative aquatic exposure and risk due to silver: Contribution of nano-functionalized plastics and textiles*. Science of the Total Environment 390(2-3): 396-409.

Blauert, F., Horn, H. and Wagner, M. (**2015**) *Time-resolved biofilm deformation measurements using optical coherence tomography*. Biotechnology and Bioengineering 112(9): 1893-1905.

Bloembergen, N. (**1957**) *Proton relaxtion times in paramagnetic solutions*. Journal of Chemical Physics 27(2): 572-573.

Boltz, J.P. and Daigger, G.T. (**2010**) *Uncertainty in bulk-liquid hydrodynamics and biofilm dynamics creates uncertainties in biofilm reactor design*. Water Science and Technology 61(2): 307-316.

Borradaile, G.J. and Henry, B. (**1997**) *Tectonic applications of magnetic susceptibility and its anisotropy*. Earth-Science Reviews 42(1-2): 49-93.

Bottrill, M., Nicholas, L.K. and Long, N.J. (**2006**) *Lanthanides in magnetic resonance imaging*. Chemical Society Reviews 35(6): 557-571.

Brar, S.K., Verma, M., Tyagi, R.D. and Surampalli, R.Y. (**2010**) *Engineered nanoparticles in wastewater and wastewater sludge - Evidence and impacts*. Waste Management 30(3): 504-520.

Brownstein, K.R. and Tarr, C.E. (**1979**) *Importance of classical diffusion NMR-studies of water in biological cells*. Physical Review A 19(6): 2446-2453.

Buzea, C., Pacheco, I.I. and Robbie, K. (**2007**) *Nanomaterials and nanoparticles: Sources and toxicity*. Biointerphases 2(4): MR17-MR71.

Callaghan, P. (**1991**) *Principles of Nuclear Magnetic Resonance Microscopy*, Oxford University Press.

Callaghan, P.T. (**1991 / 1993**) *Principles of Nuclear Magnetic Resonance Microscopy*, Oxford University Press, New York.

Callaghan, P.T. and Xia, Y. (**1991**) *Velocity and Diffusion Imaging in dynamic NMR Microscopy*. Journal of Magnetic Resonance 91(2): 326-352.

Caravan, P., Ellison, J.J., McMurry, T.J. and Lauffer, R.B. (**1999**) *Gadolinium(III) chelates as MRI contrast agents: Structure, dynamics, and applications*. Chemical Reviews 99(9): 2293-2352.

Chan, K.W.Y. and Wong, W.T. (**2007**) *Small molecular gadolinium(III) complexes as MRI contrast agents for diagnostic imaging*. Coordination Chemistry Reviews 251(17-20): 2428-2451.

Christensson, M. and Welander, T. (**2004**) *Treatment of municipal wastewater in a hybrid process using a new suspended carrier with large surface area*. Water Science and Technology 49(11-12): 207-214.

Christian, P., Von der Kammer, F., Baalousha, M. and Hofmann, T. (**2008**) *Nanoparticles: structure, properties, preparation and behaviour in environmental media*. Ecotoxicology 17(5): 326-343.

Clark, K., van Tongeren, M., Christensen, F.M., Brouwer, D., Nowack, B., Gottschalk, F., Micheletti, C., Schmid, K., Gerritsen, R., Aitken, R., Vaquero, C., Gkanis, V., Housiadas, C., Lopez de Ipina, J.M. and Riediker, M. (**2012**) *Limitations and information needs for engineered nanomaterial-specific exposure estimation and scenarios: recommendations for improved reporting practices*. Journal of Nanoparticle Research 14(9).

Codd, S.L., Vogt, S.J., Hornemann, J.A., Phillips, A.J., Maneval, J.E., Romanenko, K.R., Hansen, L., Cunningham, A.B. and Seymour, J.D. (**2011**) *NMR relaxation measurements of biofouling in model and geological porous media*. Organic Geochemistry 42(8): 965-971.

Costerton, J.W. (**1999**) *Introduction to biofilm*. International Journal of Antimicrobial Agents 11(3-4): 217-221.

Costerton, J.W., Lewandowski, Z., Caldwell, D.E., Korber, D.R. and Lappinscott, H.M. (**1995**) *Microbial Biofilms*. Annual Review of Microbiology 49: 711-745.

Costerton, J.W., Lewandowski, Z., Debeer, D., Caldwell, D., Korber, D. and James, G. (**1994**) *Biofilms, the customized microniche*. Journal of Bacteriology 176(8): 2137-2142.

Costerton, J.W., Montanaro, L. and Arciola, C.R. (**2005**) *Biofilm in implant infections: Its production and regulation*. International Journal of Artificial Organs 28(11): 1062-1068.

Creber, S.A., Pintelon, T.R.R., von der Schulenburg, D.A.W.G., Vrouwenvelder, J.S., van Loosdrecht, M.C.M. and Johns, M.L. (**2010**) *Magnetic resonance imaging and 3D simulation studies of biofilm accumulation and cleaning on reverse osmosis membranes*. Food and Bioproducts Processing 88(C4): 401-408.

Cuny, L., Herrling, M.P., Guthausen, G., Horn, H. and Delay, M. (**2015**) *Magnetic resonance imaging reveals detailed spatial and temporal distribution of iron-based nanoparticles transported through water-saturated porous media*. Journal of Contaminant Hydrology 182: 51-62.

Dalitz, F., Maiwald, M. and Guthausen, G. (**2012**) *Considerations on the design of flow cells in by-pass systems for process analytical applications and its influence on the flow profile using NMR and CFD*. Chemical Engineering Science 75: 318-326.

De Beer, D., Stoodley, P. and Lewandowski, Z. (**1994a**) *Liquid flow in heterogenous biofilms*. Biotechnology and Bioengineering 44(5): 636-641.

De Beer, D., Stoodley, P. and Lewandowski, Z. (**1996**) *Liquid flow and mass transport in heterogeneous biofilms*. Water Research 30(11): 2761-2765.

De Beer, D., Stoodley, P., Roe, F. and Lewandowski, Z. (**1994b**) *Effects of biofilm structures on oxygen distribution and mass-transport*. Biotechnology and Bioengineering 43(11): 1131-1138.

de Kreuk, M.K., Kishida, N. and van Loosdrecht, M.C.M. (**2007**) *Aerobic granular sludge - state of the art*. Water Science and Technology 55(8-9): 75-81.

Delay, M., Dolt, T., Woellhaf, A., Sembritzki, R. and Frimmel, F.H. (**2011**) *Interactions and stability of silver nanoparticles in the aqueous phase: Influence of natural organic matter (NOM) and ionic strength*. Journal of Chromatography A 1218(27): 4206-4212.

Delay, M. and Frimmel, F.H. (**2012**) *Nanoparticles in aquatic systems*. Analytical and Bioanalytical Chemistry 402(2): 583-592.

Derjaguin, B. and Landau, L. (**1941**) *Theory of the stability of strongly charged lyophobic sols and of the adhesion of strongly charged particles in solutions of electrolytes.* Acta Physicochim URSS 14: 733–762.

DIN-EN-12880 (**February 2001**) *Characterization of sludges – Determination of dry residue and water content*, Deutsches Institut für Normung e.V. (DIN).

Earnshaw, A. (**1968**) *Introduction to magnetochemistry*, Acad. Pr. London, London.

Elimelech, M., Gregory, J., Jia, X. and Williams, R.A. (**1995**) *Particle deposition and aggregation : measurement, modelling and simulation*, Mass. : Butterworth-Heinemann, Woburn.

Fabrega, J., Fawcett, S.R., Renshaw, J.C. and Lead, J.R. (**2009a**) *Silver Nanoparticle Impact on Bacterial Growth: Effect of pH, Concentration, and Organic Matter*. Environmental Science & Technology 43(19): 7285-7290.

Fabrega, J., Renshaw, J.C. and Lead, J.R. (**2009b**) *Interactions of Silver Nanoparticles with Pseudomonas putida Biofilms*. Environmental Science & Technology 43(23): 9004-9009.

Fabrega, J., Zhang, R., Renshaw, J.C., Liu, W.-T. and Lead, J.R. (**2011**) *Impact of silver nanoparticles on natural marine biofilm bacteria*. Chemosphere 85(6): 961-966.

Farré, M. and Barceló, D. (**2012**) *Introduction to the analysis and risk of nanomaterials in environmental and food samples*, Elsevier, Amsterdam.

Flemming, H.-C. and Wingender, J. (**2010**) *The biofilm matrix*. Nature Reviews Microbiology 8(9): 623-633.

Flemming, H.C. and Wingender, J. (**2001**) *Relevance of microbial extracellular polymeric substances (EPSs) - Part I: Structural and ecological aspects*. Water Science and Technology 43(6): 1-8.

Flemming, H.C. and Wingender, J. (**2002**) *What biofilms contain - Proteins, polysaccharides, etc*. Chemie in Unserer Zeit 36(1): 30-42.

Freed, J.H. (**1978**) *Dynamic effects of pair correlation-functions on spin relaxation by translational diffusion in liquds. 2. Finite jumps and independ T1 process*. Journal of Chemical Physics 68(9): 4034-4037.

Fukushima, E. (**1999**) *Nuclear magnetic resonance as a tool to study flow*. Annual Review of Fluid Mechanics 31: 95-123.

Ganesh, R., Smeraldi, J., Hosseini, T., Khatib, L., Olson, B.H. and Rosso, D. (**2010**) *Evaluation of Nanocopper Removal and Toxicity in Municipal Wastewaters*. Environmental Science & Technology 44(20): 7808-7813.

Gartiser, S., Flach, F., Nickel, C., Stintz, M., Damme, S., Schaeffer, A., Erdinger, L. and Kuhlbusch, T.A.J. (**2014**) *Behavior of nanoscale titanium dioxide in laboratory wastewater treatment plants according to OECD 303 A*. Chemosphere 104: 197-204.

Gatehouse, P.D., Keegan, J., Crowe, L.A., Masood, S., Mohiaddin, R.H., Kreitner, K.F. and Firmin, D.N. (**2005**) *Applications of phase-contrast flow and velocity imaging in cardiovascular MRI*. European Radiology 15(10): 2172-2184.

Gjersing, E.L., Codd, S.L., Seymour, J.D. and Stewart, P.S. (**2005**) *Magnetic resonance microscopy analysis of advective transport in a biofilm reactor*. Biotechnology and Bioengineering 89(7): 822-834.

Gomez-Rivera, F., Field, J.A., Brown, D. and Sierra-Alvarez, R. (**2012**) *Fate of cerium dioxide (CeO2) nanoparticles in municipal wastewater during activated sludge treatment*. Bioresource Technology 108: 300-304.

Gorbushina, A.A. (**2007**) *Life on the rocks*. Environmental Microbiology 9(7): 1613-1631.

Gottschalk, F., Kost, E. and Nowack, B. (**2013a**) *Engineered nanomaterials in water and soils: A risk quantification based on probabilistic exposure and effect modeling*. Environmental Toxicology and Chemistry 32(6): 1278-1287.

Gottschalk, F. and Nowack, B. (**2011**) *The release of engineered nanomaterials to the environment*. Journal of Environmental Monitoring 13(5): 1145-1155.

Gottschalk, F., Sonderer, T., Scholz, R.W. and Nowack, B. (**2009**) *Modeled Environmental Concentrations of Engineered Nanomaterials (TiO2, ZnO, Ag, CNT, Fullerenes) for Different Regions*. Environmental Science & Technology 43(24): 9216-9222.

Gottschalk, F., Sun, T.Y. and Nowack, B. (**2013b**) *Environmental concentrations of engineered nanomaterials: Review of modeling and analytical studies*. Environmental Pollution 181: 287-300.

Gu, L., Li, Q., Quan, X., Cen, Y. and Jiang, X. (**2014**) *Comparison of nanosilver removal by flocculent and granular sludge and short- and long-term inhibition impacts*. Water Research 58: 62-70.

Gupta, A.K. and Gupta, M. (**2005**) *Synthesis and surface engineering of iron oxide nanoparticles for biomedical applications*. Biomaterials 26(18): 3995-4021.

Guthausen, G., Machado, J.R., Luy, B., Baniodeh, A., Powell, A.K., Kramer, S., Ranzinger, F., Herrling, M.P., Lackner, S. and Horn, H. (**2015**) *Characterisation and application of ultra-high spin clusters as magnetic resonance relaxation agents*. Dalton Transactions 44(11): 5032-5040.

Hall-Stoodley, L. and Stoodley, P. (**2009**) *Evolving concepts in biofilm infections*. Cellular Microbiology 11(7): 1034-1043.

Hanesch, M. and Scholger, R. (**2002**) *Mapping of heavy metal loadings in soils by means of magnetic susceptibility measurements*. Environmental Geology 42(8): 857-870.

Heiligtag, F.J. and Niederberger, M. (**2013**) *The fascinating world of nanoparticle research*. Materials Today 16(7–8): 262-271.

Henze, M. (**2002**) *Wastewater treatment : biological and chemical processes*, Springer Verlag, Berlin.

Herrling, M.P., Fetsch, K.L., Delay, M., Blauert, F., Wagner, M., Franzreb, M., Horn, H. and Lackner, S. (**2015a**) *Low biosorption of PVA coated engineered magnetic nanoparticles in granular sludge assessed by magnetic susceptibility*. Science of the Total Environment 537: 43-50.

Herrling, M.P., Guthausen, G., Wagner, M., Lackner, S. and Horn, H. (**2015b**) *Determining the flow regime in a biofilm carrier by means of magnetic resonance imaging*. Biotechnology and Bioengineering 112(5): 1023-1032.

Horn, H. (**2004**) *Substrate Conversion and Mass Transport in Biofilm Systems: Experiment and Modelling*, FIT-Verlag für Innovation und Technologietransfer, Paderborn.

Horn, H. and Lackner, S. (**2014**) Productive Biofilms. Muffler, K. and Ulber, R. (eds), pp. 53-76, Springer-Verlag Berlin, Berlin.

Hornemann, J.A., Codd, S.L., Fell, R.J., Stewart, P.S. and Seymour, J.D. (**2009**) *Secondary Flow Mixing Due to Biofilm Growth in Capillaries of Varying Dimensions*. Biotechnology and Bioengineering 103(2): 353-360.

Hoskins, B.C., Fevang, L., Majors, P.D., Sharma, M.M. and Georgiou, G. (**1999**) *Selective imaging of biofilms in porous media by NMR relaxation*. Journal of Magnetic Resonance 139(1): 67-73.

Hou, J., Miao, L.Z., Wang, C., Wang, P.F., Ao, Y.H., Qian, J. and Dai, S.S. (**2014**) *Inhibitory effects of ZnO nanoparticles on aerobic wastewater biofilms from oxygen concentration profiles determined by microelectrodes*. Journal of Hazardous Materials 276: 164-170.

Hou, J., You, G., Xu, Y., Wang, C., Wang, P., Miao, L., Ao, Y., Li, Y. and Lv, B. (**2015**) *Effects of CeO2 nanoparticles on biological nitrogen removal in a sequencing batch biofilm reactor and mechanism of toxicity*. Bioresource Technology 191: 73-78.

Hou, L.L., Xia, J., Li, K.Y., Chen, J., Wu, X.L. and Li, X.Q. (**2013**) *Removal of ZnO nanoparticles in simulated wastewater treatment processes and its effects on COD and NH4+-N reduction*. Water Science and Technology 67(2): 254-260.

Hu, J., Chen, G.H. and Lo, I.M.C. (**2006**) *Selective removal of heavy metals from industrial wastewater using maghemite nanoparticle: Performance and mechanisms*. Journal of Environmental Engineering-Asce 132(7): 709-715.

Ikuma, K., Decho, A.W. and Lau, B.L.T. (**2015**) *When nanoparticles meet biofilms-interactions guiding the environmental fate and accumulation of nanoparticles*. Frontiers in Microbiology 6(591).

Ikuma, K., Madden, A.S., Decho, A.W. and Lau, B.L.T. (**2014**) *Deposition of nanoparticles onto polysaccharide-coated surfaces: implications for nanoparticle-biofilm interactions*. Environmental Science-Nano 1(2): 117-122.

ISO (**2008**) *Nanotechnologies –Terminology and definitions for nano-objects – Nanoparticle, nanofibre and nanoplate (ISO/TS 27687:2008),* International Organization for Standardization (ISO) and Deutsches Institut für Normung e.V. (DIN).

Israelachvili, J. (**2010**) *Intermolecular and Surface Forces*, Elsevier Academic Press, Amsterdam.

Ito, A., Shinkai, M., Honda, H. and Kobayashi, T. (**2005**) *Medical application of functionalized magnetic nanoparticles*. Journal of Bioscience and Bioengineering 100(1): 1-11.

Jiang, J., Oberdorster, G. and Biswas, P. (**2009**) *Characterization of size, surface charge, and agglomeration state of nanoparticle dispersions for toxicological studies*. Journal of Nanoparticle Research 11(1): 77-89.

Jing, H., Mezgebe, B., Hassan, A.A., Sahle-Demessie, E., Sorial, G.A. and Bennett-Stamper, C. (**2014**) *Experimental and modeling studies of sorption of ceria nanoparticle on microbial biofilms*. Bioresource Technology 161: 109-117.

Jones, M.N. and Bryan, N.D. (**1998**) *Colloidal properties of humic substances*. Advances in Colloid and Interface Science 78(1): 1-48.

Kaegi, R., Voegelin, A., Ort, C., Sinnet, B., Thalmann, B., Krismer, J., Hagendorfer, H., Elumelu, M. and Mueller, E. (**2013**) *Fate and transformation of silver nanoparticles in urban wastewater systems*. Water Research 47(12): 3866-3877.

Kaegi, R., Voegelin, A., Sinnet, B., Zuleeg, S., Hagendorfer, H., Burkhardt, M. and Siegrist, H. (**2011**) *Behavior of Metallic Silver Nanoparticles in a Pilot Wastewater Treatment Plant*. Environmental Science & Technology 45(9): 3902-3908.

Kallmeyer, J., Pockalny, R., Adhikari, R.R., Smith, D.C. and D'Hondt, S. (**2012**) *Global distribution of microbial abundance and biomass in subseafloor sediment*. Proceedings of the National Academy of Sciences of the United States of America 109(40): 16213-16216.

Kang, Y., Zhou, L.L., Li, X. and Yuan, J.Y. (**2011**) *beta-Cyclodextrin-modified hybrid magnetic nanoparticles for catalysis and adsorption*. Journal of Materials Chemistry 21(11): 3704-3710.

Keller, A.A., Wang, H.T., Zhou, D.X., Lenihan, H.S., Cherr, G., Cardinale, B.J., Miller, R. and Ji, Z.X. (**2010**) *Stability and Aggregation of Metal Oxide Nanoparticles in Natural Aqueous Matrices*. Environmental Science & Technology 44(6): 1962-1967.

Kim, B., Park, C.S., Murayama, M. and Hochella, M.F. (**2010**) *Discovery and Characterization of Silver Sulfide Nanoparticles in Final Sewage Sludge Products*. Environmental Science & Technology 44(19): 7509-7514.

Kim, J.S., Kuk, E., Yu, K.N., Kim, J.H., Park, S.J., Lee, H.J., Kim, S.H., Park, Y.K., Park, Y.H., Hwang, C.Y., Kim, Y.K., Lee, Y.S., Jeong, D.H. and Cho, M.H. (**2014**) *Antimicrobial effects of silver nanoparticles* Nanomedicine-Nanotechnology Biology and Medicine 10(5): 1119-1119.

Kimmich, R. (**1997**) *NMR - Tomography, Diffusometry, Relaxometry*. Springer Verlag.

Kirkland, C.M., Herrling, M.P., Hiebert, R., Bender, A.T., Grunewald, E., Walsh, D.O. and Codd, S.L. (**2015a**) *In-situ detection of subsurface biofilm using low-field NMR-a field study*. Environmental Science & Technology doi: 10.1021/acs.est.5b02690.

Kirkland, C.M., Hiebert, R., Phillips, A., Grunewald, E., Walsh, D.O., Seymour, J.D. and Codd, S.L. (**2015b**) *Biofilm Detection in a Model Well-Bore Environment Using Low-Field NMR*. Groundwater Monitoring & Remediation: doi: 10.1111/gwmr.12117.

Kiser, M.A., Ryu, H., Jang, H.Y., Hristovski, K. and Westerhoff, P. (**2010**) *Biosorption of nanoparticles to heterotrophic wastewater biomass*. Water Research 44(14): 4105-4114.

Kiser, M.A., Westerhoff, P., Benn, T., Wang, Y., Perez-Rivera, J. and Hristovski, K. (**2009**) *Titanium Nanomaterial Removal and Release from Wastewater Treatment Plants*. Environmental Science & Technology 43(17): 6757-6763.

Klaine, S.J., Alvarez, P.J.J., Batley, G.E., Fernandes, T.F., Handy, R.D., Lyon, D.Y., Mahendra, S., McLaughlin, M.J. and Lead, J.R. (**2008**) *Nanomaterials in the environment: Behavior, fate, bioavailability, and effects*. Environmental Toxicology and Chemistry 27(9): 1825-1851.

Kloepfer, J.A., Mielke, R.E. and Nadeau, J.L. (**2005**) *Uptake of CdSe and CdSe/ZnS quantum dots into bacteria via purine-dependent mechanisms*. Applied and Environmental Microbiology 71(5): 2548-2557.

Kroll, A., Behra, R., Kaegi, R. and Sigg, L. (**2014**) *Extracellular Polymeric Substances (EPS) of Freshwater Biofilms Stabilize and Modify CeO2 and Ag Nanoparticles*. Plos One 9(10): 16.

Kruk, D., Kowalewski, J. and Westlund, P.O. (**2004**) *Nuclear and electron spin relaxation in paramagnetic complexes in solution: Effects of the quantum nature of molecular vibrations*. Journal of Chemical Physics 121(5): 2215-2227.

Lakshmanan, S., Holmes, W.M., Sloan, W.T. and Phoenix, V.R. (**2015**) *Nanoparticle transport in saturated porous medium using magnetic resonance imaging*. Chemical Engineering Journal 266: 156-162.

Landolt, H. and Börnstein, R. (**1986**) *Numerical Data and Functional Relationships in Science and Technology*, Springer-Verlag, Heidelberg.

Lauffer, R.B. (**1987**) *Paramagnetic metal-complexes as water proton relaxation agents for NMR imaging - theory and design*. Chemical Reviews 87(5): 901-927.

Laurent, S., Forge, D., Port, M., Roch, A., Robic, C., Elst, L.V. and Muller, R.N. (**2008**) *Magnetic iron oxide nanoparticles: Synthesis, stabilization, vectorization, physicochemical characterizations, and biological applications*. Chemical Reviews 108(6): 2064-2110.

Laurent, S., Vander Elst, L., Roch, A. and Muller, R.N. (**2007**) NMR-MRI, μSR and Mössbauer Spectroscopies in Molecular Magnets, pp. 71-87, Springer, Milan.

Lauterbur, P.C. (**1973**) *Image formation by induced local interactions - examples employing nuclear magnetic resonance*. Nature 242(5394): 190-191.

Lazarova, V. and Manem, J. (**1995**) *Biofilm characterization and activity analysis in water and wastewater treatment*. Water Research 29(10): 2227-2245.

Lens, P., Pol, L.H., Lettinga, G. and Van As, H. (**1997**) *Use of H-1 NMR to study transport processes in sulfidogenic granular sludge*. Water Science and Technology 36(6-7): 157-163.

Lewandowski, Z., Altobelli, S.A. and Fukushima, E. (**1993**) *NMR and mircoeletrode studies of hydrodynamics and kinetics in biofilms*. Biotechnology Progress 9(1): 40-45.

Lewandowski, Z. and Beyenal, H. (**2013**) *Fundamentals of Biofilm Research*, Crc Pr Inc, Boca Raton.

Li, C., Felz, S., Wagner, M., Lackner, S. and Horn, H. (**2016**) *Investigating biofilm structure developing on carriers from lab-scale moving bed biofilm reactors based on light microscopy and optical coherence tomography*. Bioresource Technology 200: 128-136.

Li, C., Wagner, M., Lackner, S. and Horn, H. (**2015**) *Assessing the influence of biofilm surface roughness on mass transfer by combining optical coherence tomography and two-dimensional modeling*. Biotechnology and Bioengineering: doi: 10.1002/bit.25868.

Li, M., Lin, D. and Zhu, L. (**2013**) *Effects of water chemistry on the dissolution of ZnO nanoparticles and their toxicity to Escherichia coli*. Environmental Pollution 173(0): 97-102.

Limbach, L.K., Bereiter, R., Mueller, E., Krebs, R., Gaelli, R. and Stark, W.J. (**2008**) *Removal of oxide nanoparticles in a model wastewater treatment plant: Influence of agglomeration and surfactants on clearing efficiency*. Environmental Science & Technology 42(15): 5828-5833.

Lowry, G.V., Gregory, K.B., Apte, S.C. and Lead, J.R. (**2012**) *Transformations of Nanomaterials in the Environment*. Environmental Science & Technology 46(13): 6893-6899.

Lowry, G.V., Hotze, E.M., Bernhardt, E.S., Dionysiou, D.D., Pedersen, J.A., Wiesner, M.R. and Xing, B. (**2010**) *Environmental Occurrences, Behavior, Fate, and Ecological Effects of Nanomaterials: An Introduction to the Special Series*. Journal of Environmental Quality 39(6): 1867-1874.

Lu, A.H., Salabas, E.L. and Schuth, F. (**2007**) *Magnetic nanoparticles: Synthesis, protection, functionalization, and application*. Angewandte Chemie-International Edition 46(8): 1222-1244.

Ma, J.Y., Quan, X.C., Si, X.R. and Wu, Y.C. (**2013**) *Responses of anaerobic granule and flocculent sludge to ceria nanoparticles and toxic mechanisms*. Bioresource Technology 149: 346-352.

Machado, J.R., Baniodeh, A., Powell, A.K., Luy, B., Kramer, S. and Guthausen, G. (**2014**) *Nuclear Magnetic Resonance Relaxivities: Investigations of Ultrahigh-Spin Lanthanide Clusters from 10 MHz to 1.4 GHz*. Chemphyschem : a European journal of chemical physics and physical chemistry 15(16): 3608-3613.

Mahmoudi, M., Sant, S., Wang, B., Laurent, S. and Sen, T. (**2011a**) *Superparamagnetic iron oxide nanoparticles (SPIONs): Development, surface modification and applications in chemotherapy*. Advanced Drug Delivery Reviews 63(1-2): 24-46.

Mahmoudi, M., Serpooshan, V. and Laurent, S. (**2011b**) *Engineered nanoparticles for biomolecular imaging*. Nanoscale 3(8): 3007-3026.

Mahmoudi, M., Simchi, A., Milani, A.S. and Stroeve, P. (**2009**) *Cell toxicity of superparamagnetic iron oxide nanoparticles*. Journal of Colloid and Interface Science 336(2): 510-518.

Mai-Prochnow, A., Evans, F., Dalisay-Saludes, D., Stelzer, S., Egan, S., James, S., Webb, J.S. and Kjelleberg, S. (**2004**) *Biofilm development and cell death in the marine bacterium Pseudoalteromonas tunicata*. Applied and Environmental Microbiology 70(6): 3232-3238.

Manz, B., Volke, F., Goll, D. and Horn, H. (**2003**) *Measuring local flow velocities and biofilm structure in biofilm systems with magnetic resonance imaging (MRI)*. Biotechnology and Bioengineering 84(4): 424-432.

Manz, B., Volke, F., Goll, D. and Horn, H. (**2005**) *Investigation of biofilm structure, flow patterns and detachment with magnetic resonance imaging*. Water Science and Technology 52(7): 1-6.

Masciangioli, T. and Zhang, W.X. (**2003**) *Environmental technologies at the nanoscale*. Environmental Science & Technology 37(5): 102a-108a.

Masic, A., Bengtsson, J. and Christensson, M. (**2010**) *Measuring and modeling the oxygen profile in a nitrifying Moving Bed Biofilm Reactor*. Mathematical Biosciences 227(1): 1-11.

Maynard, A.D. (**2006**) *Nanotechnology: A Research Strategy for Addressing Risk*, Washington, DC.

McQuarrie, J.P. and Boltz, J.P. (**2011**) *Moving Bed Biofilm Reactor Technology: Process Applications, Design, and Performance*. Water Environment Research 83(6): 560-575.

Metzger, U., Lankes, U., Hardy, E.H., Gordalla, B.C. and Frimmel, F.H. (**2006**) *Monitoring the formation of an Aureobasidium pullulans biofilm in a bead-packed reactor via flow-weighted magnetic resonance imaging*. Biotechnology Letters 28(16): 1305-1311.

Mihai, L., Adrian, N., B., M. and Claudiu, B. (**2015**) *Nanoparticles' Promises and Risks : Characterization, Manipulation, and Potential Hazards to Humanity and the Environment*, Springer, Cham.

Monopoli, M.P., Aberg, C., Salvati, A. and Dawson, K.A. (**2012**) *Biomolecular coronas provide the biological identity of nanosized materials*. Nature Nanotechnology 7(12): 779-786.

Morgenroth, E. and Milferstedt, K. (**2009**) *Biofilm engineering: linking biofilm development at different length and time scales*. Reviews in Environmental Science and Bio/Technology 8(3): 203-208.

Morrow, J.B., Arango P, C. and Holbrook, R.D. (**2010**) *Association of Quantum Dot Nanoparticles with Pseudomonas aeruginosa Biofilm*. Journal of Environmental Quality 39(6): 1934-1941.

Mu, H., Zheng, X., Chen, Y.G., Chen, H. and Liu, K. (**2012**) *Response of Anaerobic Granular Sludge to a Shock Load of Zinc Oxide Nanoparticles during Biological Wastewater Treatment*. Environmental Science & Technology 46(11): 5997-6003.

Mueller, N.C. and Nowack, B. (**2008**) *Exposure modeling of engineered nanoparticles in the environment*. Environmental Science & Technology 42(12): 4447-4453.

Mueller, N.C. and Nowack, B. (**2010**) *Nanoparticles for Remediation: Solving Big Problems with Little Particles*. Elements 6(6): 395-400.

Napper, D.H. (**1977**) *Steric stabilizazion*. Journal of Colloid and Interface Science 58(2): 390-407.

Navarro, E., Baun, A., Behra, R., Hartmann, N.B., Filser, J., Miao, A.-J., Quigg, A., Santschi, P.H. and Sigg, L. (**2008a**) *Environmental behavior and ecotoxicity of engineered nanoparticles to algae, plants, and fungi*. Ecotoxicology 17(5): 372-386.

Navarro, E., Piccapietra, F., Wagner, B., Marconi, F., Kaegi, R., Odzak, N., Sigg, L. and Behra, R. (**2008b**) *Toxicity of Silver Nanoparticles to Chlamydomonas reinhardtii*. Environmental Science & Technology 42(23): 8959-8964.

Nel, A.E., Maedler, L., Velegol, D., Xia, T., Hoek, E.M.V., Somasundaran, P., Klaessig, F., Castranova, V. and Thompson, M. (**2009**) *Understanding biophysicochemical interactions at the nano-bio interface*. Nature Materials 8(7): 543-557.

Nestle, N. and Kimmich, R. (**1996**) *NMR imaging of heavy metal absorption in alginate, immobilized cells, and kombu algal biosorbents*. Biotechnology and Bioengineering 51(5): 538-543.

Neu, T.R., Manz, B., Volke, F., Dynes, J.J., Hitchcock, A.P. and Lawrence, J.R. (**2010**) *Advanced imaging techniques for assessment of structure, composition and function in biofilm systems*. Fems Microbiology Ecology 72(1): 1-21.

Nevius, B.A., Chen, Y.P., Ferry, J.L. and Decho, A.W. (**2012**) *Surface-functionalization effects on uptake of fluorescent polystyrene nanoparticles by model biofilms*. Ecotoxicology 21(8): 2205-2213.

Nott, K.P., Heese, F.P., Hall, L.D., Macaskie, L.E. and Paterson-Beedle, M. (**2005a**) *Measurement of flow field in biofilm reactors by 3-D magnetic resonance imaging*. Aiche Journal 51(11): 3072-3079.

Nott, K.P., Heese, F.P., Paterson-Beedle, M., Macaskie, L.E. and Hall, L.D. (**2005b**) *Visualization of the function of a biofilm reactor by magnetic resonance imaging*. Canadian Journal of Chemical Engineering 83(1): 68-72.

Nott, K.P., Paterson-Beedle, M., Macaskie, L.E. and Hall, L.D. (**2001**) *Visualisation of metal deposition in biofilm reactors by three-dimensional magnetic resonance imaging (MRI)*. Biotechnology Letters 23(21): 1749-1757.

Nowack, B. (**2009**) *Is anything out there? What life cycle perspectives of nano-products can tell us about nanoparticles in the environment*. Nano Today 4(1): 11-12.

Nowack, B. and Bucheli, T.D. (**2007**) *Occurrence, behavior and effects of nanoparticles in the environment*. Environmental Pollution 150(1): 5-22.

Nowack, B., Ranville, J.F., Diamond, S., Gallego-Urrea, J.A., Metcalfe, C., Rose, J., Horne, N., Koelmans, A.A. and Klaine, S.J. (**2012**) *Potential scenarios for nanomaterial release and subsequent alteration in the environment*. Environmental Toxicology and Chemistry 31(1): 50-59.

Odegaard, H. (**2006**) *Innovations in wastewater treatment: the moving bed biofilm process*. Water Science and Technology 53(9): 17-33.

Odegaard, H., Gisvold, B. and Strickland, J. (**2000**) *The influence of carrier size and shape in the moving bed biofilm process*. Water Science and Technology 41(4-5): 383-391.

Odegaard, H., Rusten, B. and Westrum, T. (**1994**) *A New Moving-Bed Biofilm Reactor - Applications and Results*. Water Science and Technology 29(10-11): 157-165.

OECD (**03. July 2015**) *Analysis of the survey on the available methods and models for assessing the exposure to manufactured nanomaterials (ENV/JM/MONO(2015)20)*, Organisation for Economic Cooperation and Development (OECD).

OECD (**2015**) *Testing Programme of Manufactured Nanomaterials - Dossiers and Endpoints*, Organisation for Economic Cooperation and Development (OECD), http://www.oecd.org/chemicalsafety/nanosafety/dossiers-and-endpoints-testing-programme-manufactured-nanomaterials.htm, 04.09.2015, 21:41 pm.

Orchard, A.F. (**2007**) *Magnetochemistry*, Oxford University Press, Oxford.

Otero-Gonzalez, L., Field, J.A., Calderon, I.A.C., Aspinwall, C.A., Shadman, F., Zeng, C. and Sierra-Alvarez, R. (**2015**) *Fate of fluorescent core-shell silica nanoparticles during simulated secondary wastewater treatment*. Water Research 77: 170-178.

Otero-Gonzalez, L., Field, J.A. and Sierra-Alvarez, R. (**2014**) *Inhibition of anaerobic wastewater treatment after long-term exposure to low levels of CuO nanoparticles*. Water Research 58: 160-168.

Ottofuelling, S.V.d.K., Frank; Hofmann, Thilo (**2011**) *Commercial Titanium Dioxide Nanoparticles in both Natural and Synthetic Water: Comprehensive Multidimensional Testing and Prediction of Aggregation Behavior*. Environmental Science & Technology 45(10): 10045–10052.

Park, H.J., Kim, H.Y., Cha, S., Ahn, C.H., Roh, J., Park, S., Kim, S., Choi, K., Yi, J., Kim, Y. and Yoon, J. (**2013**) *Removal characteristics of engineered nanoparticles by activated sludge*. Chemosphere 92(5): 524-528.

Pelley, A.J. and Tufenkji, N. (**2008**) *Effect of particle size and natural organic matter on the migration of nano- and microscale latex particles in saturated porous media*. Journal of Colloid and Interface Science 321(1): 74-83.

Petosa, A.R., Jaisi, D.P., Quevedo, I.R., Elimelech, M. and Tufenkji, N. (**2010**) *Aggregation and Deposition of Engineered Nanomaterials in Aquatic Environments: Role of Physicochemical Interactions*. Environmental Science & Technology 44(17): 6532-6549.

Peulen, T.O. and Wilkinson, K.J. (**2011**) *Diffusion of Nanoparticles in a Biofilm*. Environmental Science & Technology 45(8): 3367-3373.

Phoenix, V.R. and Holmes, W.M. (**2008**) *Magnetic resonance imaging of structure, diffusivity, and copper immobilization in a phototrophic biofilm*. Applied and Environmental Microbiology 74(15): 4934-4943.

Phoenix, V.R., Holmes, W.M. and Ramanan, B. (**2008**) *Magnetic resonance imaging (MRI) of heavy-metal transport and fate in an artificial biofilm*. Mineralogical Magazine 72(1): 483-486.

Phoenix, V.R., Ramanan, B., Sloan, W.T. and Holmes, W.M. (**2009**) *Imaging biogeochemical processes with MRI: Application of paramagetic tracers*. Geochimica Et Cosmochimica Acta 73(13): A1026-A1026.

Pintelon, T.R.R., Picioreanu, C., van Loosdrecht, M.C.M. and Johns, M.L. (**2012**) *The effect of biofilm permeability on bio-clogging of porous media*. Biotechnology and Bioengineering 109(4): 1031-1042.

Quik, J.T.K., Vonk, J.A., Hansen, S.F., Baun, A. and Van De Meent, D. (**2011**) *How to assess exposure of aquatic organisms to manufactured nanoparticles?* Environment International 37(6): 1068-1077.

Ramanan, B., Holmes, W.M., Sloan, W.T. and Phoenix, V.R. (**2013**) *Magnetic Resonance Imaging of Mass Transport and Structure Inside a Phototrophic Biofilm*. Current Microbiology 66(5): 456-461.

Rottman, J., Shadman, F. and Sierra-Alvarez, R. (**2012**) *Interactions of inorganic oxide nanoparticles with sewage biosolids*. Water Science and Technology 66(9): 1821-1827.

Rusten, B., Eikebrokk, B., Ulgenes, Y. and Lygren, E. (**2006**) *Design and operations of the Kaldnes moving bed biofilm reactors*. Aquacultural Engineering 34(3): 322-331.

Rusten, B., Hem, L.J. and Odegaard, H. (**1995**) *Nitrification of Municipal Waste-Water in Moving-Bed Biofilm Reactors*. Water Environment Research 67(1): 75-86.

Sahle-Demessie, E. and Tadesse, H. (**2011**) *Kinetics and equilibrium adsorption of nano-TiO2 particles on synthetic biofilm*. Surface Science 605(13-14): 1177-1184.

Sanderlin, A.B., Vogt, S.J., Grunewald, E., Bergin, B.A. and Codd, S.L. (**2013**) *Biofilm Detection in Natural Unconsolidated Porous Media Using a Low-Field Magnetic Resonance System*. Environmental Science & Technology 47(2): 987-992.

Schaumann, G.E., Philippe, A., Bundschuh, M., Metreveli, G., Klitzke, S., Rakcheev, D., Grun, A., Kumahor, S.K., Kuhn, M., Baumann, T., Lang, F., Manz, W., Schulz, R. and Vogel, H.-J. (**2015**) *Understanding the fate and biological effects of Ag- and TiO2-nanoparticles in the environment: The quest for advanced analytics and interdisciplinary concepts*. Science of the Total Environment 535: 3-19.

Schmid, G. (**2010**) *Nanoparticles: from theory to application*, Wiley-VCH Weinheim.

Schwegmann, H., Feitz, A.J. and Frimmel, F.H. (**2010**) *Influence of the zeta potential on the sorption and toxicity of iron oxide nanoparticles on S. cerevisiae and E. coli*. Journal of Colloid and Interface Science 347(1): 43-48.

Seymour, J.D., Codd, S.L., Gjersing, E.L. and Stewart, P.S. (**2004a**) *Magnetic resonance microscopy of biofilm structure and impact on transport in a capillary bioreactor*. Journal of Magnetic Resonance 167(2): 322-327.

Seymour, J.D., Gage, J.P., Codd, S.L. and Gerlach, R. (**2004b**) *Anomalous fluid transport in porous media induced by biofilm growth*. Physical Review Letters 93(19).

Seymour, J.D., Gage, J.P., Codd, S.L. and Gerlach, R. (**2007**) *Magnetic resonance microscopy of biofouling induced scale dependent transport in porous media*. Advances in Water Resources 30(6-7): 1408-1420.

Shang, Z., Van Nostrand, J.D., Zhou, J. and Liu, Y. (**2015**) *The effects of silver nanoparticles on intact wastewater biofilms*. Frontiers in Microbiology 6(680).

Sheng, Z.Y. and Liu, Y. (**2011**) *Effects of silver nanoparticles on wastewater biofilms*. Water Research 45(18): 6039-6050.

Sherwood-Scientific (**2006**) *MSB - Auto Magnetic Suceptibility Balance, Operator's Manual*, Sherwood Scientific Ltd, Cambridge.

Sibag, M., Choi, B.-G., Suh, C., Lee, K.H., Lee, J.W., Maeng, S.K. and Cho, J. (**2015**) *Inhibition of total oxygen uptake by silica nanoparticles in activated sludge*. Journal of Hazardous Materials 283: 841-846.

Solomon, I. (**1955**) *Relaxation processes in a system of 2 spins*. Physical Review 99(2): 559-565.

Som, C., Berges, M., Chaudhry, Q., Dusinska, M., Fernandes, T.F., Olsen, S.I. and Nowack, B. (**2010**) *The importance of life cycle concepts for the development of safe nanoproducts*. Toxicology 269(2-3): 160-169.

Stark, W.J. (**2011**) *Nanoparticles in Biological Systems*. Angewandte Chemie-International Edition 50(6): 1242-1258.

Staudt, C., Horn, H., Hempel, D.C. and Neu, T.R. (**2004**) *Volumetric measurements of bacterial cells and extracellular polymeric substance glycoconjugates in biofilms*. Biotechnology and Bioengineering 88(5): 585-592.

Stewart, P.S. (**2003**) *Diffusion in biofilms*. Journal of Bacteriology 185(5): 1485-1491.

Stewart, P.S. (**2012**) *Mini-review: Convection around biofilms*. Biofouling 28(2): 187-198.

Stewart, P.S. and Costerton, J.W. (**2001**) *Antibiotic resistance of bacteria in biofilms*. Lancet 358(9276): 135-138.

Stumm, W. (**1992**) *Chemistry of the solid-water interface. Processes at the mineral-water and particle-water interface in natural waters.*, Wiley Interscience, New York.

Stumm, W. and Morgan, J.J. (**1996**) *Aquatic chemistry. Chemical equilibria and rates in natural waters*, Wiley Interscience, New York.

Sun, T.Y., Gottschalk, F., Hungerbuehler, K. and Nowack, B. (**2014**) *Comprehensive probabilistic modelling of environmental emissions of engineered nanomaterials*. Environmental Pollution 185: 69-76.

Tan, M., Qiu, G. and Ting, Y.-P. (**2015**) *Effects of ZnO nanoparticles on wastewater treatment and their removal behavior in a membrane bioreactor*. Bioresource Technology 185(0): 125-133.

Theron, J., Walker, J.A. and Cloete, T.E. (**2008**) *Nanotechnology and water treatment: Applications and emerging opportunities*. Critical Reviews in Microbiology 34(1): 43-69.

Thill, A., Zeyons, O., Spalla, O., Chauvat, F., Rose, J., Auffan, M. and Flank, A.M. (**2006**) *Cytotoxicity of CeO2 nanoparticles for Escherichia coli. Physico-chemical insight of the cytotoxicity mechanism*. Environmental Science & Technology 40(19): 6151-6156.

Tiller, C.L. and Omelia, C.R. (**1993**) *Nautral organic matter and colloidal stability - models and measruements*. Colloids and Surfaces a-Physicochemical and Engineering Aspects 73: 89-102.

Van Loosdrecht, M.C.M., Eikelboom, D., Gjaltema, A., Mulder, A., Tijhuis, L. and Heijnen, J.J. (**1995**) *Biofilm structures*. Water Science and Technology 32(8): 35-43.

Vogt, S.J., Sanderlin, A.B., Seymour, J.D. and Codd, S.L. (**2013**) *Permeability of a growing biofilm in a porous media fluid flow analyzed by magnetic resonance displacement-relaxation correlations*. Biotechnology and Bioengineering 110(5): 1366-1375.

von der Schulenburg, D.A.G., Holland, D.J., Paterson-Beedle, M., Macaskie, L.E., Gladden, L.F. and Johns, M.L. (**2008a**) *Spatially resolved quantification of metal ion concentration in a biofilm-mediated ion exchanger*. Biotechnology and Bioengineering 99(4): 821-829.

von der Schulenburg, D.A.G., Vrouwenvelder, J.S., Creber, S.A., van Loosdrecht, M.C.M. and Johns, M.L. (**2008b**) *Nuclear magnetic resonance microscopy studies of membrane biofouling*. Journal of Membrane Science 323(1): 37-44.

Waesche, S., Horn, H. and Hempel, D.C. (**2002**) *Influence of growth conditions on biofilm development and mass transfer at the bulk/biofilm interface*. Water Research 36(19): 4775-4784.

Wagner, M., Ivleva, N.P., Haisch, C., Niessner, R. and Horn, H. (**2009**) *Combined use of confocal laser scanning microscopy (CLSM) and Raman microscopy (RM): Investigations on EPS - Matrix*. Water Research 43(1): 63-76.

Wagner, M., Manz, B., Volke, F., Neu, T.R. and Horn, H. (**2010a**) *Online Assessment of Biofilm Development, Sloughing and Forced Detachment in Tube Reactor by Means of Magnetic Resonance Microscopy*. Biotechnology and Bioengineering 107(1): 172-181.

Wagner, M., Taherzadeh, D., Haisch, C. and Horn, H. (**2010b**) *Investigation of the Mesoscale Structure and Volumetric Features of Biofilms Using Optical Coherence Tomography*. Biotechnology and Bioengineering 107(5): 844-853.

Wang, Y., Westerhoff, P. and Hristovski, K.D. (**2012**) *Fate and biological effects of silver, titanium dioxide, and C-60 (fullerene) nanomaterials during simulated wastewater treatment processes*. Journal of Hazardous Materials 201: 16-22.

Wanner, O. (**2006**) *Mathematical modeling of biofilms*, IWA Publishing, London.

Wasche, S., Horn, H. and Hempel, D.C. (**2002**) *Influence of growth conditions on biofilm development and mass transfer at the bulk/biofilm interface*. Water Research 36(19): 4775-4784.

Weishaupt, D., Köchli, V.D. and Marincek, B. (**2006**) *How Does MRI Work? : An Introduction to the Physics and Function of Magnetic Resonance Imaging*, Springer-Verlag, Berlin, Heidelberg.

Weiss, A. and Witte, H. (**1973**) *Magnetochemie : Grundlagen und Anwendungen*, Verlag Chemie, Weinheim/Bergstr.

Wessman, F.G., Yuegen, E.Y., Zheng, Q., He, G., Welander, T. and Rusten, B. (**2004**) *Increasing the capacity for treatment of chemical plant wastewater by replacing existing suspended carrier media with Kaldnes Moving Bed (TM) media at a plant in Singapore*. Water Science and Technology 49(11-12): 199-205.

Westerhoff, P.K., Kiser, A. and Hristovski, K. (**2013**) *Nanomaterial Removal and Transformation During Biological Wastewater Treatment*. Environmental Engineering Science 30(3): 109-117.

Wiesmann, U., Choi, I. and Dombrowski, E. (**2007**) *Fundamentals of biological wastewater treatment*, Wiley-Verlag, Weinheim.

Wiesner, M.R., Lowry, G.V., Alvarez, P., Dionysiou, D. and Biswas, P. (**2006**) *Assessing the risks of manufactured nanomaterials*. Environmental Science & Technology 40(14): 4336-4345.

Wiesner, M.R., Lowry, G.V., Jones, K.L., Hochella, M.F., Jr., Di Giulio, R.T., Casman, E. and Bernhardt, E.S. (**2009**) *Decreasing Uncertainties in Assessing Environmental Exposure, Risk, and Ecological Implications of Nanomaterials*. Environmental Science & Technology 43(17): 6458-6462.

Wirth, S., Lowry, G. and Tilton, R. (**2012**) *Natural Organis matter Alters Biofilm Tolerance to Silver Nanoparticles and Dissolved Silver*. Environmental Science & Technology 46: 12687-12696.

Yang, Y. and Alvarez, P.J.J. (**2015**) *Sublethal Concentrations of Silver Nanoparticles Stimulate Biofilm Development*. Environmental Science & Technology Letters 2(8): 221-226.

Yang, Y., Wang, Y., Hristovski, K. and Westerhoff, P. (**2015**) *Simultaneous removal of nanosilver and fullerene in sequencing batch reactors for biological wastewater treatment*. Chemosphere 125: 115-121.

Yeo, M.-K. and Kang, M. (**2008**) *Effects of nanometer sized silver materials on biological toxicity during zebrafish embryogenesis*. Bulletin of the Korean Chemical Society 29(6): 1179-1184.

Yu, R., Fang, X., Somasundaran, P. and Chandran, K. (**2015**) *Short-term effects of TiO2, CeO2, and ZnO nanoparticles on metabolic activities and gene expression of Nitrosomonas europaea*. Chemosphere 128: 207-215.

Yuan, Z.-H., Yang, X., Hu, A. and Yu, C.-P. (**2015**) *Long-term impacts of silver nanoparticles in an anaerobic-anoxic-oxic membrane bioreactor system*. Chemical Engineering Journal 276: 83-90.

Zhang, W.X. (**2003**) *Nanoscale iron particles for environmental remediation: An overview*. Journal of Nanoparticle Research 5(3-4): 323-332.

Zhang, Y., Chen, Y., Westerhoff, P. and Crittenden, J. (**2009**) *Impact of natural organic matter and divalent cations on the stability of aqueous nanoparticles*. Water Research 43(17): 4249-4257.

Zhang, Y., Chen, Y., Westerhoff, P., Hristovski, K. and Crittenden, J.C. (**2008**) *Stability of commercial metal oxide nanoparticles in water*. Water Research 42(8-9): 2204-2212.

Zhou, X.-h., Huang, B.-c., Zhou, T., Liu, Y.-c. and Shi, H.-c. (**2015**) *Aggregation behavior of engineered nanoparticles and their impact on activated sludge in wastewater treatment*. Chemosphere 119: 568-576.

Verification of the contributions from the co-authors

Chapter 4

Title: Direct surface visualization of biofilms with high spin coordination clusters using magnetic resonance imaging

Journal: Acta Biomaterialia, (2016), 31: 167–177. (http://dx.doi.org/ 10.1016/j.actbio.2015.12.007)

Authors: Florian Ranzinger, Maria Pia Herrling, Susanne Lackner, Vanessa W. Grande, Amer Baniodeh, Annie K. Powell, Harald Horn, Gisela Guthausen

Position in the dissertation:

The content of this paper has been included in Chapter 4.

Contribution of Florian Ranzinger (First author) (40%):

- designed and conducted the batch experiment
- data acquisition and processing via Matlab
- wrote the first draft of the manuscript

Contribution of Maria Pia Herrling (Second author) (40%):

- conceived the concept
- designed the experiment
- analysis and discussion of the data/results
- wrote and corrected the manuscript

Contribution of Susanne Lackner (Third author) (2%):

- discussion of the data/results
- corrected the manuscript

Contribution of Vanessa Grande (Fourth author) (0.5%):

- provided contrast agent (cluster molecule)

Contribution of Amer Baniodeh (Fifth author) (0.5%):

- provided contrast agent (cluster molecule)

Contribution of Annie Powell (Sixth author) (1%):

- provided contrast agent (cluster molecule)
- corrected the manuscript

Contribution of Harald Horn (Sixth author) (2%):

- discussion of the results
- corrected the manuscript

Contribution of Gisela Guthausen (Seventh author) (14%):

- conceived the concept

- acquired and processed MRI data
- designed the experiment
- analysis and discussion of the data/results
- corrected the manuscript

Signature of the authors:

Author	*Electronic signature*
Florian Ranzinger	
Maria Pia Herrling	
Susanne Lackner	
Vanessa Grande	
Amer Baniodeh	
Annie Powell	
Harald Horn	
Gisela Guthausen	

Permission from Elsevier:

"*The authors can include their articles in full or in part in a thesis or dissertation for non-commercial purposes."*

Source: Homepage Elsevier (https://www.elsevier.com/about/company-information/policies/copyright/permissions, status: 15th January 2016)

Chapter 5

Title: Low biosorption of PVA coated engineered magnetic nanoparticles in granular sludge assessed by magnetic susceptibility

Journal: Science of the total Environment, (2015), 537: 43-50. (http://dx.doi.org/10.1016/j.scitotenv.2015.07.161)

Authors: Maria Pia Herrling, Katharina Fetsch, Markus Delay, Florian Blauert, Michael Wagner, Mathias Franzreb, Harald Horn, Susanne Lackner

Position in the dissertation:

The content of this paper has been included in Chapter 5.

Contribution of Maria Pia Herrling (First author) (75%):

- conceived the concept
- designed the experiment
- conducted the batch experiments
- analysis and discussion of the data/results
- wrote and corrected the manuscript

Contribution of Katharina Fetsch (Second author) (7%):

- conducted the batch experiments
- analysis and discussion of the data/results

Contribution of Markus Delay (Third author) (5%):

- discussion of the results
- corrected the manuscript

Contribution of Florian Blauert (Fourth author) (1%):

- acquired the OCT images

Contribution of Michael Wagner (Fifth author) (1%):

- acquired the OCT images
- corrected the manuscript

Contribution of Mathias Franzreb (Sixth author) (1%):

- provided nanoparticles for batch experiments
- discussion of the results
- corrected the manuscript

Contribution of Harald Horn (Sixth author) (5%):

- discussion of the results
- corrected the manuscript

Contribution of Susanne Lackner (Seventh author) (5%):

- designed the experiment
- discussion of the results
- corrected the manuscript

Signature of the authors:

Author	*Electronic signature*
Maria Pia Herrling	
Katharina Fetsch	
Markus Delay	

Florian Blauert	
Michael Wagner	
Matthias Franzreb	
Harald Horn	
Susanne Lackner	

Permission from Elsevier:

"*The authors can include their articles in full or in part in a thesis or dissertation for non-commercial purposes."*

Source: Homepage Elsevier (https://www.elsevier.com/about/company-information/policies/copyright/permissions, status: 15th January 2016)

Chapter 6

Title: Short and long term biosorption of silica-coated iron oxide nanoparticles in heterotrophic biofilms

Journal: Science of the total Environment, (2016), 544: 722–729 (http://dx.doi.org/10.1016/j.scitotenv.2015.11.174)

Authors: Maria Pia Herrling, Susanne Lackner, Oleg Tatti, Gisela Guthausen, Markus Delay, Mathias Franzreb, Harald Horn,

Position in the dissertation:

The content of this paper has been included in Chapter 6.

Contribution of Maria Pia Herrling (First author) (77%):

- conceived the concept
- designed the experiment
- conducted the experiments
- analysis and discussion of the data/results
- wrote and corrected the manuscript

Contribution of Susanne Lackner (Second author) (5%):

- designed the experiment
- corrected the manuscript

Contribution of Oleg Tatti (Third author) (7%):

- conducted the experiments
- analysis and discussion of the data/results

Contribution of Gisela Guthausen (Fourth author) (2%):

- acquired MRI images
- discussion of the data/results

Contribution of Markus Delay (Fifth author) (2%):

- discussion of the data/results
- corrected the manuscript

Contribution of Mathias Franzreb (Sixth author) (2%):

- provided nanoparticles for experiments
- discussion of the data/results
- corrected the manuscript

Contribution of Harald Horn (Sixth author) (5%):

- discussion of the data/results
- corrected the manuscript

Signature of the authors:

Author	*Electronic signature*
Maria Pia Herrling	
Susanne Lackner	
Oleg Tatti	
Gisela Guthausen	
Markus Delay	
Matthias Franzreb	
Harald Horn	

Permission from Elsevier:

"*The authors can include their articles in full or in part in a thesis or dissertation for non-commercial purposes."*

Source: Homepage Elsevier (https://www.elsevier.com/about/company-information/policies/copyright/permissions, status: 15th January 2016)

Chapter 7

Title: Determining the flow regime in a biofilm carrier by means of magnetic resonance imaging

Journal: Biotechnology and Bioengineering, (2015), 112(5): 1023-1032.
(http://dx.doi.org/10.1002/bit.25510)

Authors: Maria Pia Herrling, Gisela Guthausen, Michael Wagner, Susanne Lackner, Harald Horn

Position in the dissertation:

The content of this paper has been included in Chapter 7.

Contribution of Maria Pia Herrling (First author) (75%):

- conceived the concept
- designed the experiment
- conducted the MRI flow experiments
- analysis and discussion of the data/results
- wrote and corrected the manuscript

Contribution of Gisela Guthausen (Second author) (13%):

- designed the experiment
- MRI data analysis via Matlab
- discussion of the data/results
- corrected the manuscript

Contribution of Michael Wagner (Third author) (2%):

- discussion of the data/results
- corrected the manuscript

Contribution of Susanne Lackner (Fourth author) (5%):

- designed the experiment
- discussion of the data/results
- corrected the manuscript

Contribution of Harald Horn (Last author) (5%):

- discussion of the data/results
- corrected the manuscript

Signature of the authors:

Author	*Electronic signature*
Maria Pia Herrling	
Gisela Guthausen	
Michael Wagner	

Susanne Lackner	
Harald Horn	

Permission from Wiley:

Permission Letter given to Maria Pia Herrling, 16th February 2016:

Permission is hereby granted for the use requested subject to the usual acknowledgements (Herrling et al., Determining the flow regime in a biofilm carrier by means of magnetic resonance imaging, Biotechnology and Bioengineering, (2015), 112(5): 1023-1032. (http://dx.doi.org/10.1002/bit.25510)). You should also duplicate the copyright notice that appears in the Wiley publication; this can be found on the copyright page if the material is a book or within the article if it is a journal.

Any third party material is expressly excluded from this permission. If any of the material you wish to use appears within our work with credit to another source, authorization from that source must be obtained.

This permission does not include the right to grant others permission to photocopy or otherwise reproduce this material except for accessible versions made by non-profit organizations serving the blind, visually impaired and other persons with print disabilities (VIPs).

Paulette Goldweber (E-mail: pgoldweb@wiley.com)
Manager, Copyright & Permissions Wiley
111 River Street, MS 4-02
Hoboken, NJ 07030-5774, U.S.

"*Reuse in a Dissertation/Thesis: A dissertation/thesis license authorizes an advanced degree candidate to reproduce portions of the content in his/her doctoral thesis or dissertation. For full article/chapter content, please contact publisher directly to obtain approval. If your license is for use in a thesis or dissertation, your thesis may be submitted to your institution in either print or electronic format. If your thesis, or dissertation, is to be published commercially, then you must reapply for permission. If you are an author of the article/chapter wishing to reuse the content in full please refer to your Author Licensing Agreement for an explanation of your retained author rights."*

Source: Homepage Wiley
(https://s100.copyright.com/help/rightslinkhelppages/Frequently_Asked_Questions_wiley.htm, status: 15th January 2016)

Schriftenreihe des Lehrstuhls für Wasserchemie und Wassertechnologie und der DVGW-Forschungsstelle am Engler-Bunte-Institut des Karlsruher Instituts für Technologie (KIT)

Band 35: Symposium on Refractory Organic Substances in the Environment – ROSE, 1997, 248 S., 12,80 €.

Band 36: Symposium on Refractory Organic Substances in the Environment – ROSE II, 2000, 265 S., 12,80 €.

Band 37: Thomas Brinkmann: Alkalischer und solarinduzierter Abbau von natürlicher organischer Materie, 2003, 212 S., 15,00 €.

Band 38: Andreas Gorenflo: Rückhalt und Fouling von natürlichen organischen Substanzen bei der Nano- und Ultrafiltration, 2003, 219 S., 18,00 €.

Band 39: Philip Hörsch: Einfluss der chemischen Oxidation auf das toxische Potenzial und das biologische Abbauverhalten von Industrieabwässern, 2004, 210 S., 20,00 €.

Band 40: Margit B. Müller: Bewertung von Anreicherungs- und Fraktionierungsverfahren für die strukturelle Charakterisierung der gelösten organischen Substanz in Gewässern, 2004, 185 S., 18,00 €.

Band 41: Fritz H. Frimmel, Gudrun Abbt-Braun: Praktikum Allgemeine Chemie und Chemie in wässrigen Lösungen – Qualitative und quantitative Bestimmungen, 2004, 158 S., 18,00 €.

Band 42: Tusnelda E. Doll: Photochemischer und photokatalytischer Abbau von Carbamazepin, Clofibrinsäure, Iomeprol und Iopromid, 2004, 158 S., 18,00 €.

Band 43: Ayşe B. Değer: Entfernung von organischen Schadstoffen aus Wasser mit Hilfe von Poly(ε-caprolacton), 2005, 205 S., 18,00 €.

Band 44: Fritz H. Frimmel, Gudrun Abbt-Braun: Wassertechnologisches und wasserchemisches Praktikum, 2005, 201 S., 20,00 €.

Band 45-I, 45-II: Fritz H. Frimmel, Gudrun Abbt-Braun (Eds.): Humic Substances – Linking Structure to Functions. Proceedings of the 13th Meeting of the International Humic Substances Society, July 30 to August 4, 2006, Universität Karlsruhe, 2006, 492 S. (45-I), 623 S. (45-II), 50,00 €.

Band 46: Fritz H. Frimmel, Gudrun Abbt-Braun: Praktikum Allgemeine Chemie und Chemie in wässrigen Lösungen – Qualitative und quantitative Bestimmungen II, 2. verbesserte und ergänzte Neuauflage 2007, 139 S., 20,00 €.

Band 47: Thomas Glauner: Aufbereitung von Schwimmbeckenwasser – Bildung und Nachweis von Desinfektionsnebenprodukten und ihre Minimierung mit Membran- und Oxidationsverfahren, 2007, 233 S., 20,00 €.

Band 48: George Metreveli: Kolloidale Wechselwirkungen und kolloidgetragener Transport von Metall(oid)en in porösen Medien, 2008, 215 S., 20,00 €.

Band 49: Florencia Saravia: Entfernung von organischen Spurenstoffen und Untersuchung von Foulingprozessen in getauchten Membranen und Hybridverfahren, 2009, 213 S., 20,00 €.

Band 50: Markus Delay: Dynamische versus statische Elutionsversuche – Ein Beitrag zur Beurteilung der Wiederverwertbarkeit von Abfallmaterialien, 2010, 206 S., 20,00 €.

Band 51: Luis A. Tercero Espinoza: Heterogeneous photocatalysis with titanium dioxide suspensions containing bromide and dissolved organic matter, 2010, 172 S., 20,00 €.

Band 52: Ulrich-M. Metzger: Extrazelluläre polymere Substanzen aus Biofilmen – Aufklärung von Strukturen und ihr Einfluss auf die Foulingbildung in Membranbioreaktoren, 2011, 211 S., 20,00 €.

Band 53: Fritz H. Frimmel, Gudrun Abbt-Braun: Praktikum Allgemeine Chemie und Chemie in wässrigen Lösungen – Qualitative und quantitative Bestimmungen, 3. überarbeitete Neuauflage 2011, 139 S., 20,00 €.

Band 54: Markus Ziegmann: Beurteilung von Cyanobakterienblüten und Untersuchung geeigneter Verfahrenskombinationen zur Eliminination cyanobakterieller Zellen und Toxine, 2011, 191 S., 20,00 €.

Band 55: Fritz H. Frimmel, Gudrun Abbt-Braun: Praktikum Allgemeine Chemie und Chemie in wässrigen Lösungen – Qualitative und quantitative Bestimmungen, 4. ergänzte Neuauflage 2012, 137 S., 20,00 €.

Band 56: Angela Klüpfel: Nanofiltration bei der Aufbereitung von Trink- und Schwimmbeckenwasser – Foulingmechanismen und Rückhalt anthropogener Kontaminanten, 2012, 259 S., 20,00 €.

Band 57: Christina Schmalz: Bildung, Phasentransfer und Toxizität halogenierter Desinfektionsnebenprodukte im Aufbereitungszyklus von Schwimmbeckenwasser – Schwerpunkt stickstoffhaltige Verbindungen, 2012, 195 S., 20,00 €.

Band 58: Fritz H. Frimmel, Gudrun Abbt-Braun, Harald Horn: Praktikum Allgemeine Chemie und Chemie in wässrigen Lösungen – Qualitative und quantitative Bestimmungen, 5. ergänzte Neuauflage 2013, 120 S., 20,00 €.

Band 59: Heiko Schwegmann: Wechselwirkungen zwischen anorganischen Nanopartikeln und Mikroorganismen – Nutzungs- und Gefährdungspotentiale, 2013, 149 S., 20,00 €.

Band 60: Fritz H. Frimmel, Gudrun Abbt-Braun, Harald Horn: Praktikum Allgemeine Chemie und Chemie in wässrigen Lösungen – Qualitative und quantitative Bestimmungen, 6. Überarbeitete Neuauflage 2014, 129 S., 20,00 €.

Band 61: Carsten Jobelius: Anaerobe Metabolite organischer Schadstoffe im Grundwasser - Analytik, Bildung und Nutzung als Indikatoren, 2014, 247 S., 20,00 €.

Band 62: Eva M. Gilbert: Partielle Nitritation / Anammox bei niedrigen Temperaturen, 2014, 115 S., 20,00 €.

Band 63: Aleksandr O. Kondrakov: Heterogeneous photocatalysis and sensitized photolysis for enhanced degradation of bisphenol A and its analogues, 2015, 155 S., 20,00 €.

Band 64: Meijie Ren: TiO2: application in photocatalysis for the degradation of organic pollutants and aggregation behavior in aquatic systems, 2015, 121 S., 20,00 €.

Band 65: Fritz H. Frimmel, Gudrun Abbt-Braun, Harald Horn: Praktikum Allgemeine Chemie und Chemie in wässrigen Lösungen – Qualitative und quantitative Bestimmungen, 7. überarbeitete Neuauflage 2016, 126 S., 20,00 €.

Band 66: Chunyan Li: Using optical coherence tomography to quantify biofilm structure and mass transfer in combination with mathematical modeling, 2016, 121 S., 20,00 €.

Band 67: Maria Pia Herrling: Nanoparticles in biofilm systems – assessment of their interactions by magnetic susceptibility balance and magnetic resonance imaging, 2016, 132 S., 20,00 €.

Preise verstehen sich zzgl. der gesetzlichen Mehrwertsteuer und Versandkosten.

Bestellungen über:
Lehrstuhl für Wasserchemie und Wassertechnologie und DVGW-Forschungsstelle
am Engler-Bunte-Institut des Karlsruher Instituts für Technologie (KIT)
Engler-Bunte-Ring 9
D-76131 Karlsruhe
Tel.: +49-(0)721-608-42581
Fax: +49-(0)721-608-46497
E-mail: ebi-sekretariat-wasserchemie@kit.edu